Towards 50 Year Lifetime PV Modules: Double Glass vs. Glass/Backsheet

Project Title	**Towards 50 Year Lifetime PV Modules: Double Glass vs. Glass/Backsheet**
Report	**Final report**
Project Period	(01/01/2019 – 06/30/2022)
Budget Period	(01/01/2021 – 06/30/2022)
Reporting Period	(08/01/2022 – 09/30/2022)
Reporting Frequency	Quarterly
Submission Date	10/30/2022
Award Number	**DE-EE-0008550**
Recipient	**Case Western Reserve University**
Address	10900 Euclid Avenue Cleveland, OH 44106-7204
Website	SDLE Research Center
Project Team	**Case Western Reserve University**
Collaboration With	**Canadian Solar, Inc., National Renewable Energy Laboratory, Cybrid, Dupont**
Principal Investigator	**Roger H. French, Kyocera Professor**
Phone:	216-368-3655
Email	rxf131@case.edu
Business Contact	**Jonathan Steirer, SDLE Operations Manager**
Phone	216-368-0374
Email	jws227@case.edu
HQ Tech Manager	**Marie Mapes**
HQ Project Officer:	**Jeremey Mikrut**
GO Grant Specialist:	**Fania Barwick**
GO Contracting Officer:	**Diana Bobo**

Signature Date

Acknowledgement: This material is based upon work supported by the U.S. Department of Energy's Office of Energy Efficiency and Renewable Energy (EERE) under the Solar Energy Technologies Office (SETO) award number DE-EE0008550.

Information from Statement of Project Objectives (SOPO)

This award aims to increase the lifetime of c-Si modules by lowering the power degradation rate to the goal of 0.2 %/year, while also increasing the harvested irradiance per module using bifacial cells to achieve the 2030 SunShot goal of $0.03/kWh. Increasing the durability and lifetime of modules requires improved module packaging material choices and module architectures to exploit new cell improvements. Bifacial PERC cells (with backside aluminum fingers) are becoming a primary PV technology due to their decreased rear surface recombination and increased light absorption compared to traditional monofacial Al-BSF cells. Bifacial modules with double glass architectures have been deployed to capture the rear-side irradiance thereby increasing the light captured. The choice of a double glass (DG) or glass/backsheet (GB) module leads to two very different chemical (e.g., O_2, H_2O) and mechanical environments (e.g., mechanical stress levels) inside the PV module that impact the cell's operational conditions. The recipient will fabricate 4-cell DG and GB minimodules with various module architectures or constructions (mono- & bifacial cells, transparent & white encapsulants), and conduct stepwise accelerated exposures and characterization. These stepwise evaluations of degradation include evaluations for electrical, mechanical, and chemical degradation that would reduce the overall power output. Evaluations will be performed stepwise during exposure giving key insights into the mechanisms driving degradation and the strength of the various degradation pathways. Samples will be retained for additional non-destructive and destructive mechanical and chemical evaluations. Through the integration of materials, cell, and module-level data, the recipient will quantify the impact of module architecture and packaging materials on mechanistic degradation pathways and rates in both DG and GB modules by network structural equation (netSEM) modeling. The recipient will also use advanced statistical methods to model power and mechanistic degradation of fielded bifacial PERC DG and GB minimodules using time-series I-V data. By developing degradation models for each type of mini-module architecture and bill of materials, the recipient can determine the best approach for module design when comparing DG and GB modules. The three objectives of this award: 1. Optimize DG and GB designs for degradation rate, mechanical durability, and cost. 2. Quantify degradation rates and modes specific to DG and GB mono-/bi-facial modules. 3. Identify module architectures, packaging materials, and cell designs by cross-correlating indoor/outdoor mini-module results to advance the industry to 50 year lifetimes.

Backsheet modules lead to a "breathable" cell environment with varying oxygen and moisture content, which strongly influences the rates of photolysis, hydrolysis, and thermolysis inside the module, while at the same time providing an asymmetric mechanical stress environment that could give rise to cracking. A DG module design produces a cell environment with more constant concentrations of oxygen and moisture and less breathability of encapsulant degradation products such as acetic acid, while at the same time representing a more symmetrical stress state, and potentially greater protection from mechanical impacts. This award will identify and mitigate relevant degradation modes (corrosion and mechanical) in GB and DG modules to reduce the power degradation rate of PV modules to the goal of 0.2%/year, toward increasing PV module lifetimes to 50 years.

DG modules have potential advantages over GB modules, including increased rigidity and decreased permeability, but it is an unknown whether DG will create additional degradation mechanisms for cells. New degradation mechanisms may also be brought on by encapsulant choices within the module, so the recipient will explore white, UV cutoff, and transparent encapsulant variations of both POE and EVA. The additives in white and UV cutoff forms of these encapsulants may create additional degradation risks, especially for cell corrosion. Recent accelerated exposures show that GB modules tend to show crack propagation after thermal cycling, while DG forms cracks at cell edges. After damp heat exposure, GB modules show busbar darkening and dark spots in EL, while there is no significant change in DG modules. Because both mechanical and chemical degradation are of concern for comparing DG and GB modules, this award will include sequential tests of damp heat with thermal cycling and/or mechanical stress. The award is structured for direct comparison of DG and GB minimodules, and cross-correlation of outdoor and accelerated results to identify module architecture, materials, and cells to optimize module packaging for 50 year lifetimes.

Contents

1 Executive Summary

All the milestones, subtasks and End of Project (EOP) have been completed during Budged Period 1 and Budged Period 2. See Section 2 for the detailed Task, Subtasks, and Milestones from the SOPO. The objectives of this project are as follows:

-

A brief summary of the sections in the report are presented here and the relevant sections are referenced.

Minimodule fabrication and characterization In this project, 5 different sets with varied packaging strategies and module architectures were fabricated at CSI and CWRU manufacturing facilities. Forty-eight minimodules each from sets #1-#4 and 40 minimodules from set #5 (including retained minimodules) were fabricated at both facilities. Across 5 sets, a total of 232 minimodules were fabricated. In addition, 120 1-cell minimodules were fabricated and shipped to NREL for mechanical testing studies. Stepwise characterization techniques, namely I-V, $SunsV_{oc}$, electroluminescence (EL), electroluminescence (PL), and 4-point proof loading, were utilized to monitor degradation. More details are highlighted in Sections 3.1.1 and 3.1.2.

Minimodule exposures: Two types of exposures were implemented in this project: indoor accelerated and outdoor exposures. There are two types of indoor accelerated exposures including: modified damp heat (mDH) and mDH with full spectrum light (mDH + FSL). mDH is 80 $^{\circ}C$ and 85 % relative humidity and FSL makes use of 420 W^{-2} light intensity. All the minimodule sets were preconditioned and exposed in either accelerated conditions for a total of 2520 hours. Thirty-two minimodules from sets #1-#4 were exposed outdoors at the SDLE SunFarm located in Cleveland, OH. This location belongs to the Dfa climate (continental, no dry season, hot summer) according to the Köppen-Geiger climate classification system. The outdoor exposure was performed for 1.6 years.

T50 webinar: The T50 workshop with up-to-date results from the project was held on August 18, 2020. The title of the workshop was 'Strategies of PV Modules with Lower Performance Loss Rates'. 127 participants registered from industry (81) and research institutions (46). Most of the participants were from research and manufacturing fields. One of the major interests among participants was bifacial PV modules, followed by degradation studies.

Accelerated exposure results All the minimodule sets were compared using degradation pathway modeling (netSEM) and (predictive) confidence intervals from 0-2520 hours of accelerated exposures. Predictive confidence intervals were used to rank-order durable/degrading variants. Set #5 minimodules are seen to be experiencing greater power loss in comparison to the other minimodule sets. This could be due to issues in packaging material formulation optimization and/or quality control. The degradation mode strongly influencing this behavior is corrosion, which is consistent from our Markovian and multiple regression analysis. There is no strong dependence on encapsulant on the performance but manufacturer and module architecture apparently play a role in the degradation behavior of minimodules. The durable variants are stable in mDH+FSL exposure, which is more realistic. From our rank-ordering results, the most stable variants are GB minimodules from set #4.

Outdoor exposure results Thirty-two minimodules from sets #1-#4 were exposed in outdoor conditions (SDLE SunFarm) for 1.6 years. Slopes from linear models obtained from degradation pathway modeling reveals that bi_POE_Opaq_GB, mono_EVA_Opaq_DG and mono_POE_Opaq_GB degrade the most, whereas bi_POE_Opaq_DG and bi_EVA_Opaq_DG were found to be relatively stable. In the degrading variants, the prominent cause of degradation is optical transmission loss.

Mechanical modeling of cells, packaging materials & minimodules Mechanical modeling was done using simulations and 4-point proof loading experiments for bare and packaged cells. Weibull modulus values decrease for soldered bifacial cells in both the testing orientations which indicate a greater distribution in measurements but the fracture displacement doesn't change, indicating that the limiting flaw size distribution is due to soldering. One-cell minimodules with bifacial cells have a lower characteristic fracture strain value in the $\perp$ orientation compared to $||$, which makes them more sensitive to loading. From finite element modeling, the tensile strain is constant between inner spans for bare cells whereas for the minimodule 4-point bending, the tensile strain is maximum only at the center of the cell. From numerical simulations, it was found that the strength limiting flaws are most likely to reside on the edge area of these cells. When the four-cell module is loaded uniformly, about 20 % reduction in characteristic strength is expected between the packaged and bare cell. The 4-point proof loading experiment done on 4-cell GB minimodules reveal that minimodule cells that did not have cracks before the experiment did not develop cracks during the loading.

Characterization of rear encapsulants from set #5 minimodules The rear encapsulants were extracted from set #5 GB minimodules after step 6 of exposure (i.e., 3024 hours of exposure) and compared against retained samples with same specifications. Colorimetry and FTIR were performed to track changes in the rear encapsulants. From 2000 to 3000 cm^{-1}, EPE behaves similarly to both POE and EPE. However, past 3000 cm^{-1}, we observe the appearance of a small peak in the EPE encapsulant spectra, which looks similar to the water absorption band, indicating a potential onset of delamination due to water ingress and/or additive diffusion. This is likely due to the lamination recipe for set #5 not being fully optimized. An increase in yellowness index (YI) from unexposed to exposed encapsulant samples was observed. The largest YI increase can be seen for the POE rear encapsulant.

Neural networks for predicting overall changes in electrical parameters Neural network architectures were utilized to quantitatively learn spatial and temporal information and predict the change of electrical features from spatiotemporal image datasets. Fifty-two model variants with different input image types and image preprocessing methods were trained. Recurrent neural networks (RNNs) performed significantly better than convolutional neural networks (CNNs).

Indoor/outdoor cross correlation

Publications & Presentations A total of 3 journal articles, 5 conference proceedings and 10 posters have been published/presented throughout the duration of this project. In addition, 3 journal articles are currently under preparation.

2 Project Milestones and Subtasks (Budget Periods 1 & 2)

Task 1.0: Mono-facial mini-module fabrication (BP1) Task Summary: Acquire commercial module components, assemble and laminate mini-modules. Mono-facial mini-modules will be constructed with component variations including but not limited to mono- and bi-facial cells, transparent, white, and UV cutoff versions of EVA and POE encapsulants, and glass and polymer backsheets.

The milestones are:

- MS 1.1 (FY19Q3): Mini-module fabrication
  - Success Value: At least 4 samples each of set 1 glass-backsheet and glass-glass mini-module types fabricated by CWRU.
  - Assessment Tool: Count. At least 16 mini-modules of at least 4 different types will be fabricated at CWRU to match CSI-provided mini-modules.
  - Verification Process: Initial characterization results from mini-modules and CSI equivalents reported to DOE.
  - Metric Justification: Immediately fabricating both glass-backsheet and double-glass mini-modules to compare architecture performance.
- MS 1.2 (FY19Q4): Mini-module outdoor exposure
  - Success Value: At least 2 mini-modules of each of at least 8 types fielded outdoors in Cleveland, OH with P_{mp}, I-V time-series data.
  - Assessment Tool: Count. 16 mini-modules fielded outdoors with individual module-level I-V curve tracing.
  - Verification Process: Raw outdoor P_{mp}, I-V time-series data reported to DOE.
  - Metric Justification: Early fielding of mini-modules to obtain the maximum possible amount of outdoor data during the 3 years of the project.
- MS 1.3 (FY20Q1): Mini-module characterization
  - Success Value: Performance at least 4 characterization methods listed table 2 at each accelerated exposure step (500 hours DH) in 2 accelerated exposures through at least 2000 hours.
  - Assessment Tool: Count. Characterizations such as I-V, $Suns$-V_{oc}, EL, Raman, FTIR, or Fluorescence will be performed for each module, with data collected and stored in a high performance computing environment.
  - Verification Process: Data summary and preliminary time-series plots reported to DOE.
  - Metric Justification: At least 4 characterization to evaluate electrical, mechanical, and chemical degradation within the minimodule.

- MS 1.4 (FY20Q1): Mini-module accelerated exposures
  - Success Value: Conclude a minimum of 1 accelerated test with a minimum of 6 measurement steps on at least 3 samples.
  - Assessment Tool: Count. Stepwise measurements performed after every 500 hours DH or equivalent for test.
  - Verification Process: Data summary and time-series plots reported to DOE.
  - Metric Justification: 6 measurement steps required to accurately fit a model. Multiple samples of each type to obtain statistically relevant results.
- MS 1.5 (FY20Q1): Modeling of accelerated exposure result
  - Success Value: $< S|R >$ and $< S|M|R >$ models for at least 4 module types in at least 1 accelerated exposure. Rank- Ordered performance of included module types.
  - Assessment Tool: $< S|R >$ models indicate Rd of a chosen response. $< S|M|R >$ models indicate significant module degradation pathways. Rank-ordering a minimum of 4 module types by power loss and by rates of observed degradation modes using electrical, mechanical, and chemical characterization results.
  - Verification Process: Raw and analyzed data reported to DOE.
  - Metric Justification: $< S|R >$ power model gives the functional form and rate of power loss. By comparing the adjusted-R2 and RMSE of each pathway in an $< S|M|R >$ model, significant degradation modes can be identified.
- MS 1.6 (FY20Q3): Modeling of outdoor exposure results
  - Success Value: $< S|R >$ and $< S|M|R >$ models of time-series I-V for at least 8 module types in at least 9 months of outdoor exposure.
  - Assessment Tool: $< S|R >$ models indicate R_d of a chosen response. $< S|M|R >$ models indicate significant module degradation pathways. Rank-ordering a minimum of 8 module types by power loss and by rates of observed degradation modes.
  - Verification Process: Raw and analyzed data reported to DOE.
  - Metric Justification: $< S|R >$ power model gives the functional form and rate of power loss. By comparing the adjusted-R2 and RMSE of each pathway in an $< S|M|R >$ model, significant degradation modes can be identified.
- MS 1.7 (FY20Q3): Webinar/Workshop For PV Manufacturers and PV Plant Developers, Owners, Financiers, and IEA-PVPS working group.
  - Success Value: The audience includes members of the academic community, from the industry, and financiers / insurers. A minimum of 30 industry participants from at least 20 different companies Post- event survey/follow-up completed by a minimum of 50% of attendees.

  - Assessment Tool: The post-event survey / follow-up will collect feedback from participants including their assessment of the value of the results of this project as it relates to costs, reliability and cost basis.
  - Verification Process: Survey Responses and Summary sent to DOE, including changes to the project plan, based on the feedback received, if appropriate.
  - Metric Justification: Perspectives and feedback from industry will guide future project decisions, with emphasis on economic and commercial viability.

The subtasks are:

  - Subtask 1.1: Fabricate DG and GB mini-modules with mono-facial PERC cells, and UV-cutoff EVA and POE encapsulants (Set 1).
  - Subtask 1.2: Fabricate DG and GB mini-modules with bi-facial PERC cells, and opaque EVA and POE encapsulants (Set 2).
  - Subtask 1.3: Fabricate DG and GB mini-modules with mono-facial PERC cells, and opaque EVA and POE encapsulants (Set 3).

Task 2.0: Quantify degradation rates of mono-facial DG and GB minimodules (BP1)
Task Summary: Using $< Stressor|Response >$ predictive modeling techniques, the functional time dependence and rates of power and mechanistic degradation for mono-facial modules will be determined from accelerated and real-world exposure results. Accelerated tests will include stepwise chemical, mechanical and electrical evaluations, producing a variety of variables for time-series analysis.

The milestones are:

- MS 2.1 (FY21Q1): Mini-module accelerated exposures
  - Success Value: Conclude a minimum of 1 accelerated test with a minimum of 6 measurement steps of 4+ characterizations on at least 3 samples of each of 8 module types.
  - Assessment Tool: Count. Stepwise measurements performed after every 500 hours DH or equivalent for test.
  - Verification Process: Data summary and time-series plots reported to DOE.
  - Metric Justification: 6 measurement steps required to accurately fit a model. Multiple samples of each type to obtain statistically relevant results.
- MS 2.2 (FY21Q2): Modeling of accelerated exposure results
  - Success Value: $< S|R >$ and $< S|M|R >$ models for at least 8 module types in at least 2 accelerated exposures. Rank-ordered performance of included module types.
  - Assessment Tool: $< S|R >$ models indicate Rd of a chosen response $< S|M|R >$ models indicate significant module degradation pathways. Rank-ordering a minimum of 8 module types by power loss and by rates of observed degradation modes using electrical, mechanical, and chemical characterization results.

  - Verification Process: Raw and analyzed data reported to DOE.
  - Metric Justification: $< S|R >$ power model gives the functional form and rate of power loss. By comparing the adjusted-R2 and RMSE of each pathway in an $< S|M|R >$ model, significant degradation modes can be identified.

- MS 2.3 (FY21Q3): Modeling of outdoor exposure results

  - Success Value: $< S|R >$ and $< S|M|R >$ models of time-series I-V for at least 12 module types in at least 20 months of outdoor exposure.
  - Assessment Tool: $< S|R >$ models indicate Rd of a chosen response. $< S|M|R >$ models indicate significant module degradation pathways. Rank-ordering a minimum of 12 module types by power loss and by rates of observed degradation modes.
  - Verification Process: Raw and analyzed data reported to DOE.
  - Metric Justification: $< S|R >$ power model gives the functional form and rate of power loss. By comparing the adjusted-R2 and RMSE of each pathway in an $< S|M|R >$ model, significant degradation modes can be identified.

- MS 2.4 (FY21Q3): Mini-module fabrication (Set 5)

  - Success Value: At least 4 samples each of a minimum of 2 new mini- module types determined from modeling and Sets 1-4 results fabricated by CWRU.
  - Assessment Tool: Count. At least 8 mini-modules of at least 2 different types will be fabricated at CWRU to match CSI-provided mini-modules.
  - Verification Process: Initial characterization results from mini-modules and CSI equivalents reported to DOE.
  - Metric Justification: Optimized module architectures derived from mechanical modeling, and outdoor and accelerated testing results of mini-module Sets 1-4 will be fabricated.

- MS 2.5 (FY21Q4): Mini-module characterization (Set 5)

  - Success Value: Perform at least 5 characterization methods such as those listed in Table 2 at each accelerated exposure step (500 hours DH) in 2 accelerated exposures through at least 2000 hours.
  - Assessment Tool: Count. Characterizations such as I-V, Suns-VOC, EL, Raman, FTIR, or Fluorescence will be performed for each module, with data collected and stored in a high performance computing environment.
  - Verification Process: Data summary and preliminary time-series plots reported to DOE.
  - Metric Justification: At least 5 characterizations to evaluate electrical, mechanical, and chemical degradation within mini-modules. 1 characterization method added based on learnings from results of Sets 1-4.

The subtasks are:

- Subtask 2.1: Outdoor fielding of mono- and bi-facial DG and GB mini-modules.
- Subtask 2.2: Mechanical modeling of cells, packaging materials & mini-modules.
- Subtask 2.3: Accelerated exposures of mini-modules with step-wise evaluations (Set 1).
- Subtask 2.4: $< Stressor|Response >$ modeling of accelerated exposure time-series results. (Set 1).
- Subtask 2.5: Accelerated exposures of mini-modules with step-wise evaluations (Set 2).
- Subtask 2.6: $< Stressor|Response >$ modeling of accelerated exposure time-series results (Set 2).
- Subtask 2.7: $< Stressor|Response >$ modeling of outdoor PMP/I-V time-series results (Sets 1-3).
- Subtask 2.8: Accelerated exposures of mini-modules with step-wise evaluations (Set 3).
- Subtask 2.9: $< Stressor|Response >$ modeling of accelerated exposure time-series results (Set 3).

Task 3.0: Identify degradation modes specific to DG and GB minimodules to optimize packaging (BP1) Task Summary: Using $< Stressor|Mechanism|Response >$ models, the most significant degradation pathways for each minimodules architecture can be inferred. By comparing results between architectures with varying components, the most and least degradation-susceptible cells and packaging materials can be identified. Comparing time-series measurements from outdoor and accelerated testing via Indoor/Outdoor cross-correlation confirms the commonality of degradation modes activated in these weathering conditions.

The subtasks are:

- Subtask 3.1: $< Stressor|Mechanism|Response >$ inferential pathway model on accelerated results (Set 1).
- Subtask 3.2: $< Stressor|Mechanism|Response >$ inferential pathway model on accelerated results (Set 2).
- Subtask 3.3: $< Stressor|Mechanism|Response >$ inferential pathway model on 1 year of outdoor $I\text{-}V/PMP$ (Sets 1-3).
- Subtask 3.3: Indoor/Outdoor cross-correlation with 1 year of outdoor I-V/PMP time-series data (Sets 1-2).
- Subtask 3.4: $< Stressor|Mechanism|Response >$ inferential pathway model (Set 3).

Task 4.0: Stakeholder engagement and dissemination of results (BP1) Task Summary: The recipient will engage with relevant stakeholders and disseminated the results of this award through activities including but not limited to participation and/or presentations at technical conference, in-person meetings, scientific or technical publications.

Task 5.0: Bi-facial and advanced mini-module fabrication (BP2) Task Summary: Acquire commercial module components, assemble and laminate mini-modules. Bi-facial mini-modules will be constructed with component variations including but not limited to bi-facial cells, transparent EVA and POE encapsulants, and glass and polymer backsheets. Advanced mini-module architectures will be determined from mono- and bi-facial module results.

The subtasks are:

- Subtask 5.1: Fabricate DG and GB mini-modules with bi-facial PERC cells, transparent EVA and POE encapsulants, and transparent back glass or polymer backsheets (Set 4).
- Subtask 5.2: Fabricate DG and GB mini-modules with optimized architectures based on the results from mono- and bi-facial mini-modules (Set 5).

Task 6.0: Quantify degradation rates of mono- and bi-facial DG and GB mini-modules (BP2) Task Summary: Using $< Stressor|Response >$ predictive modeling techniques, the functional time-dependence and rates of power and mechanistic degradation for mono-facial modules will be determined from accelerated and real-world exposure results. Accelerated tests will include stepwise chemical, mechanical, and electrical evaluations, producing a variety of variables for time-series analysis.

- Subtask 6.1: $< Stressor|Response >$ modeling of outdoor PMP/I-V time-series results (Sets 1-4).
- Subtask 6.2: Accelerated exposures of mini-modules with step-wise evaluations (Set 4).
- Subtask 6.3: $< Stressor|Response >$ modeling of accelerated exposure time-series results (Set 4).
- Subtask 6.4: Accelerated exposures of mini-modules with step-wise evaluations (Set 5).
- Subtask 6.5: $< Stressor|Response >$ modeling of accelerated exposure time-series results (Set 5).
- Subtask 6.6: $< Stressor|Response >$ modeling of outdoor $PMP/I\text{-}V$ time-series results (Sets 1-4).

Task 7.0: Identify degradation modes specific to DG and GB mini-modules to optimize packaging (BP2) Task Summary: Using $< Stressor|Mechanism|Response >$ models, the most significant degradation pathways for each mini-module architecture can be inferred. By comparing results between architectures with varying components, the most and least degradation-susceptible cells and packaging materials can be identified. Comparing time-series measurements from outdoor and accelerated testing via Indoor/Outdoor cross-correlation confirms the commonality of degradation modes activated in these weathering conditions.

- Subtask 7.1: $< Stressor|Mechanism|Response >$ inferential pathway model on 1.5-2 years of outdoor $I\text{-}V/PMP$ (Sets 1-4).
- Subtask 7.2: Indoor/Outdoor cross-correlation with 1.5-2 years of outdoor I-V/PMP (Sets 1-3).
- Subtask 7.3: $< Stressor|Mechanism|Response >$ inferential pathway model on accelerated results (Set 4).
- Subtask 7.4: $< Stressor|Mechanism|Response >$ inferential pathway model of accelerated results (Set 5).
- Subtask 7.5: $< Stressor|Mechanism|Response >$ inferential pathway model on full project length outdoor $I\text{-}V/PMP$ (Sets 1-4).
- Subtask 7.6 Indoor/Outdoor cross-correlation with full project length outdoor $I\text{-}V/PMP$ (Sets 1-4).

Task 8.0: Stakeholder engagement and dissemination of results (BP2) Task Summary: The recipient will engage with relevant stakeholders and disseminate the results of this award through activities including but not limited to participation and/or presentations at technical conferences, in-person meetings, scientific or technical publications.

EOP-A (FY22Q1): Major Degradation Mechanisms vs. GB/DG, EVA/POE, mono-/bi-facial cells and modules (BP2)

- Success Metric: $< S|M|R >$ pathways indicate at least 3 significant degradation pathways for at least 12 different module types in accelerated exposures.
- Assessment Tool: Rank-ordering a minimum of 3 significant degradation pathways in the $< S|M|R >$ models for a minimum of 12 module types in 2 accelerated exposures.
- Verification Process: Raw and analyzed data reported, sent to DOE.
- Metric Justification: Most significant degradation modes can be identified from $< S|M|R >$ models of each module type.

EOP-B (FY22Q1): Indoor/Outdoor Cross-correlation of Mini-module Sets 1-4 (BP2)

- Success Value: Best representative accelerated test determined from indoor/outdoor cross-correlation. Cross-correlation scale factor ($CCSF$) $<$ 0.5, power cross-correlation coefficient (CCC) $>$ 0.7.
- Assessment Tool: $CCSF$ determined from scaling indoor accelerated test results to outdoor performance. CCC calculated for power performance (P_{mp}) and degradation mechanisms and responses ($I\text{-}V$ features) between outdoor and time-scaled indoor data.
- Verification Process: Raw and analyzed data reported, sent to DOE.

- Metric Justification: $CCSF$ indicates whether an accelerated test degrades a module "faster" than outdoor exposure. $CCSF$=0.5 indicates twice as fast. Power CCC is the metric for module performance. CCC for mechanistic I-V features indicates whether the accelerated test induces the same degradation modes as outdoor fielding.

EOP-C: Rev. 2.0 Module Architectures (BP2)

- Success Value: $< S|R >$ power models and $< S|M|R >$ models quantifying at least 3 significant degradation modes for at least 12 different module types in accelerated exposures.
- Assessment Tool: $< S|R >$ models indicate Rd of a chosen response. $< S|M|R >$ models indicate significant module degradation pathways. Rank-ordering a minimum of 12 module types by power loss and by rates of 3+ significant degradation modes resulting from accelerated exposures.
- Verification Process: Raw and analyzed data reported, sent to DOE.
- Metric Justification: $< S|R >$ power model gives the functional form and rate of power loss. $< S|M|R >$ models of each degradation pathway compared for different module types, and rank-ordered to determine the best combination of module components to mitigate each degradation mode..

EOP-D: Dissemination: Publications (Journals & trade articles and Tools) (BP2)

- Success Value: 2 additional articles or proceedings, and participation in 2 conferences.
- Assessment Tool: Count. A minimum of 2 peer-reviewed journal articles or conference proceedings papers (in addition to those from BP1) disseminating project findings. Participation in a minimum of 2 national or international conferences.
- Verification Process: Articles/proceedings sent to DOE.
- Metric Justification: Published results in the form of journal articles or conference proceedings will communicate findings with the community. Participation in conferences ensures timely and accurate industry views on project tasks.

3 Narrative on Tasks, Subtasks, Milestones and End Of Project (Budget Periods 1 & 2)

The narrative is divided into broader topics in which the specific tasks, subtasks, and milestones are highlighted. The completion and relevant budget periods are included where applicable.

3.1 Minimodule fabrication and characterization

3.1.1 Fabrication process

The minimodule fabrication in this project was completed in BP1 and BP2 as part of:

- MS 1.1, 2.4
- ST 1.1, 1.2, 1.3, 5.1, 5.2

Four-cell PV minimodules were fabricated for studying degradation behavior under different exposure conditions. Five different sets of minimodules were fabricated with variations in the cell type, encapsulation, and backsheet (in the case of GB minimodules). This includes novel packaging strategies like co-extruded EPE that have only been recently introduced in the industry.

The fabrication process during BP1 and BP2 took place at two manufacturing facilities: CSI and CWRU. The fabrication processes were slightly different across CSI and CWRU. CSI adopted a more automated soldering process and maintained greater uniformity in the fabrication process and recipes. CWRU, on the other hand, tried to be consistent with the methods used by CSI but due to instrumentation differences, there were differences in soldering and lamination recipes.

The process of fabrication done by CSI includes the following steps in order: cell sorting, automatic soldering, soldering tabs for a specific layout, lamination, checking electroluminescence (EL) images, checking electrical properties and junction boxes installation. Figure 1 shows how several steps are carried in the production line.


(a) Cell transportation for sorting.

(b) Automatic soldering for ribbons.

(c) Hand-soldering for tabs.

Figure 1: CSI minimodule fabrication assembling line.

The process of fabrication done by CWRU includes the following steps in order: hand-soldering, lamination, electroluminescence (*EL*) image check and junction box installation.

Both CSI and CWRU were responsible for fabricating 48 minimodules each from sets #1-#4 and 40 minimodules from set #5 (including retained minimodules) combined. Across 5 sets, 232

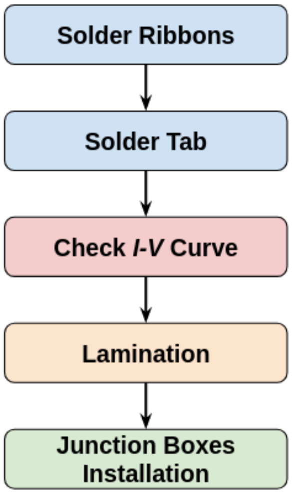

Figure 2: Module Fabrication Process at CWRU

minimodules were fabricated. Table 1 shows the minimodule quantities and specifications across all the sets. In addition, we fabricated 120 1-cell minimodules for mechanical testing studies conducted at NREL. Figure 3 shows the front and back view of a 4-cell minimodule from the study.

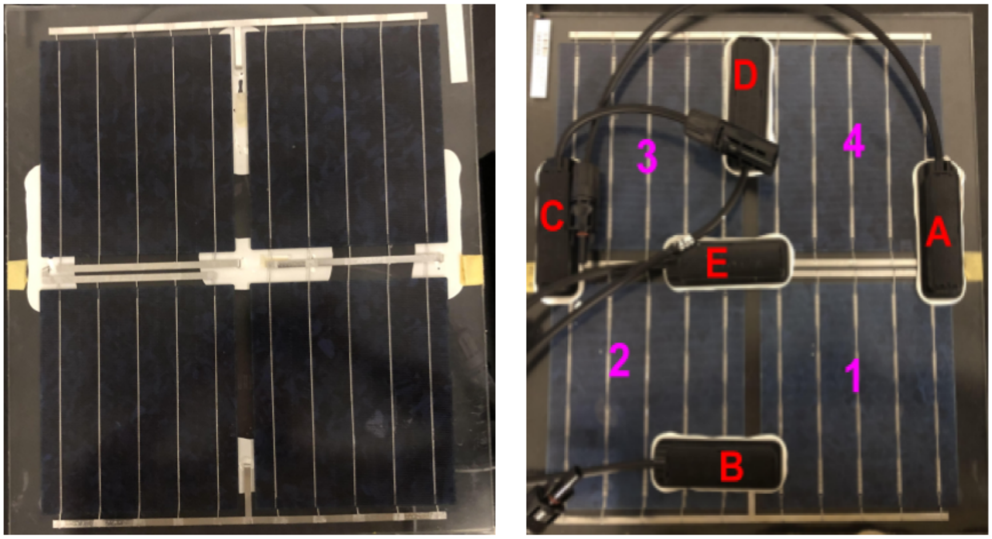

Figure 3: Representative 4-cell minimodule with front and back views.

In the fabrication process across different manufacturers, we used various materials such as glass, encapsulants, backsheets, PERC silicon cells, ribbon and bus wires, flux, junction boxes, and junction box potting materials. The details of the specific components used are summarized below.

- Glass: Based on the glass choice for commercial modules from several large companies and through internal team discussions, we decided to use 3.2mm tempered glass for GB minimodules and 2.5mm heat-strengthened glass for DG minimodules. Irrespective of thickness,

Table 1: Quantities and specifications of minimodules fabricated and tested. mDH represents modified damp heat, mDH+FSL represents the sequential exposure of modified damp heat with full-spectrum light.

Set #	MM Variant	# of MMs		# Retained	# Outdoor	# mDH	# mDH+FSL	Cell Type	Encap. Material	Rear Encap.	Architecture	Module Type
		Brand A	Brand B									
1	1	6	6	2	2	4	4	mono-facial	EVA	UV-Cut	GB	monofacial
1	2	6	6	2	2	4	4	mono-facial	EVA	UV-Cut	DG	monofacial
1	3	6	6	2	2	4	4	mono-facial	POE	UV-Cut	GB	mono-facial
1	4	6	6	2	2	4	4	mono-facial	POE	UV-Cut	DG	monofacial
2	5	6	6	2	2	4	4	bi-facial	EVA	Opaque	GB	monofacial
2	6	6	6	2	2	4	4	bi-facial	EVA	Opaque	DG	monofacial
2	7	6	6	2	2	4	4	bi-facial	POE	Opaque	GB	monofacial
2	8	6	6	2	2	4	4	bi-facial	POE	Opaque	DG	monofacial
3	9	6	6	2	2	4	4	mono-facial	EVA	Opaque	GB	monofacial
3	10	6	6	2	2	4	4	mono-facial	EVA	Opaque	DG	monofacial
3	11	6	6	2	2	4	4	mono-facial	POE	Opaque	GB	monofacial
3	12	6	6	2	2	4	4	mono-facial	POE	Opaque	DG	monofacial
4	13	6	6	2	2	4	4	bi-facial	EVA	UV-Cut	GB	bifacial
4	14	6	6	2	2	4	4	bi-facial	EVA	Transparent	DG	bifacial
4	15	6	6	2	2	4	4	bi-facial	POE	UV-Cut	GB	bifacial
4	16	6	6	2	2	4	4	bi-facial	POE	Transparent	DG	bifacial
5	17	0	6	2	0	2	2	bi-facial (new)	POE	UV-Cut	GB	bifacial
5	18	3	6	3	0	2	4	bi-facial (new)	POE	Transparent	DG	bifacial
5	19	0	6	2	0	2	2	bi-facial (new)	EPE	UV-Cut	GB	bifacial
5	20	3	6	3	0	2	4	bi-facial (new)	EPE	Transparent	DG	bifacial

the glass used for minimodules has textured side on the side facing the encapsulant, but has no texture on the air side. We have utilized small rectangular glass for making 1-cell minimodules for 4-point bend testing at NREL, which helped in deciding the loading conditions for the 4-point proof loading studies at CWRU, and enabled correlation with mechanical tests of bare cells. The dimensions of the glass were different (square versus rectangular).

- Encapsulants & backsheets: We ordered various encapsulants frequently in small rolls to avoid expiration. We kept the encapsulant weights consistent across manufacturing facilities. The encapsulants used in minimodules were ethylene vinyl acetate (EVA), polyolefin elastomer (POE) and co-extruded EPE, which is a multilayered EVA-POE-EVA encapsulant. The front side encapsulation for all minimodules was transparent. Depending on the set #, we used transparent/UV-cutoff/opaque rear encapsulation. We used KPf (sets #1-3), transparent backsheet with white grids (set #4) and transparent backsheet with no white grids (set #5).
- Cells: We used monofacial & bifacial multi-Si full-size PERC cells. CSI has provided 550 cells of each type for fabricating sets #1-#4 4-cell minimodules at CWRU. All of these cells have 5 busbars and are boron-doped. The cell size is about 150 mm. Additionally, CSI provided 120 mono-facial multi-Si full size PERC cell, 120 bi-facial multi-Si full size PERC cells and 120 mono-facial multi-Si full size Al-BSF cell for Weibull modulus testing carried out at NREL. This enabled the testing of cell durability of bare versus soldered cells, as well as in 1-cell minimodules. For set #5, we utilized the monofacial-Si bifacial P-type gallium-doped cells with 9 busbars. The cell size is about 167 mm. In comparison to the regular PERC cells utilized in the project, the cells used in set #5 had a short-circuit current value of about 11 A.

- Miscellaneous materials: This includes ribbon and bus wires, flux, junction boxes, and junction box potting materials. The dimension of the ribbons used were 0.85 × 0.27mm, and the dimension of tab is 4 × 0.23mm, which are the same dimensions used in CSI minimodules. At CWRU, we used a pen to apply organic flux to ribbons and tabs before soldering. After discussing with CSI, we decided to adopt their isopropanol flux application method which is to first soak the cut ribbons in the flux for about 20 minutes, then put it into the dryer, and finally put it on the cell for soldering. The junction boxes used were the same as CSI and shown in Fig 4. These small rectangular shaped junction box are easier to install and require less sealant.

(a) Front (b) Back

Figure 4: Picture of junction box

We have received samples of junction box junction and sealant from CSI. We have also purchased two types of caulk guns (Figure 5) for application.

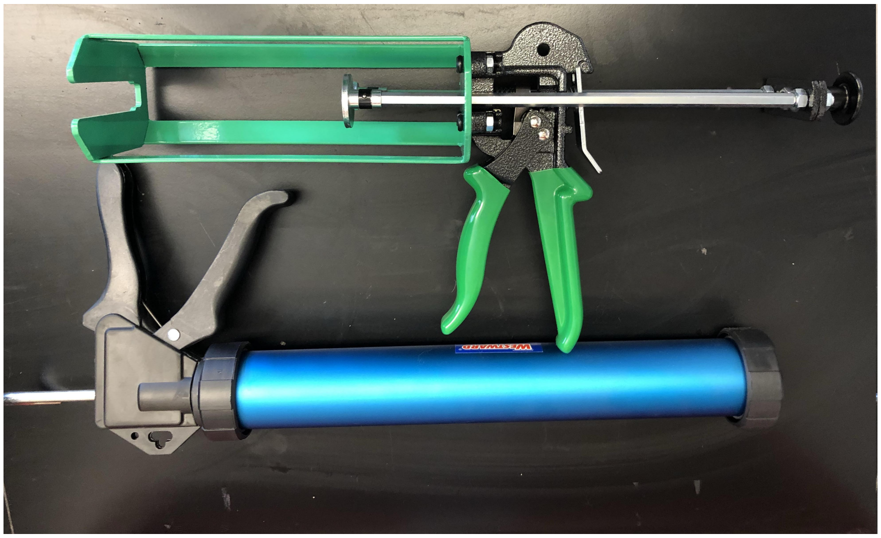

Figure 5: Caulk guns for potting materials and sealant

3.1.2 Mini-module characterization

The minimodule characterization in this project was completed in BP1 and BP2 as part of:

- MS 1.3, 2.5

The minimodule characterization techniques implemented in this project are I-V, $Suns\_V_{oc}$, electroluminescence (EL), electroluminescence (PL), and 4-point proof loading test. Stepwise characterization was performed using these techniques at the end of each exposure step (at 504 hours, equivalent to 21 days). In addition, extracted encapsulants from retained and exposed set #5 minimodules were characterized using colorimetry and Fourier-transform infrared spectroscopy (FTIR). This will be covered in Section 3.4.5.

- I-V: Current-voltage ($I-V$) curves provide information about the current and voltage at which the PV modules can be operated at fixed irradiance and temperature. Several different features can be extracted from $I-V$ curves including maximum power (P_{mp}), short circuit current (I_{sc}) (current at zero voltage), open circuit voltage (V_{oc}) (voltage at zero current), series resistance (R_s), fill factor (FF) (measure of 'squareness' of the $I-V$ curve), voltage at maximum power (V_{mp}), etc. Using $I-V$ curves and the extracted features, various losses can be tracked [1, 2].

  At each step, we measured the current-voltage (I-V) curves at three irradiance levels (1000 Wm^{-2}, 500 Wm^{-2} and 250 Wm^{-2}). The series resistance ($R_{s,IV}$) is extracted using all three I-V curves by following IEC 60891 [3]. The maximum power ($P_{mp,IV}$), short-circuit current (Isc,IV) are extracted from the I-V curve measured at 1000 W/m2 using the $ddiv$ package [4].

- $Suns$-V_{oc}: $Suns$-V_{oc} method measures the V_{oc} at different illumination levels. From $Suns$-V_{oc} curves, we could get an implied photovoltaic I-V curve and the curve of effective lifetime versus minority carrier density [5].

  In order to quantitatively compare the results, we extracted two features from implied photovoltaic I-V curves, P_{mp} and FF, and another two features from the curve, namely effective lifetime versus minority carrier density, they are the maximal effective lifetime in the unit of us and the corresponding minority carrier density under log10 scale. The $Suns$-V_{oc} measurements are taken for each cell in a minimodule.

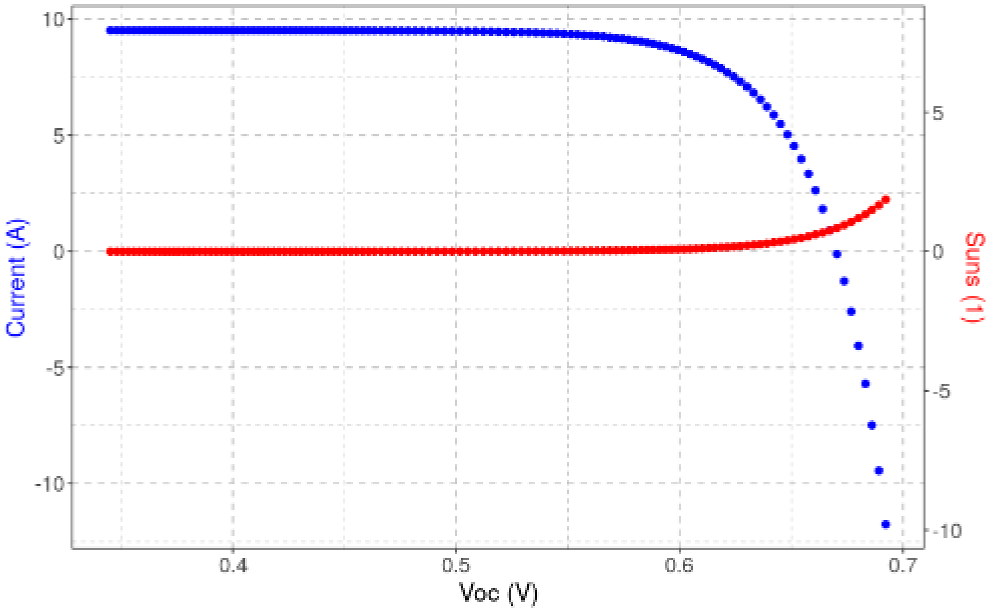

Figure 6: Implied I-V curve from $Suns$-V_{oc} curve.

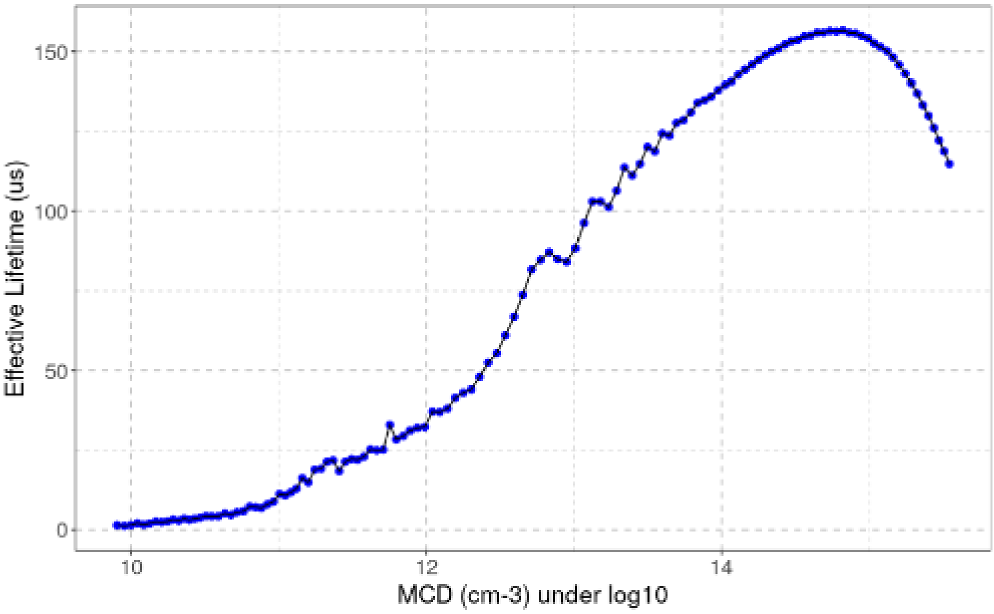

Figure 7: Effective lifetime vs. minority carrier density.

- EL/PL: Every EL & PL measurement contains 8 images in total- they are EL images taken at I_{sc}, $0.5I_{sc}$ and $0.25I_{sc}$, corresponding dark images (the same camera setting with no current input) and PL images at about 2 Suns irradiance and corresponding dark image (at the same irradiance and short-circuited conditions). For each signal of the minimodule image, first the corresponding dark image has to be subtracted followed by processing using the cell extraction pipeline with planar indexing[6]. After we obtain the cell images, for EL

measured at I_{sc}, we extract normalized busbar width (NBW) [7] and average intensity. Figure 8 shows the setup of EL/PL system.

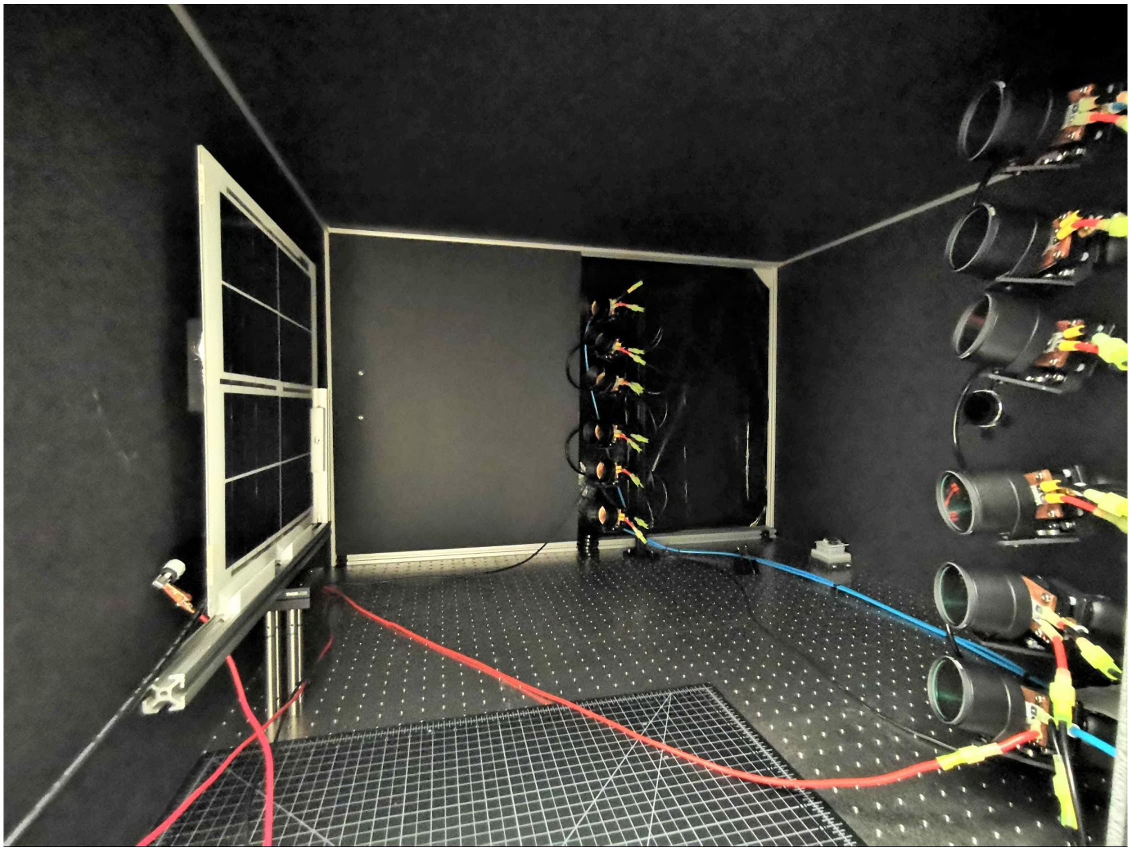

Figure 8: EL/PL system setup

- 4-point proof loading: 4-point bending was done on rectangular minimodules with GB architecture. The corresponding load versus load line displacement plots were constructed. These minimodules have two layouts: $||$ and $\perp$. $||$ is for the module with the busbars parallel to the width of the minimodule (short edge) and $\perp$ is for the ones with the busbars perpendicular to the width of the minimodule. This is illustrated in Figure 9. The 4-point proof loading setup is shown

(a) $||$ orientation

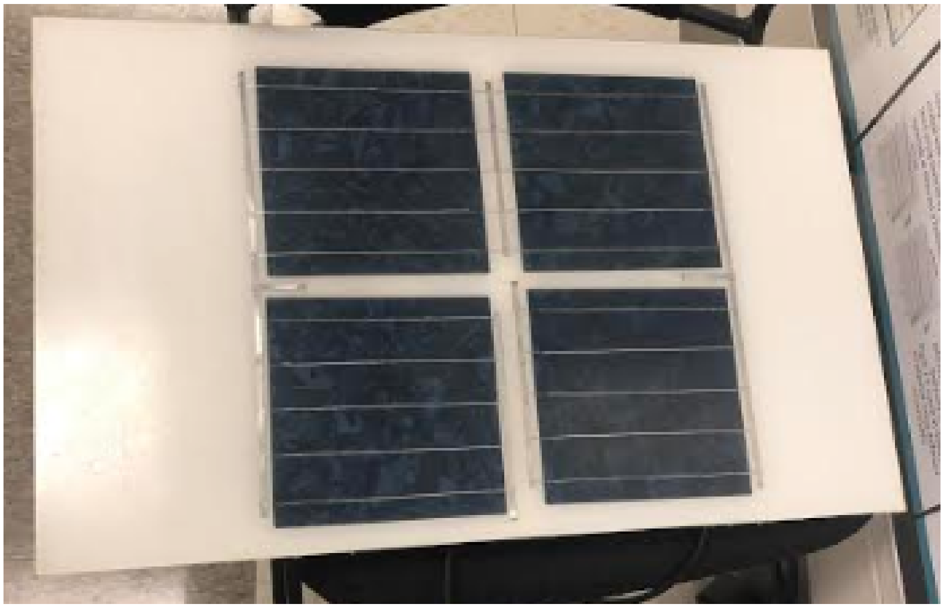

(b) $\perp$ orientation

Figure 9: The 4-cell minimodule layouts used in the 4-point proof loading.

3.2 Minimodule exposures

3.2.1 Indoor accelerated exposures

The minimodule indoor exposures in this project was completed as part of:

- MS 1.5, 2.1, 2.5

- ST 2.3, 2.5, 2.8, 6.2, 6.4

Before accelerated exposures, both CWRU and CSI minimodules were preconditioned to make sure the performance of the minimodules were able to achieve stability before being exposed. CSI preconditioning procedure includes two steps: outdoor exposure up to 40 $kW \cdot h/m^2$ and then current-induced degradation (CID) at current at maximum power (I_{mp}) for 48 hours at room temperature. CWRU preconditioning procedure was carried indoors since the minimodules that were fabricated were no longer suitable for outdoor preconditioning. The CWRU preconditioning procedure also includes two steps: indoor light exposure up to 40 $kW \cdot h/m^2$ and then current-induced degradation (CID) at current at maximum power (I_{mp}) for 48 hours at 80 $^{\circ}C$ and 40 % relative humidity. The minimodules from both suppliers were able to achieve stable status after preconditioning based on IEC 61215 draft (2019). Both CWRU and CSI minimodules achieved values of less than 1%.

The two types of accelerated exposures in this project are modified damp heat (mDH) and mDH with full spectrum light (mDH + FSL). mDH is 80 °C and 85 % relative humidity and FSL makes use of 420 W/m^2 light intensity. The total exposure time was 2520 hours, divided into five exposure steps. During the 504 hours (21 days) of each step, mDH took two-thirds of the exposure time (14 days), and FSL took one-third of the exposure time (7 days). The full spectrum light exposure was conducted with a class C solar simulator based on specialized HID lamps from Iwasaki Electric. The average light intensity on the front and back side of the exposed MM were 420.4 $\mathrm{W/m^2}$ and 85.1 $\mathrm{W/m^2}$ (due to reflection from walls of the chamber), respectively. A 0.5 Ω load resistor was connected to each MM to make it operate around the maximum power $P_{mp,IV}$. The minimodule temperature was controlled below 70 $^{\circ}\mathrm{C}$ under FSL. The primary purpose of FSL was to make the module fully operational, with the packages probably containing degradation products initiated from mDH. The number of minimodules exposed in either exposure conditions is listed in Table 1.

3.2.2 Outdoor exposure in SunFarm, Cleveland, OH

The minimodule outdoor exposures in this project was completed in BP1 and BP2 as part of:

- MS 1.2
- ST 2.1

Thirty-two minimodules of 16 variants with 2 minimodules under each variant were mounted on a tilted rack at an outdoor testing site in Cleveland in May 2020. We analyzed the data until December 2021, amounting to a total exposure period of 1.6 years. Only sets #1-#4 minimodules fabricated by CSI were exposed in outdoor conditions.

The 16 module variants have differences in encapsulant materials (EVA or POE), rear encapsulant types (transparent, UV-cutoff, or opaque), module architectures (GB or DG), and cell types (monofacial or bifacial). The backsheet used for monofacial GB minimodules is KPf, and that for bifacial GB minimodules including the transparent PVF-based backsheet. The detailed specifications are listed in Table 2.

The rack faced south with a tilted angle of 23°. The minimodules were arranged on the rack into three rows and eleven columns. So the distance from the minimodule to the ground

Table 2: Quantities and specifications of minimodules exposed in outdoor conditions.

Set #	MM Variant	# Outdoor	Cell Type	Encap. Material	Rear Encap.	Architecture	Module Type
1	1	2	mono-facial	EVA	UV-Cut	GB	monofacial
1	2	2	mono-facial	EVA	UV-Cut	DG	monofacial
1	3	2	mono-facial	POE	UV-Cut	GB	mono-facial
1	4	2	mono-facial	POE	UV-Cut	DG	monofacial
2	5	2	bi-facial	EVA	Opaque	GB	monofacial
2	6	2	bi-facial	EVA	Opaque	DG	monofacial
2	7	2	bi-facial	POE	Opaque	GB	monofacial
2	8	2	bi-facial	POE	Opaque	DG	monofacial
3	9	2	mono-facial	EVA	Opaque	GB	monofacial
3	10	2	mono-facial	EVA	Opaque	DG	monofacial
3	11	2	mono-facial	POE	Opaque	GB	monofacial
3	12	2	mono-facial	POE	Opaque	DG	monofacial
4	13	2	bi-facial	EVA	UV-Cut	GB	bifacial
4	14	2	bi-facial	EVA	Transparent	DG	bifacial
4	15	2	bi-facial	POE	UV-Cut	GB	bifacial
4	16	2	bi-facial	POE	Transparent	DG	bifacial

varies according to rows from 25 cm to 100 cm. The longitude and latitude of the testing site are -81.616° and 41.511°, respectively. This location belongs to the Dfa climate (continental, no dry season, hot summer) according to the Köppen-Geiger climate classification system. The time-series I-V curve for each module was recorded by the Daystar MT5 Multi-tracer in every ten minutes. A thermocouple was attached to each minimodule on the rear side around the center position of a cell to monitor module temperatures. A pyranometer was installed nearby to record the plane of array irradiance (POA). Both thermocouples and the pyranometer were connected to a data logger with the recording frequency as one minute. Both sources of data were merged using the closest measurement time. A POA limitation of 5 W/m^2 was applied to remove night observations.

3.3 Webinar/Workshop For PV Manufacturers and PV Plant Developers, Owners, Financiers, and IEA-PVPS working group

Organizing the T50 webinar is related to MS 1.7. The T50 workshop with up-to-date results from the project was held on August 18, 2020. The title of the workshop was 'Strategies of PV Modules with Lower Performance Loss Rates'. Some of the topics covered were PV Market Share of Glass/Backsheet and Double Glass Modules, Manufacturing Defects, Failure Modes, & Degradation Mechanisms in Modules, Cell Mechanics and Cracking, Towards 50: Results to Date, Instrumentation and Tools for PV Research. The workshop had 127 registered participants from both industry (81) and research institutions (46).

Figure 10 shows which PV fields people are associated with. The responses are gathered from people who responded to the survey questions. Some of the categories include PV systems, research, management, materials, operations and management, etc. More than 30% of the people who responded are from research and about 20% of the people are from manufacturing.

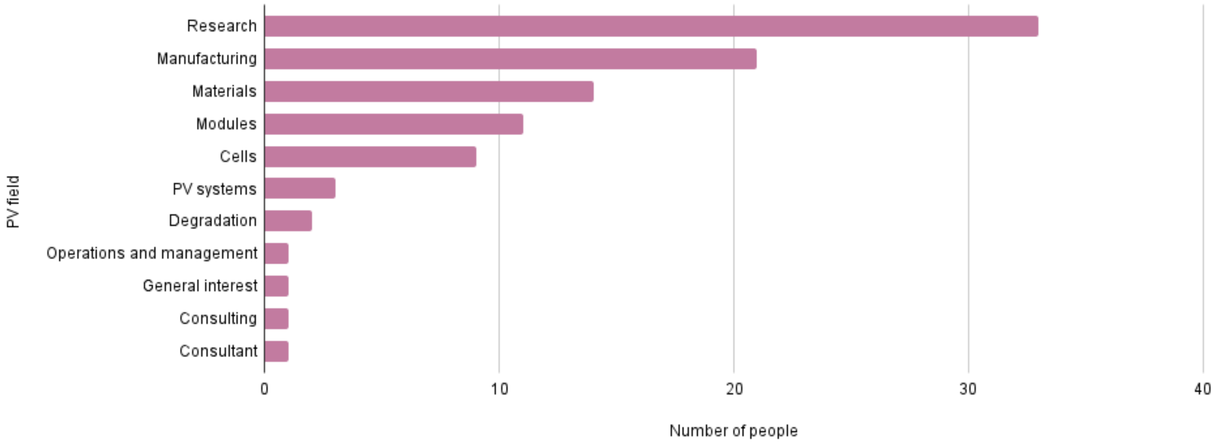

Figure 10: PV fields that registered participants are associated with. Only a certain number of people (97) from registered participants responded to this question.

Figure 11 shows the PV interests among registered participants. The most popular interest among participants is bifacial PV modules.

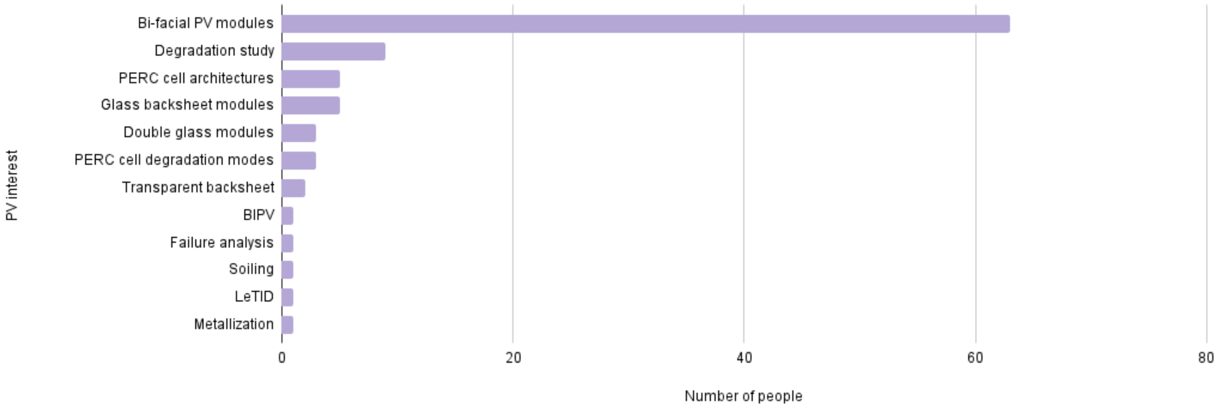

Figure 11: PV interests that registered participants have. Only a certain number of people (95) from registered participants responded to this question.

3.4 Results in the project

3.4.1 Accelerated exposure results

The minimodule characterization in this project was completed in BP1 and BP2 as part of:

- MS 1.5, 2.2
- ST 2.4, 2.6, 2.9, 3.1, 3.2, 3.4, 6.3, 6.5, 7.3, 7.4
- EOP-A, EOP-C

Most of these results will be part of our future publication. The results of all minimodule sets from #1 through #5 are compared. Statistical analysis using confidence intervals (CIs) and degradation pathway modeling using the Markovian principle will be shown using examples. Rank-ordering of the best- and worst-performing variants will be done using predictive 83.4% CIs.

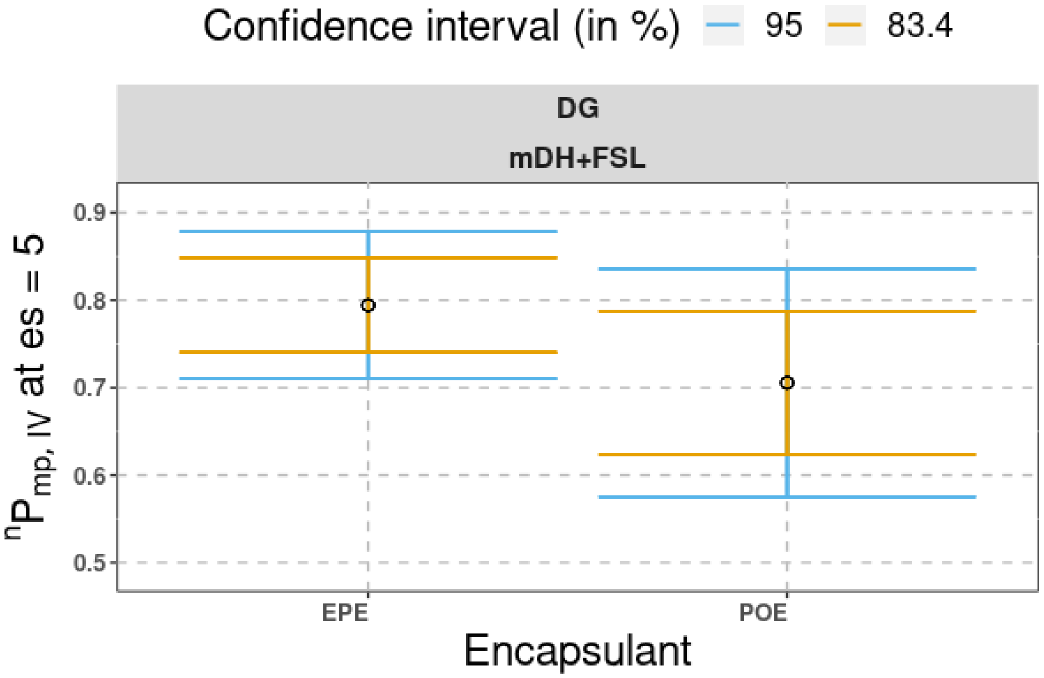

Figure 12: 83.4 % and 95 % CIs of ${}^nP_{mp,IV}$ at final exposure step (i.e., step 5) for minimodule variants fabricated by Manufacturer A.

83.4 % (orange) and 95 % (blue) CIs were constructed for various minimodule variants. Here,we show results for set #5 minimodules as an example. Figure 12 shows the results for the set #5 DG minimodules, which were exposed in mDH+FSL conditions and fabricated by Manufacturer A. The average power loss for DG with POE is more than the one with EPE. Due to overlap in the 83.4 % and 95 % CIs, the minimodules may be behaving similarly as per inference by eye [8, 9].

Figure 13 shows the results for set #5 minimodule variants fabricated by Manufacturer B. The average power loss for DG with EPE exposed in mDH+FSL is greater than the rest of the variants. There is significant CI overlap between minimodule variants. In some cases, there is widening of CIs (especially for DG with POE in mDH and GB with EPE in mDH+FSL), suggesting that the data points may have high variability and do not provide a precise population mean estimate [9].

Rank-ordering of minimodule variants was done using predictive 83.4 % CIs using the Markovian principle. Predictive CIs can provide insights into how degradation occurs throughout the

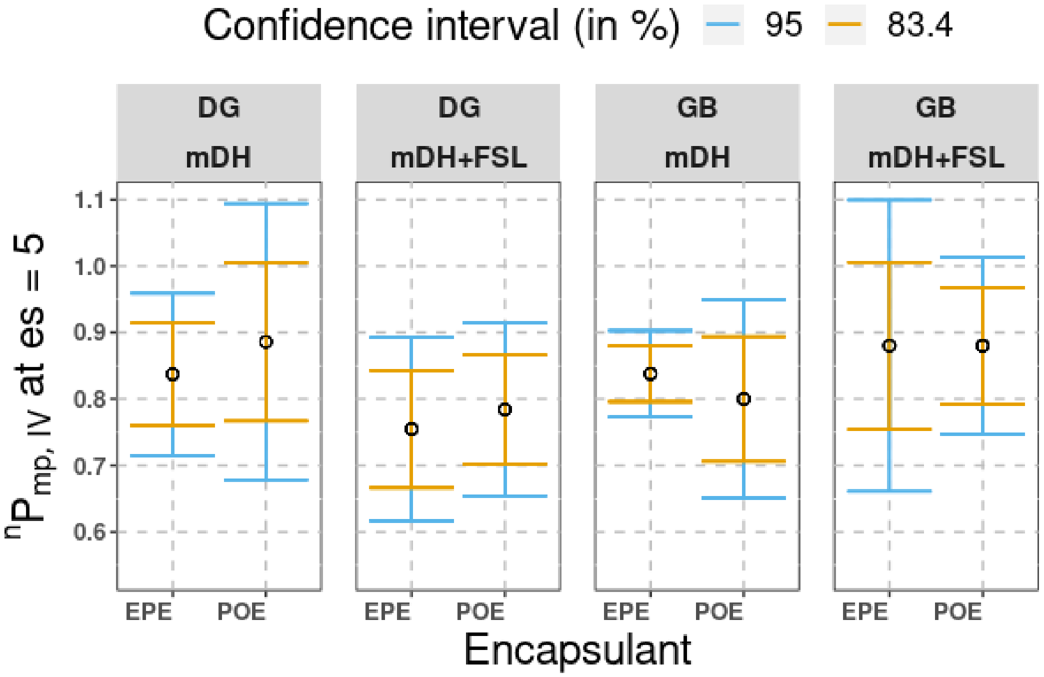

Figure 13: 83.4 % (orange) and 95 % (blue) CIs of $^nP_{mp,IV}$ at final exposure step (i.e., step 5) for minimodule variants fabricated by Manufacturer B.

exposure cycle by providing uncertainty in estimated mean [10]. Figs 14 and 15 show the predictive CIs for various minimodule variants from sets #1-#5. Some of the variants do not have a predictive CI due to the absence of pathway from exposure time (dy) to $^nP_{mp,IV}$. A similar analysis was done in our previous work [10].

For set #5, the estimated means from the predictive CIs are lower than the 83.4% CI estimated means and the predictive CIs are also wider in comparison. The predictive CIs have a significant overlap across encapsulants, which seems to indicate that the degradation behavior is similar throughout the exposure cycle. Set #5 appears to be degrading the most over the exposure cycle. There is variability in the widths of CIs of variants made by different manufacturers, indicating some differences in the quality control. Based on the estimated means from predictive CIs, we can rank-order variants to identify durable and degrading variants. Table 3 shows the durable and degrading variants along with estimated mean values across all the sets. In addition, the top five variants in each category are displayed.

We observe that there are three variants that have no direct pathway between dy and $^nP_{mp,IV}$: this signifies stability. The three most durable variants are GB-based and were fabricated by Manufacturer A. Most of the durable variants are from sets #1 and #4. There seems to be no strong trend of any particular encapsulant or module architecture being better by considering durable categories in Table 3. mDH+FSL is a realistic exposure in which high temperature, high humidity, and exposure to light are included: most of the durable variants appear to be stable in mDH+FSL conditions. There is an apparent dependence of manufacturer and exposure conditions on the performance of minimodules from the rank-ordering results.

Figure 16 shows the $< Stressor|Mechanism|Response >$ ($< S|M|R >$) model of a de-

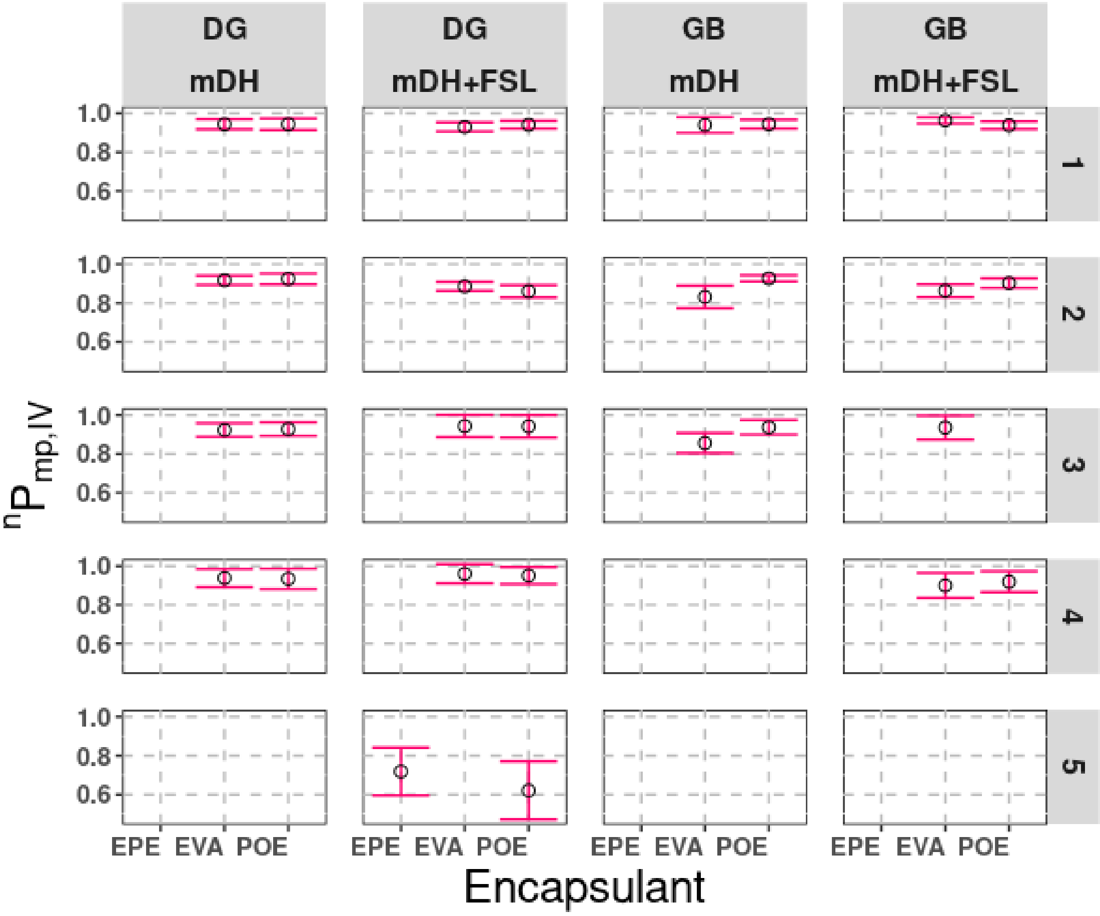

Figure 14: Predictive 83.4 % confidence intervals for minimodule variants fabricated by Manufacturer A.

Table 3: Rank-ordering durable and degrading variants based on predictive 83.4% confidence intervals. The variants with no degradation pathway indicates that there is no direct pathway between dy and ${}^{n}P_{mp,IV}$.

Set	Manufacturer	Encapsulant	Architecture	Exposure	Estimated mean	Category
4	A	EVA	GB	mDH	-	Durable (no degr. path)
4	A	POE	GB	mDH	-	Durable (no degr. path)
3	A	POE	GB	mDH+FSL	-	Durable (no degr. path)
1	B	EVA	DG	mDH+FSL	0.98	Durable
1	B	POE	DG	mDH+FSL	0.98	Durable
1	A	EVA	GB	mDH+FSL	0.96	Durable
4	A	EVA	DG	mDH+FSL	0.96	Durable
4	A	POE	DG	mDH+FSL	0.95	Durable
5	B	POE	GB	mDH	0.76	Degrading
5	B	POE	DG	mDH+FSL	0.76	Degrading
5	A	EPE	DG	mDH+FSL	0.72	Degrading
5	B	EPE	DG	mDH+FSL	0.66	Degrading
5	A	POE	DG	mDH+FSL	0.62	Degrading

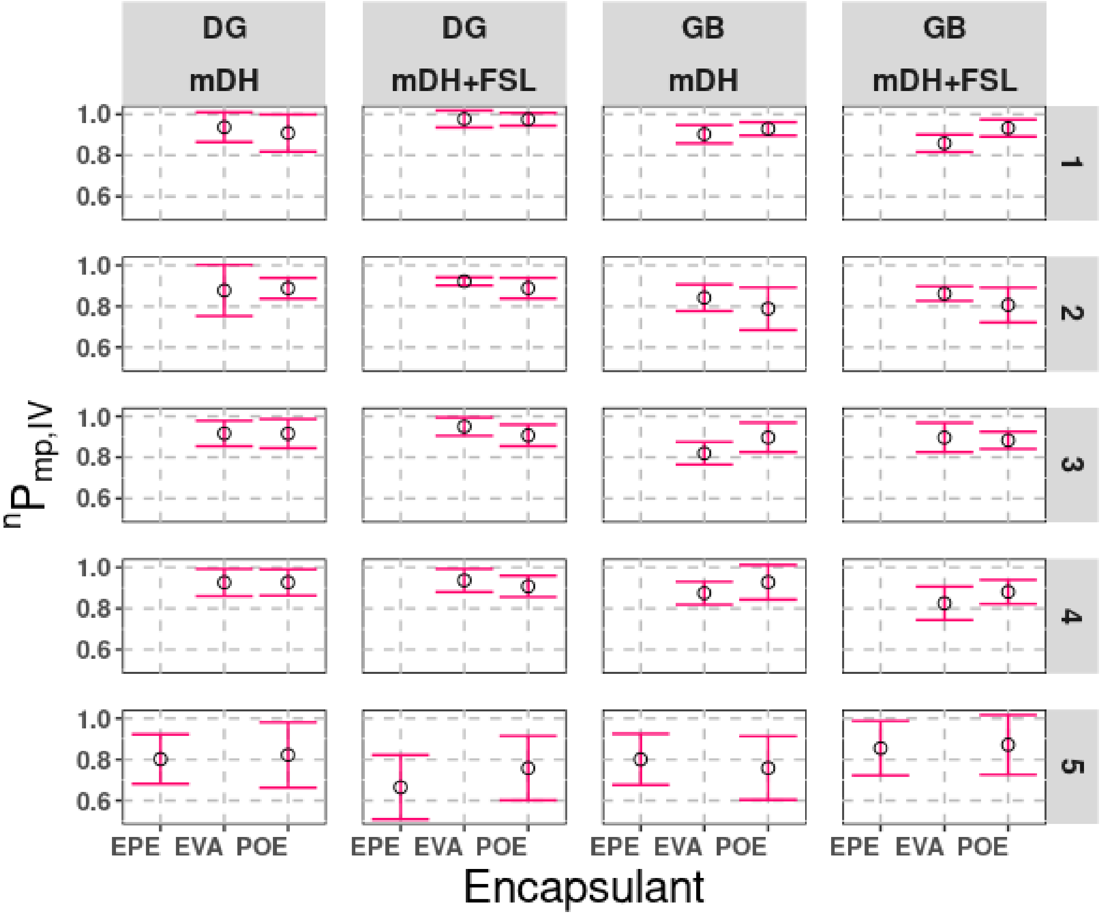

Figure 15: Predictive 83.4 % confidence intervals for minimodule variants fabricated by Manufacturer B.

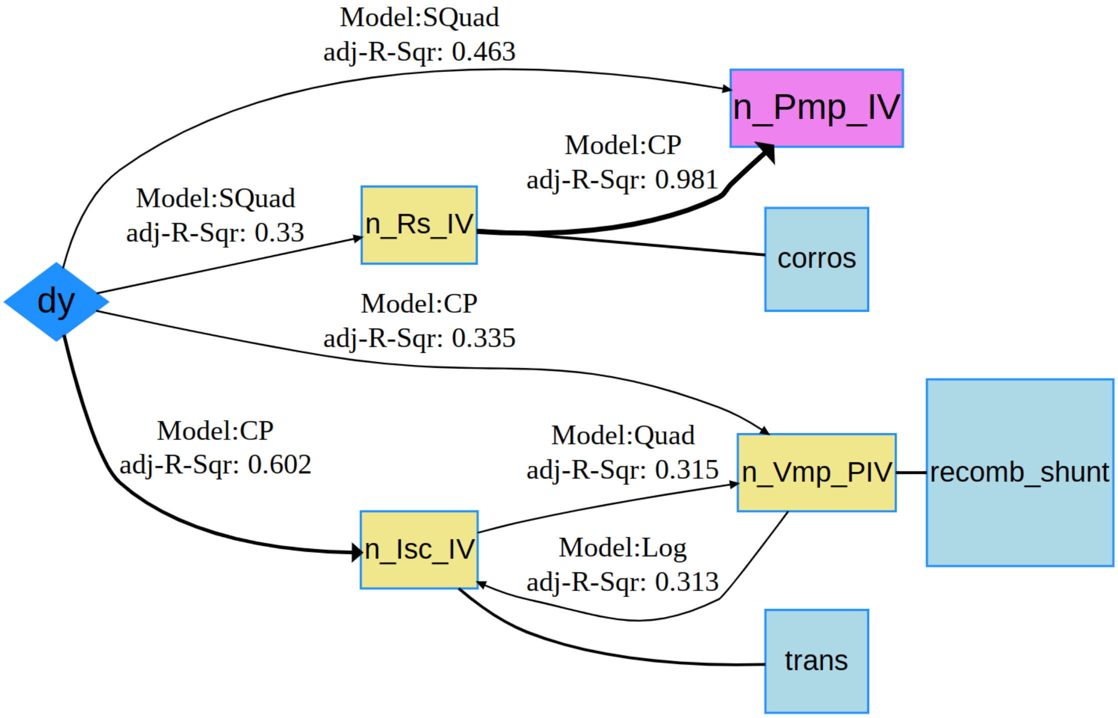

Figure 16: $< Stressor|Mechanism|Response >$ model of DG with EPE in mDH+FSL fabricated by Manufacturer A obtained using Markovian principle. dy is exposure time (stressor) and ${}^{n}P_{mp,IV}$ is maximum power, which is the response. ${}^{n}I_{sc,IV}$ indicates short-circuit current, ${}^{n}R_{s,IV}$ indicates series resistance, and ${}^{n}V_{mp,PIV}$ indicates voltage at maximum power (IV means that the measurement is from current-voltage data whereas PIV means it is a $Suns\text{-}V_{oc}$ measurement). The blue boxes indicate the degradation mode that the variable tracks: ${}^{n}I_{sc,IV}$ tracks optical transmission loss, ${}^{n}R_{s,IV}$ monitors corrosion, and ${}^{n}V_{mp,PIV}$ tracks recombination and shunting.

grading set #5 minimodule variant, DG with EPE in mDH+FSL, which was fabricated by Manufacturer A. The pathway between dy and ${}^{n}P_{mp,IV}$ is referred to as the direct pathway or $< S|R >$. The pathway between dy and any mechanistic variable (M_i) is $< S|M|$ whereas the pathway between M_i and ${}^{n}P_{mp,IV}$ is $< M|R >$. This model was obtained from the netSEM package using the Markovian principle. In order for the variant to be strongly impacted by a time-dependent mechanistic variable, the R^2_{adj} values should be significant in $< S|M|$ and $< M|R >$. It is apparent that the dominant degradation pathway is ${}^{n}R_{s,IV}$ as there is a well-defined $< S|M|$ and $< M|R >$. The rest of the mechanistic variables do not have $< M|R >$ due to R^2_{adj} being less than 0.01.

Figure 17 shows how ${}^{n}P_{mp,IV}$ changes with dy for set #5 minimodule variants. This is referred to as the $< S|R >$ pathway in the $< S|M|R >$ model. It can be observed that all of the minimodule variants, irrespective of whether they were fabricated by Manufacturer A or B, experience some extent of power loss. On average, the power loss is at least 10 % across all variants. Among the DG minimodules fabricated by Manufacturer A and exposed in mDH+FSL, the one with EPE has greater stability than the one with POE. Under the influence of mDH+FSL, GB minimodules fabricated by Manufacturer B seem to have similar power loss. In mDH exposure, DG with POE fabricated by manufacturer B has the least amount of power loss among the other variants.

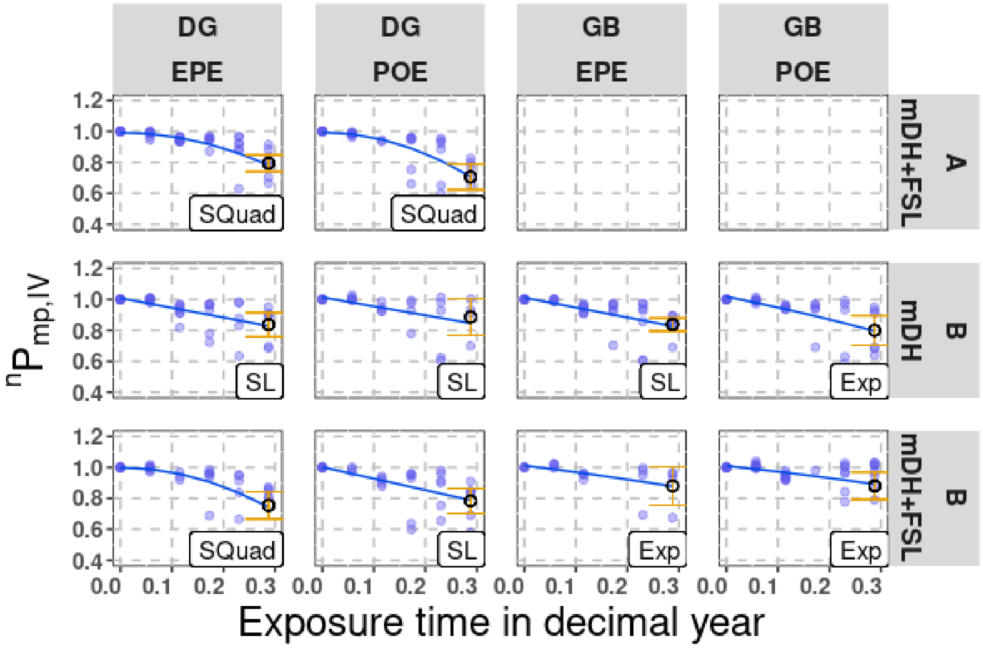

Figure 17: Variation of ${}^{n}P_{mp,IV}$ with dy ($< S|R >$) fabricated by Manufacturers A and B for set #5 minimodules. The best model equation line and name in text, data points, and 83.4% CIs (orange) at the end of exposure cycle are shown.

Figure 18 shows how ${}^{n}P_{mp,IV}$ changes with dy for durable/degrading variants that have been rank-ordered using predictive 83.4% CIs. Each plot represents a particular minimodule variant named in the order of manufacturer, encapsulant, module architecture, exposure type, and set number. The plots are arranged in the order of durable to degrading. The results are consistent between $< S|R >$ and statistical analysis.

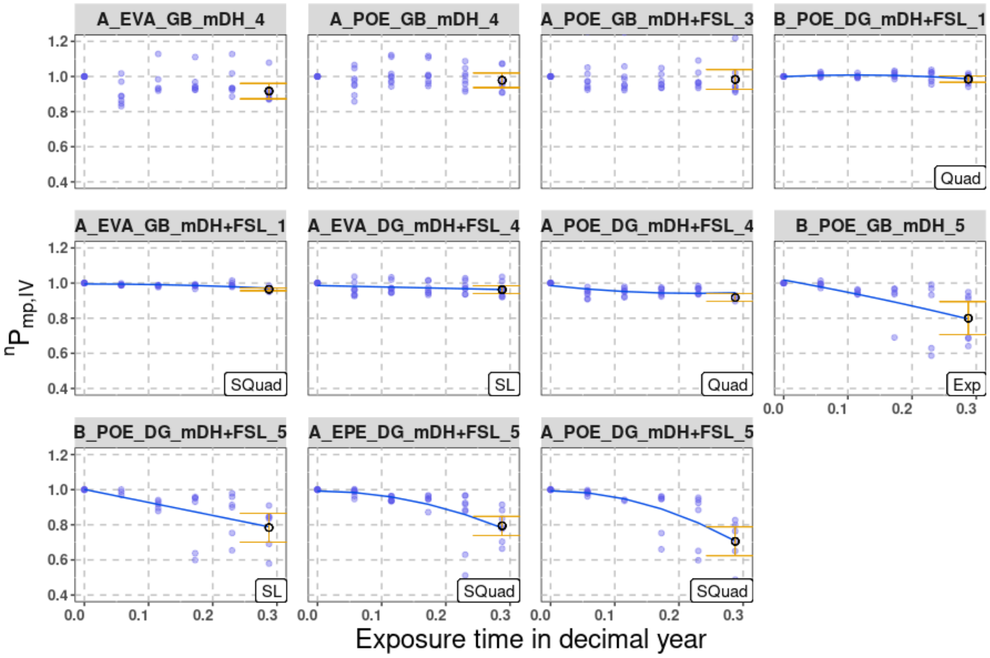

Figure 18: Variation of ${}^{n}P_{mp,IV}$ with dy ($< S|R >$) for durable and degrading variants based on 83.4 % predictive CIs. The best model equation line and name in text, data points, and 83.4 % CIs (orange) at the end of exposure cycle are shown.

To compare between minimodule sets, the variant DG with POE fabricated by Manufacturer A was chosen as an example (this will be referred to as minimodule variant from here on). Figure 19 shows how the variant changes with each set. Even though the variant name is the same across all the sets, the cell type and the rear encapsulant are different. Set #5 minimodule variant seems to undergo a higher power loss over the exposure cycle compared to other sets. Set #1 minimodule variant seems to have the least amount of power loss. Sets #3 and #4 minimodules have similar variation in ${}^{n}P_{mp,IV}$ with exposure time.

Multiple regression analysis was done using netSEM, similar to the procedure outlined in our previous study [9]. The purpose of multiple regression analysis is to identify the causes behind the power loss occurring in degrading minimodule variants. One of the capabilities of multiple regression analysis is service lifetime prediction (SLP) by considering the impact of multiple mechanistic variables and stressors on the power [9].

Two of the degrading minimodule variants, DG with EPE and POE exposed in mDH+FSL, fabricated by Manufacturer A, were chosen from Table 3. Figure 20 and Figure 21 shows the results for both variants. In both the cases, ${}^{n}P_{mp,IV}$ and ${}^{n}C_{s,IV}$ drop in value with time, whereas ${}^{n}I_{sc,IV}$ and ${}^{n}V_{mp,PIV}$ remain nearly constant. ${}^{n}C_{s,IV}$ is the inverse of ${}^{n}R_{s,IV}$ (series resistance). ${}^{n}C_{s,IV}$ is considered so that range of values for ${}^{n}C_{s,IV}$ is comparable to that of other variables. An increase in series resistance negatively impacts solder joints, interconnects, resistance in junction box connections and emitter/base regions of the cell, and/or cell metallization, causing an increase in corrosion [9, 11, 12, 13]. Multiple regression analysis reveals that the dominant degradation mode in these minimodules is corrosion.

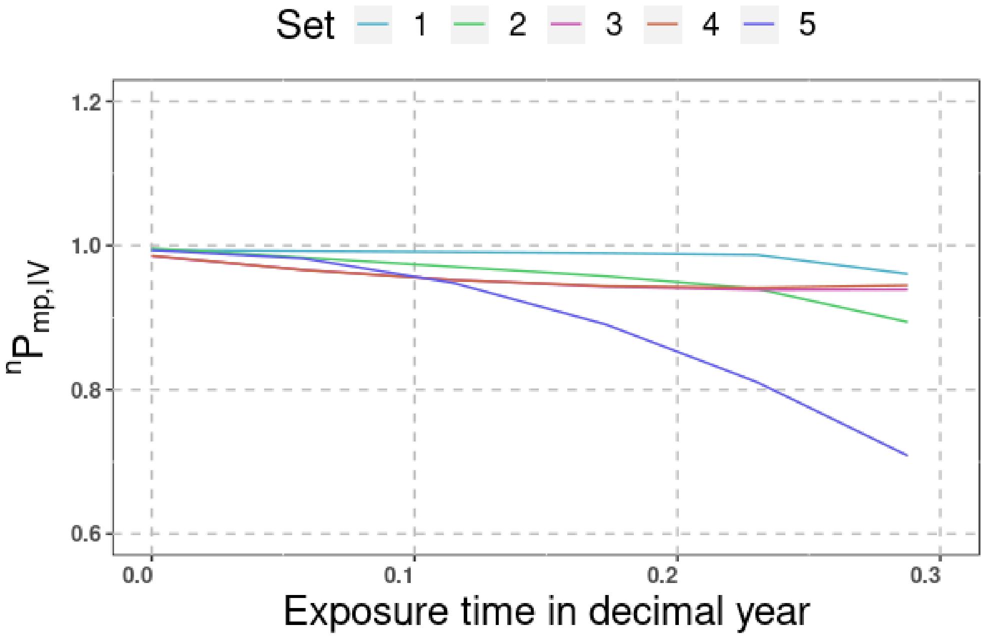

Figure 19: Variation of normalized power ($^nP_{mp,IV}$) with exposure time (dy) ($< S|R >$) for minimodule variant DG with POE in mDH+FSL exposure fabricated by Manufacturer A for all sets. The best model equation line is shown for each set.

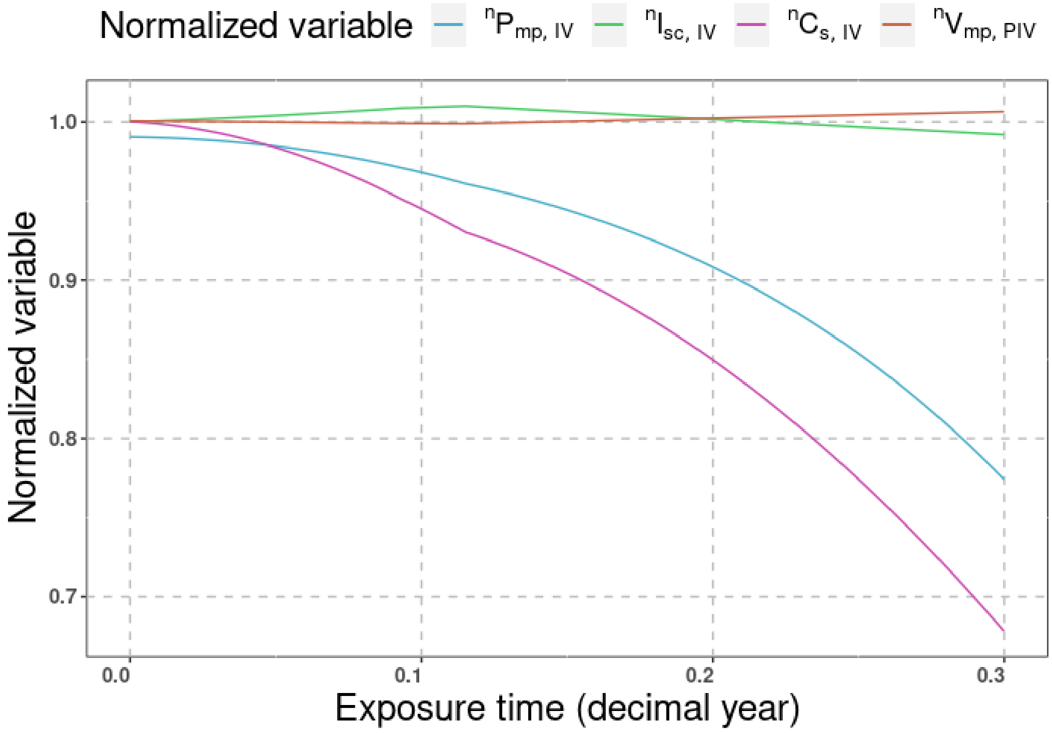

Figure 20: Variation of mechanistic variables ($^nI_{sc,IV}$, $^nR_{s,IV}$, and $^nV_{mp,PIV}$) and power ($^nP_{mp,IV}$) with exposure time (dy) using multiple regression network structural equation modeling for DG with EPE manufactured by A in mDH+FSL (set #5).

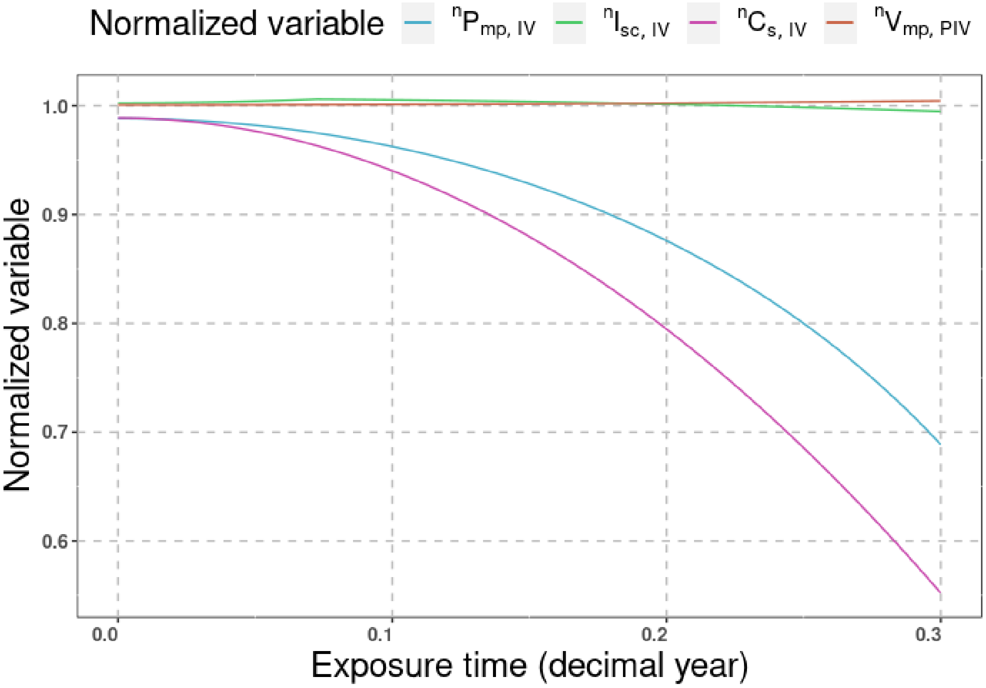

Figure 21: Variation of mechanistic variables (${}^{n}I_{sc,IV}$, ${}^{n}R_{s,IV}$, and ${}^{n}V_{mp,PIV}$) and power (${}^{n}P_{mp,IV}$) with exposure time (dy) using multiple regression network structural equation modeling for DG with POE manufactured by A in mDH+FSL (set #5).

3.4.2 Outdoor exposure results

The minimodule characterization in this project was completed in BP1 and BP2 as part of:

- MS 1.6, 2.3
- ST 2.7, 3.3, 6.1, 6.6, 7.1, 7.5

Thirty-two minimodules from sets #1-#4 were exposed in outdoor conditions (SDLE SunFarm) for 1.6 years. The variants exposed are highlighted in Table 2. I-V features were extracted from each I-V curve using the ddiv package in CRAN [14], including the maximum power (P_{mp}), the current at P_{mp} (I_{mp}), the voltage at P_{mp} (V_{mp}), the short-circuit current (I_{sc}), the open-circuit voltage (V_{oc}), the series resistance (R_s), and the shunting resistance (R_{sh}). The module temperature, POA irradiance, and these I-V features except R_{sh} were processed by the Suns-Voc package[15] to obtain the predicted electrical features at reference conditions for each defined period as one week. These predicted features for modeling in the next step include $P_{mp,IV}$, $I_{sc,IV}$, $R_{s,IV}$, and $V_{mp,PIV}$. PIV is the short name for the Pseudo I-V curve. The reference conditions were 1000 W/m^2 POA irradiance and corresponding median annual module temperature, which was estimated as 45 $^\circ C$ using the data of the first year and a POA irradiance range of 1000 $\pm$ 10 W/m^2. Usually, a seasonal decompose should be applied to remove the seasonality and noise to obtain the trend. However, such methods can not be applied due to the requirement of more than two years of data that can not be met by the available outdoor data in this study.

$< S|R >$ results were obtained for outdoor minimodules exposed in SDLE SunFarm, Cleveland OH. The data collected corresponds to the full module measurements. Normalization was done based on the first 90 days for all the modules except sa43014 (normalized based on 90-120 days) and sa43022 (normalized based on 120 days). These two modules had problems with the connection at the beginning of the exposure.

The variations in outdoor minimodules are based on module architectures (GB/DG), encapsulant materials (EVA/POE), cell types (mono-facial/bi-facial),and rear encapsulant types (transparent, opaque, UV-cutoff).

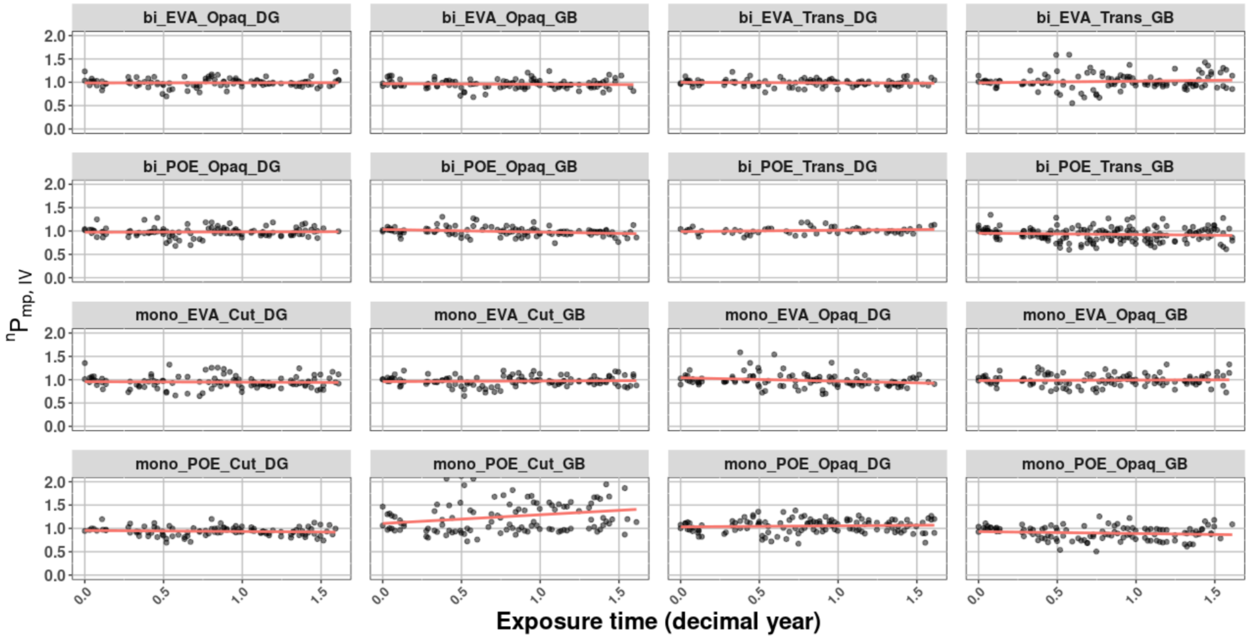

Figure 22: Outdoor minimodule facet plot with dy as the stressor and $^{n}P_{mp,IV}$ as the response. Each facet grid has normalized data points and simple linear model fit.

The slope values from linear models are summarized in Table 4. It can be seen that there are variants with slope values decreasing more than -0.01; such variants are degrading. Some of the variants that are degrading are bi_POE_Opaq_GB, mono_EVA_Opaq_DG and mono_POE_Opaq_GB. The stable variants are the ones that have nearly zero slope; for example, bi_POE_Opaq_DG and bi_EVA_Opaq_DG are considered stable.

Table 4: Slopes from linear fitted models (dy versus $^{n}P_{mp,IV}$).

Variant	Slope
bi_EVA_Opaq_DG	0.003
bi_EVA_Opaq_GB	-0.01
bi_EVA_Trans_DG	-0.01
bi_EVA_Trans_GB	0.03
bi_POE_Opaq_DG	0.006
bi_POE_Opaq_GB	-0.06
bi_POE_Trans_DG	0.03
bi_POE_Trans_GB	-0.03
mono_EVA_Cut_DG	-0.01
mono_EVA_Cut_GB	0.01
mono_EVA_Opaq_DG	-0.07
mono_EVA_Opaq_GB	0.01
mono_POE_Cut_DG	-0.02
mono_POE_Cut_GB	0.2
mono_POE_Opaq_DG	0.02
mono_POE_Opaq_GB	-0.04

$< S|M|R >$ models for 16 variants were obtained. Figure 23 shows an $< S|M|R >$ model for GB with EVA with bi-facial PERC and opaque rear encapsulant.

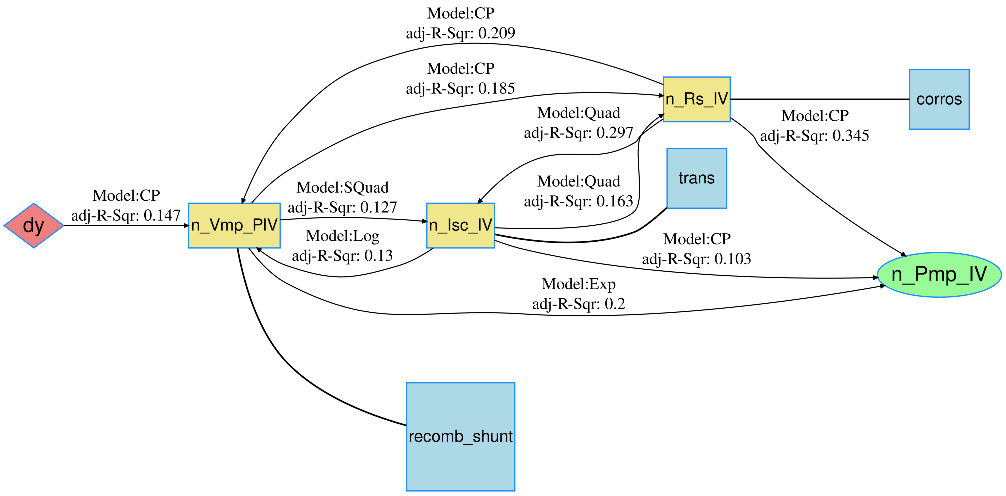

Figure 23: $< S|M|R >$ model of GB with EVA with bifacial PERC and opaque rear encapsulant. Each pathway has a specific best model/functional form and corresponding adjusted R^2 value. The blue boxes represent short-hand description of degradation mode.

The slope values of linear model fits from $< S|M|$ results are summarized in Table 5. It can be seen that for the three degrading module types bi_POE_Opaq_GB, mono_EVA_Opaq_DG () and mono_POE_Opaq_GB, the prominent degradation mode is optical transmission loss (tracked by $^{n}I_{sc,IV}$). $^{n}R_{s,IV}$ and $^{n}V_{mp,PIV}$ do not contribute to degradation as much in these three variants.

Table 5: Slopes from linear fitted models (dy versus mechanistic variables ${}^{n}I_{sc,IV}$, ${}^{n}R_{s,IV}$, ${}^{n}V_{mp,PIV}$).

Variant	Slope of $< S\|M\|$		
	${}^{n}I_{sc,IV}$	${}^{n}R_{s,IV}$	${}^{n}V_{mp,PIV}$
bi_EVA_Opaq_DG	-0.02	0.02	-0.008
bi_EVA_Opaq_GB	-0.002	0.02	-0.003
bi_EVA_Trans_DG	-0.009	0.01	-0.008
bi_EVA_Trans_GB	-0.02	0.08	-0.0003
bi_POE_Opaq_DG	0.02	0.002	0.002
bi_POE_Opaq_GB	-0.03	0.05	-0.004
bi_POE_Trans_DG	0.003	0.02	-0.002
bi_POE_Trans_GB	-0.01	0.01	0.0001
mono_EVA_Cut_DG	-0.03	0.01	0.0008
mono_EVA_Cut_GB	-0.008	0.07	-0.0005
mono_EVA_Opaq_DG	-0.014	0.07	-0.001
mono_EVA_Opaq_GB	-0.008	-0.007	-0.001
mono_POE_Cut_DG	0.003	0.02	-0.0003
mono_POE_Cut_GB	0.006	0.02	0.005
mono_POE_Opaq_DG	-0.02	-0.02	-0.0009
mono_POE_Opaq_GB	-0.01	-0.01	-0.003

3.4.3 Mechanical modeling of cells, packaging materials & mini-modules

The minimodule outdoor exposure in this project was completed in BP1 and BP2 as part of:

- MS 1.3, 2.5
- ST 2.2

The main subtask associated with this topic is ST 2.2: Mechanical modeling of cells, packaging materials & mini-modules.

In this section, an overview of the steps involved in mechanical modeling, bare and soldered cell testing, Weibull analysis, FEM results, proof load calculation and 4-point proof loading results for rectangular GB minimodules will be discussed.

PV modules in real-world exposure conditions develop internal mechanical stresses induced by wind, rain, temperature fluctuations, hail, etc. which can lead to cell cracking and further decrease the power output. The changes in mechanical properties of polymeric packaging materials can influence cell cracking: if the encapsulant becomes harder (stiffer), it would transfer more external load to the solar cells, leading to cell cracking. Conversely, if the encapsulant is relatively soft, the strain would not be transmitted to solar cells and there would be no danger of cell cracking. 4-point proof loading is a technique we use in the project to track changes in the encapsulants under accelerated exposure conditions by the cell fracture probability.

There are several steps followed in mechanical modeling studies. Initially, bare and soldered monofacial and bifacial multicrystalline Si PERC cells were tested in parallel and perpendicular testing directions to see if there is any introduction of a new flaw size distribution. Weibull analysis was performed on these bare and soldered cells to obtain Weibull moduli and characteristic fracture displacements (which scale up with characteristic fracture strains). The cells from the same population were then used in 1-cell minimodules and 4-point proof loading was done to obtain Weibull moduli and characteristic fracture strains (ϵ_0). Then, the next step was to use finite element modeling (FEM) to obtain the conversion factor for translating from 1-cell minimodules to 4-cell minimodules, which is the minimodule we used under mDH+FSL accelerated exposures. Proof loads were calculated such that the probability of fracture is less than 5% in the undegraded state. During the course of indoor accelerated exposure, 4-point proof loading was done on rectangular GB minimodules at the end of each mDH+FSL exposure step using the calculated proof load values. Figure 24 shows a Weibull plot with the sequence of steps in the T50 project.

The figure captures the effect of soldering of bare cells: it would lead to the introduction of a new flaw size distribution that would change the slope and flexural displacement. The results from FEM analysis are necessary to be able to calculate the proof load (proof load is the load at which there is negligible failure in undegraded minimodules and a high probability of failure in degraded minimodules). Using the proof load, the changes in packaging materials of minimodules can be tracked at the end of each exposure step. Once the cells are packaged, they are capable of detecting changes in the polymer layers of the minimodules if the encapsulant become harder enough.

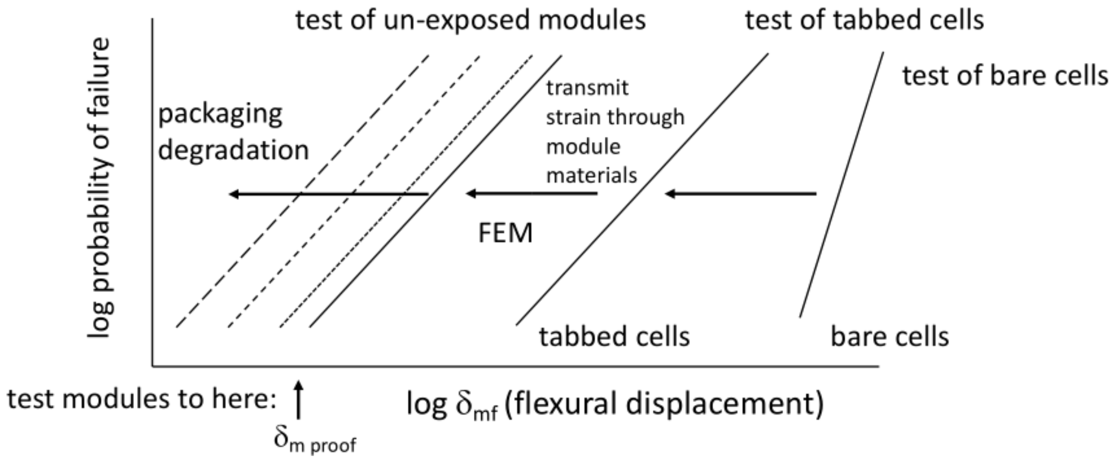

Figure 24: Weibull plot showing the steps in the T50 project.

Weibull analysis was done for both bare and soldered monofacial and bifacial PERC cells in different testing directions (i.e. parallel and perpendicular). The Weibull modulus (b) characterizes the variation in material strength and distribution. For example, a higher Weibull modulus indicates a tighter and narrower distribution.

From Table 6, it can be seen that the Weibull modulus values decrease for soldered bifacial cells in both the testing orientations which indicate a greater distribution in measurements but the fracture displacement doesn't change. This shows that there is an introduction of strength-limiting flaw size distribution due to the soldering process and hence they are the most influenced by soldering. Also, note that the X-axis is fracture displacement which scales up with fracture strain and can be obtained from classical beam theory for 4-point bending. For monofacial multi-Si cells, the flaw size distribution increases in the parallel direction after soldering.

Table 6: Weibull modulus and characteristic fracture displacement values for monofacial and bifacial PERC cells (bare and soldered).

Type	Weibull Modulus (b)	Characteristic Fracture Displacement (mm)
Monofacial PERC, bare, parallel	12	12.3
Monofacial PERC, bare, perpendicular	12	11.6
Monofacial PERC, soldered, parallel	7.5	12.3
Monofacial PERC, soldered, perpendicular	11	11.5
Bifacial PERC, bare, parallel	13	14.7
Bifacial PERC, bare, perpendicular	9.6	11.7
Bifacial PERC, soldered, parallel	7.7	15.0
Bifacial PERC, soldered, perpendicular	6.4	11.3

Weibull analysis was done on 120 40 x 19 cm Glass/Backsheet (GB) 1-cell minimodules after 4-point bending flexure. Two cell types were used: monofacial and bifacial. The encapsulants used in fabricating these minimodules were transparent and UV-cutoff EVA and POE. The backsheet used was KPf. Table 7 summarizes these the Weibull moduli and characteristic fracture strains (ϵ_0).

Table 7: Weibull modulus and characteristic fracture strain values for 1-cell minimodules with EVA and POE encapsulation.

Type	Weibull Modulus (b)	Characteristic Fracture Strain (ϵ_0)
Bifacial PERC, EVA, parallel	9.8	6.2E-4
Bifacial PERC, EVA, perpendicular	13	4.9E-4
Monofacial PERC, EVA, parallel	6.8	6.3E-4
Monofacial PERC, EVA, perpendicular	20.7	5.8E-4
Bifacial PERC, POE, parallel	11.3	6.9E-4
Bifacial PERC, POE, perpendicular	13.4	5.0E-4
Monofacial PERC, POE, parallel	10.2	7.3E-4
Monofacial PERC, POE, perpendicular	17.4	5.7E-4

It can be seen that in the parallel (||) direction, the characteristic fracture strains (ϵ_0) are similar across all cell types and encapsulants in the minimodules. For each encapsulant type, the 1-cell minimodules with bifacial cells have a lower characteristic fracture strain value in the perpendicular orientation compared to ||, which makes them more sensitive to loading. In addition, there's not much of a difference between EVA and POE samples as they lie in a similar range of ϵ_0 values. This is due to the fact that the encapsulants have similar stiffness at room temperature and the loading rate are similar. Even after grouping minimodules having EVA and POE encapsulation together and separating only on the basis of cell type and orientation as shown in Figure 25, bifacial minimodules in the perpendicular orientation have lower fracture strain and an overall lower fracture strength. They appear to be more sensitive in the perpendicular direction.

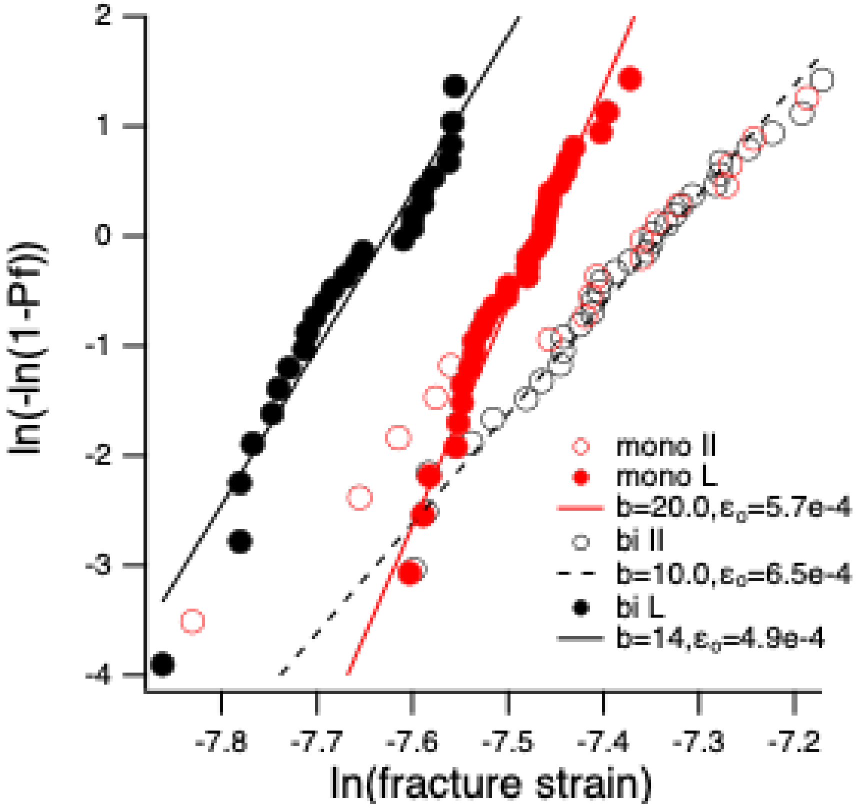

Figure 25: Weibull plots for 1-cell minimodules after grouping encapsulants and separating on the basis of cell and orientation.

A short experiment was done using a 1-cell minimodule to detect cell cracking events using load versus displacement data. It was observed that if there is a cell cracking event, there would be a sharp drop in the load, which can be easily identifiable in a load versus displacement plot. Figure 26 shows this result. This result is useful in identifying cell cracking due to proof loading.

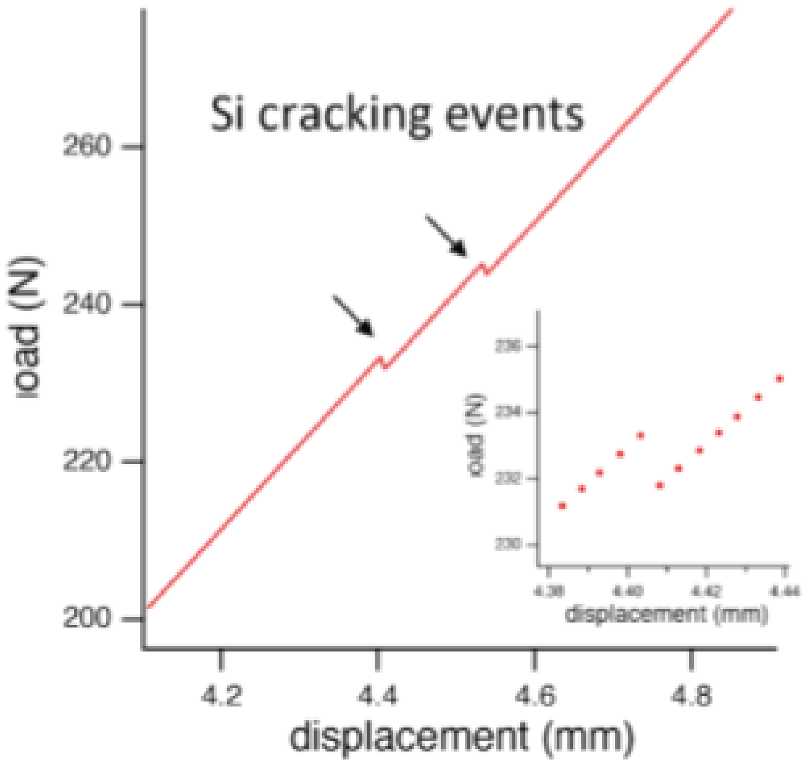

Figure 26: Cell cracking events in a 1-cell minimodule as observed on load versus displacement plots.

Finite element analysis is useful to translate the proof load from 1-cell minimodules to 4-cell minimodules. This is done using a conversion factor specific to each type of minimodule.

Figure 27 shows the finite element analysis for 1-cell and 4-cell minimodules. It was observed that for bare cell 4-point bending, the tensile strain is constant between inner spans whereas for the minimodule 4-point bending, the tensile strain is maximum only at the center of the cell. The values of the conversion factors (designated as m) is shown in the next section for each case.

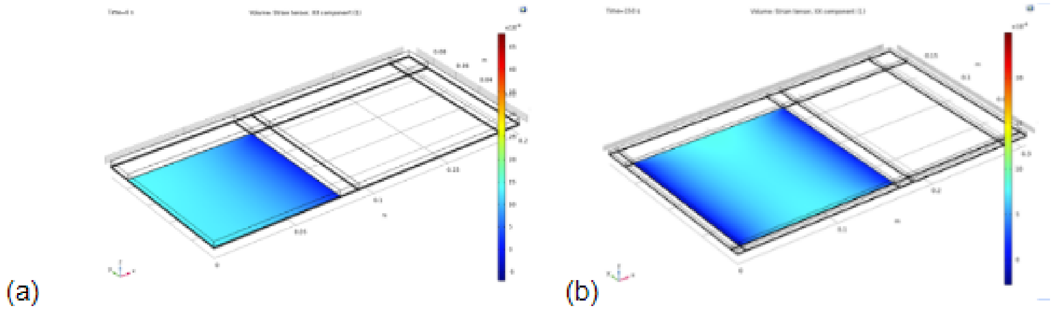

Figure 27: FEM results for (a) quarter of a 1-cell minimodule and (b) A quarter of 4-cell minimodule.

The part of the work is taken from the published article named 'Employing Weibull Analysis and Weakest Link Theory to Resolve Crystalline Silicon PV Cell Strength Between Bare Cells and

Reduced- and Full-Sized Modules' [16]. In this work, Weibull analysis and weakest link theory are employed to resolve the probability of crystalline silicon PV cell fracture when measured as bare cells and when stressed in reduced 1-cell PV minimodules and full-sized 4-cell PV minimodules. The ability to measure the strength distribution of bare cells and accurately predict their probability of fracture once packaged into a module is demonstrated in this work. Some of the results from the article are highlighted in this section.

A single population of bare multicrystalline silicon bifacial PERC PV cells (156.75 × 156.75 × 0.17 mm) were evaluated in this study. All cells were tabbed (application of soldered ribbon interconnects) on the production line of a Tier 1 PV manufacturer, and a subset of these bare cells was packaged into 20 × 40 cm one-cell modules of a glass/polymer backsheet construction. Four-point flexure (4PF) testing was performed to evaluate the strength distribution of the bare cells and once packaged into the one-cell modules. Cell-level testing was conducted with a loading (140 mm) to support span ratio of about 0.5 and at a load-line displacement rate of 200 μms^{-1} until cell fracture. All cells were evaluated such that the rear (nonsun-facing) side of the cell was put into tension and in both a parallel (flexural strain direction parallel with tabbing direction) and perpendicular orientation. One-cell module-level 4PF testing with cells both in the parallel and perpendicular orientations was similarly conducted with a loading to support span ratio of 0.5, where the packaged cell was totally contained within the inner loading span, and a load-line displacement rate of 20 μms^{-1} until cell fracture was detected by live electroluminescence imaging (no cell cracks were detected prior to loading).

Figure 28 shows the results of similar numerical simulations to calculate the Weibull effective volume, area, and edge area of the cell when both loaded in 4PF as a bare cell and packaged within the experimental one-cell module are presented as the computed characteristic strength ratio as a function of Weibull modulus. Volume and areas calculated in this study are utilized to address the potential for the strength limiting flaw distribution to reside in one of these locations. The shaded region of Figure 28 highlights the experimentally measured space of packaged to bare cell characteristic stress ratio ($\sigma_m/\sigma_c =$ 0.8–0.85) and Weibull modulus ($m =$ 16–20). The intersection of this experimentally measured space with the characteristic strength ratios predicted by both the Weibull effective volume and edge area suggests the population of strength limiting flaws resides in one of these locations. Considering the very high quality of the silicon feed stock used to produce PV cells, and the relatively abrasive nature of the subsequent sectioning and processing steps, we conclude that the strength limiting flaws are most likely to reside on the edge area of these cells.

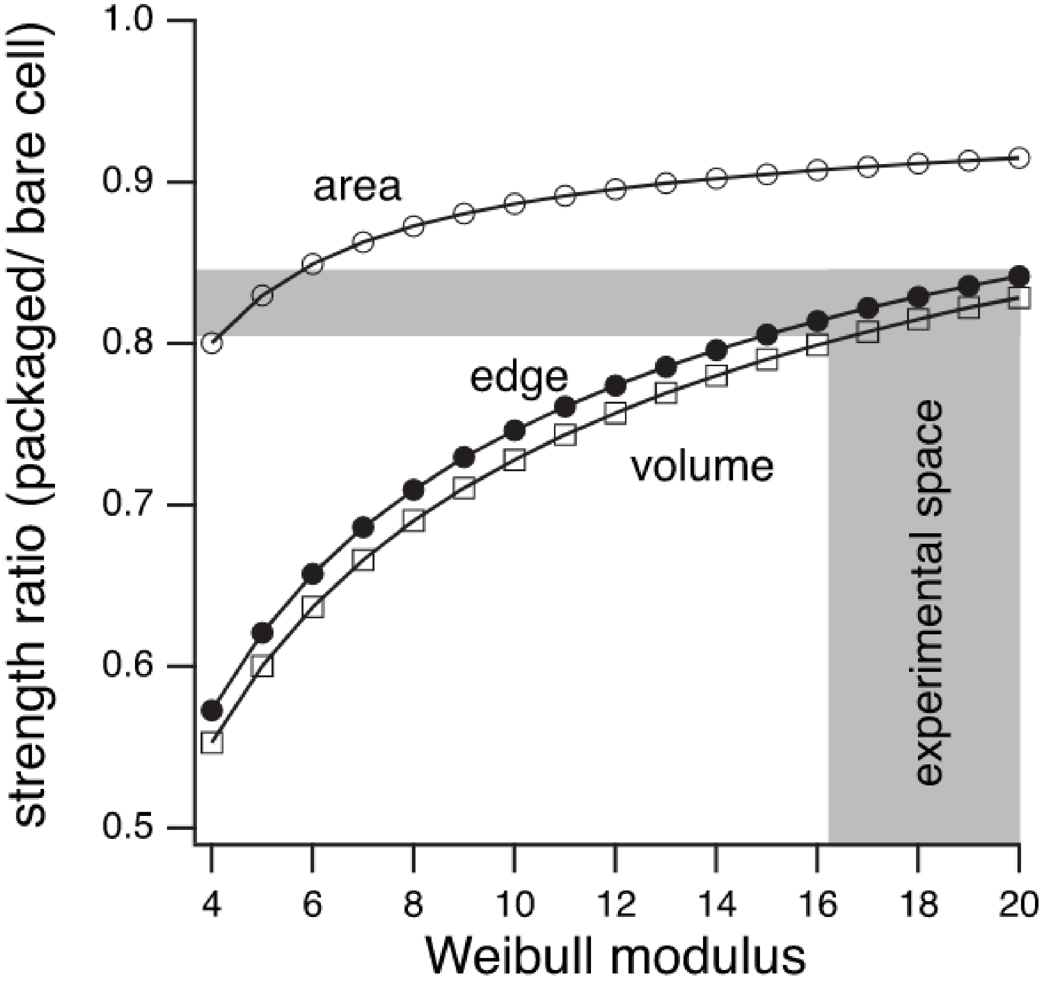

Figure 28: Packaged to bare cell characteristic strength ratios according to Weibull effective area, edge area, and volume calculations for the experimental one-cell modules. The shaded region represents the experimentally measured space.

Figure 29 reveals the characteristic strength ratios between the simulated fourcell modules loaded uniformly and in 4PF, and the bare cell loaded in 4PF. The ratios are close to unity for the four-cell module loaded in 4PF, implying that the characteristic fracture strength of the cell will be similar when measured as a bare or packaged cell in 4PF. When the four-cell module is loaded uniformly, however, about 20% reduction in characteristic strength is expected between the packaged and bare cell. A similar comparison between the uniformly loaded full-sized module and bare cell loaded in 4PF is presented in Figure 30. In Figure 30, the results from only the center-most row of cells are presented as these cells experience the highest absolute stress with loading. This analysis demonstrates that for cell strength distributions with Weibull moduli greater than 10, the characteristic strength is reduced by 10%–20% once the cells are packaged into a full-sized module and uniformly loaded.

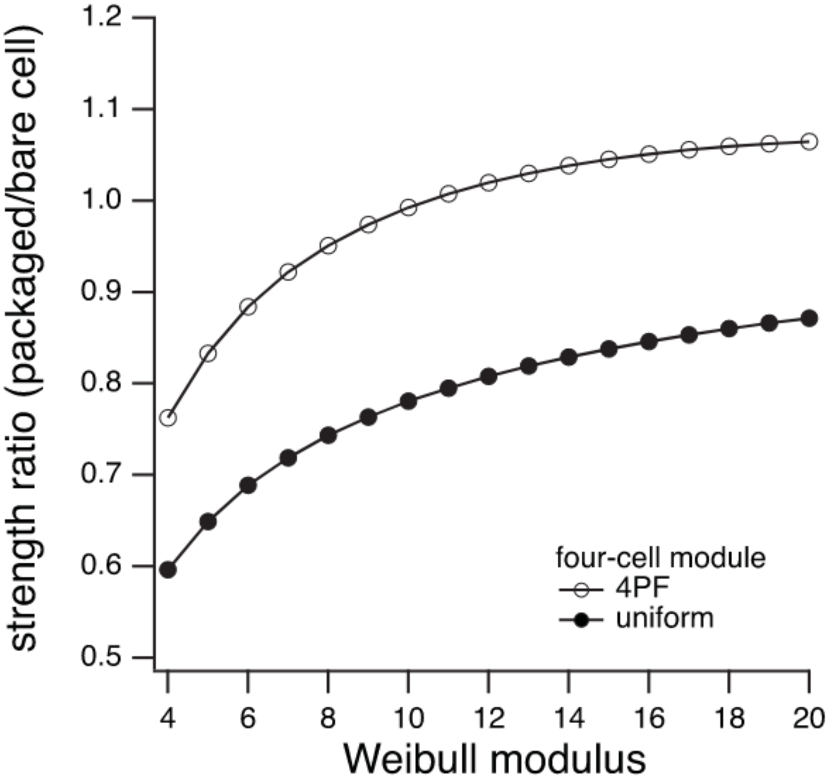

Figure 29: Characteristic strength ratios based on effective edge area between the simulated packaged cells within four-cell modules loaded uniformly and in 4PF, and the bare cell loaded in 4PF.

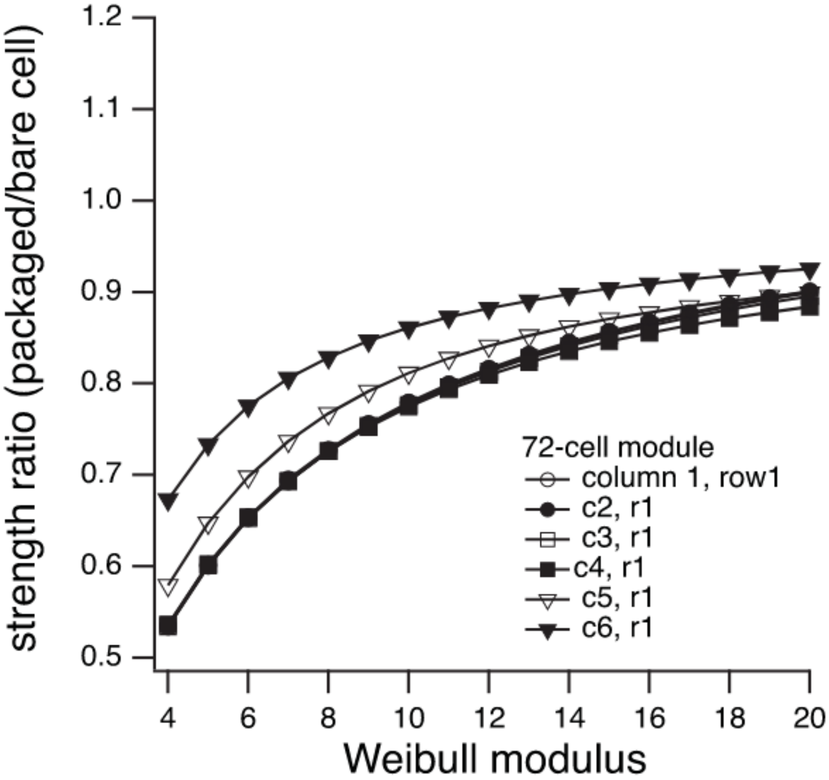

Figure 30: Characteristic strength ratios based on effective edge area between the center row of packaged cells in the simulated uniformly loaded 72-cell module and a bare cell loaded in 4PF.

The main takeaway from this study is that the characteristic cell strength is reduced by about 20% once packaged into the laminate of a one-cell module and loaded in 4PF. This experimental observation was shown consistent with a weakest link theory prediction that the strength limiting flaws reside on the surface of the cell's edge.

For the calculation of proof loads for different minimodule combinations, Eq. 1 was used, where P_f is the probability of failure, λ is the discount term, $m\epsilon_0$ is the characteristic failure load (where m is the conversion factor from 1-cell to 4-cell minimodule and ϵ_0 is the characteristic fracture strain). λ is the discount term that changes the distribution function in such a way that an undegraded sample has a negligible probability of failure and a large probability of fracturing a degraded sample. For example, an λ value of 0.7 means there's 30% degradation in the sample; essentially, λ captures the effect of degradation in the sample. The values of b, ϵ_0 are obtained from 1-cell minimodule Weibull plots.

$$P_f = 1 - exp(-(\frac{load}{\lambda.m\epsilon_0})^b \tag{1}$$

The proof load was calculated by using 5% fracture probability and $\lambda = 1$. The proof loads for all GB minimodules are listed in Table 8. Here, $||$ means parallel layout and $\perp$ means perpendicular layout.

Table 8: Proof load values calculated for each minimodule set.

Set	Layout	Proof Load (N)
1	$\|\|$	439.9
1	$\perp$	447.3
1	$\|\|$ (wrong front glass thickness (2.5 mm))	209.4
1	$\perp$ (wrong front glass thickness (2.5 mm))	205.9
2	$\|\|$	439.9
2	$\perp$	360.9
3	$\|\|$	439.9
3	$\perp$	447.3
4	$\|\|$	439.9
4	$\perp$	360.9
5	$\|\|$	439.9
5	$\perp$	360.9

3.4.4 Four-Point Proof Loading Results for GB Minimodules

Four-point proof loading was done on 4-cell rectangular GB minimodules at end of each exposure step. Using the proof loads listed in Table 8, the load and displacement data was collected for minimodules. EL images were collected before, during and after loading as shown in Figure **??**.

Offset load versus load line displacement plots were generated to monitor changes in minimodules. Offset load is defined as load at which the load line displacement is zero before it turns nonzero subtracted from load. By defining offset load, we ensure that all the line plots start from a common zero. Load line displacement is the displacement subtracted from the first displacement value in the data frame. This is done to set the displacement range from 0-5 mm. These definitions have been adopted with Si cracking event as a reference (refer to Figure 26).

In this section, the results from sets #1-#4 will be shown. Due to some issues in data syncing in our high performance computing cluster, set #5 data did not get synced properly. The complete set of results will be included in our future publication.

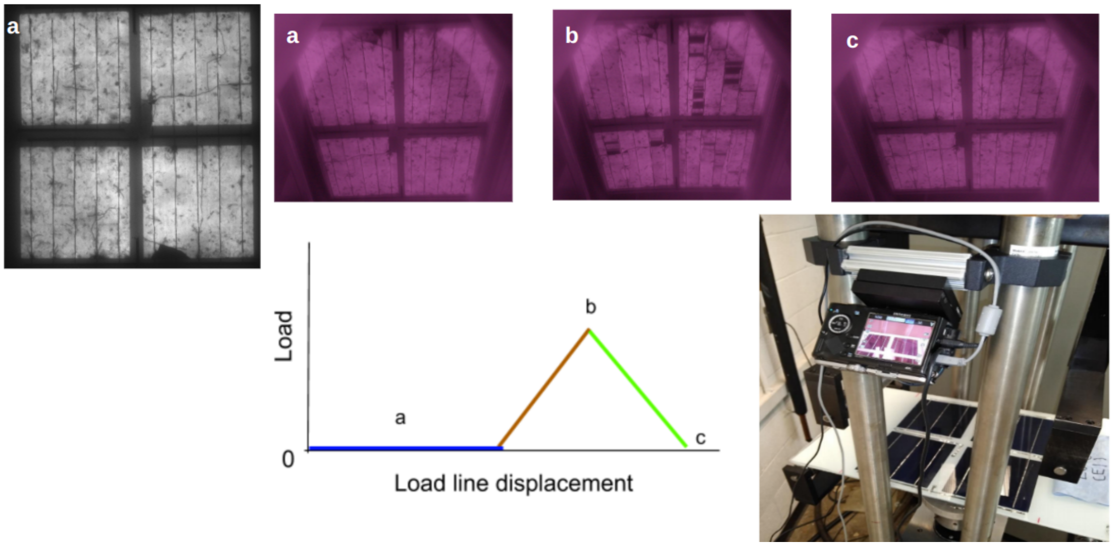

Figure 31: EL instrument setup with images shown before, during and after proof loading. The grayscale image represents the EL image taken using EL/PL system.

The offset load versus load line displacement plots are shown in Figs. 32, 33, 34 and 35. Note that in Figure 32, 3 of the minimodules had incorrect front glass thickness (2.5 mm glass instead of 3.2 mm glass), which increased the compliance of the overall minimodule. From sets #1-#4 results, we observed that cell cracking was not induced due to the 4-point proof loading experiment. In other words, minimodule cells that did not have cracks before the experiment did not develop cracks during the loading. In the presence of pre-existing cracks before the experiment, the cracks open up to reveal electrically isolated regions in the cells as shown in Figure 31 (image (b)). There is no strong dependence in the encapsulant type or orientation in these results.

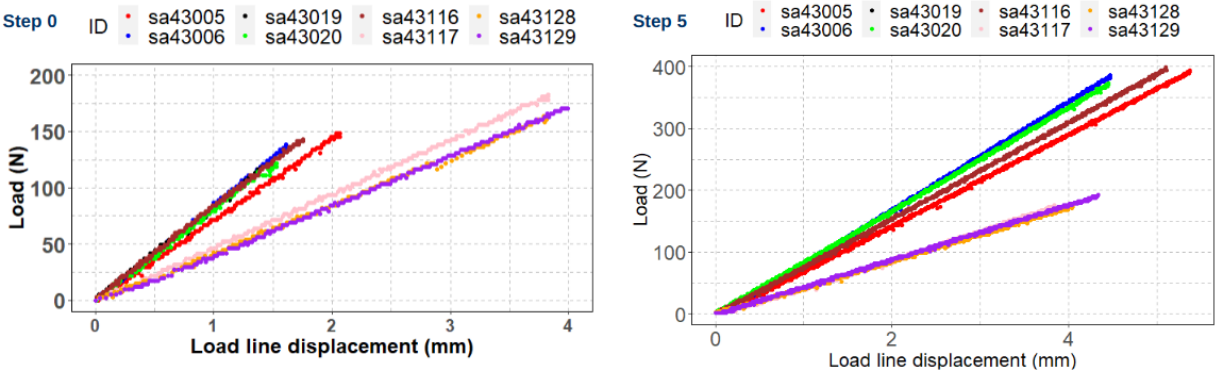

Figure 32: Offset load versus load line displacement plots for minimodules in set #1. Baseline and exposure step 5 results are shown.

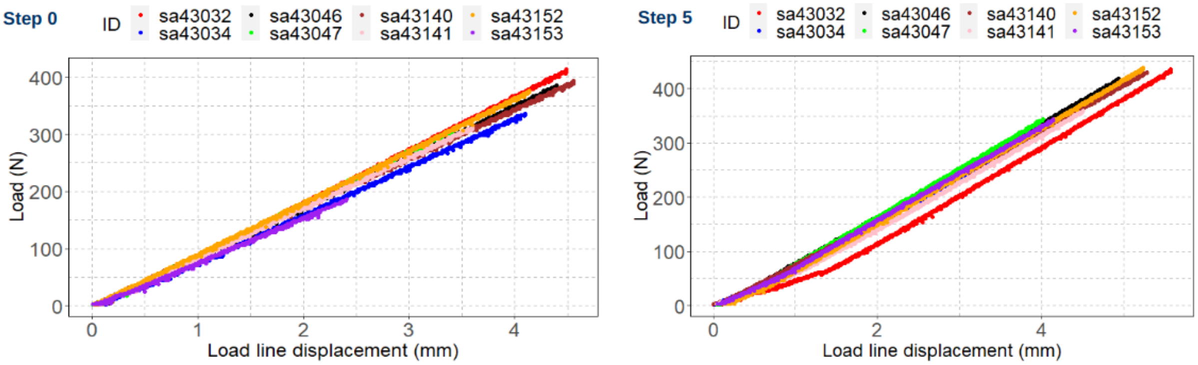

Figure 33: Offset load versus load line displacement for minimodules in set #2. Baseline and exposure step 5 results are shown.

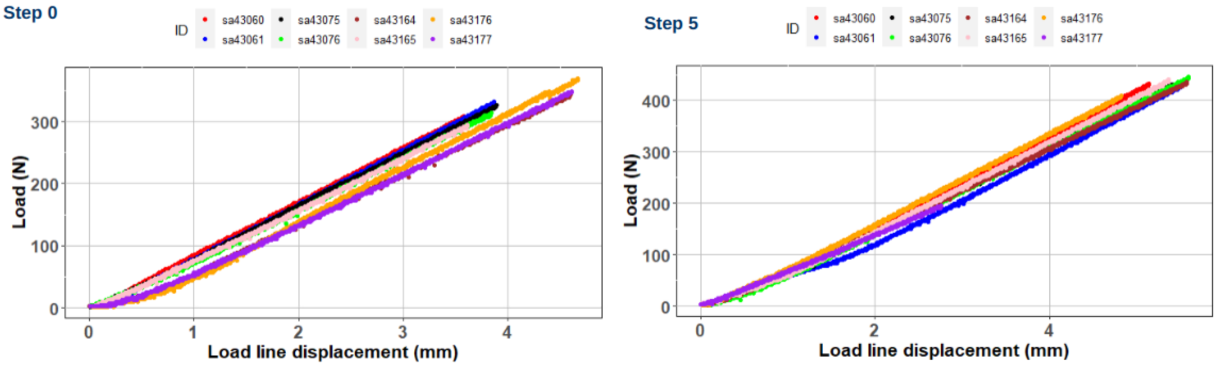

Figure 34: Offset load versus load line displacement for minimodules in set #3. Baseline and exposure step 5 results are shown.

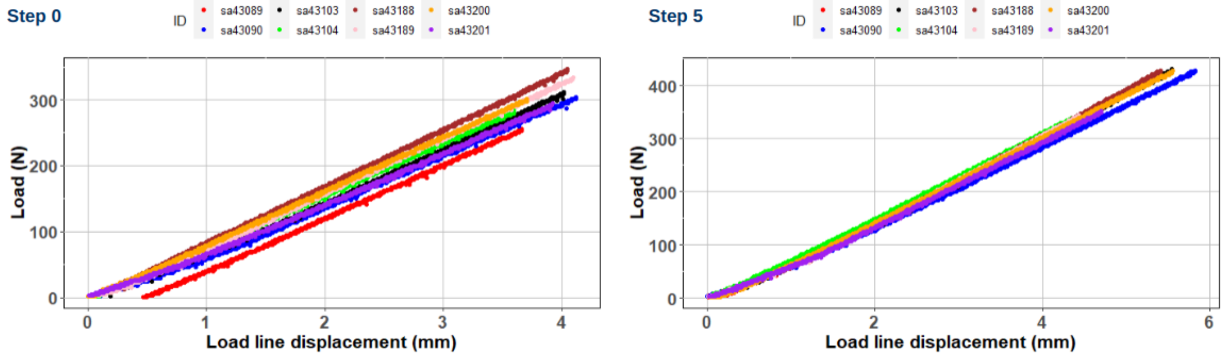

Figure 35: Offset load versus load line displacement for minimodules in set #4. Baseline and exposure step 5 results are shown.

3.4.5 Characterization of rear encapsulants from set #5 minimodules

This topic does not correspond to any particular task, subtask or milestone. However, this will be part of our future publication.

For materials characterization, the rear encapsulants were extracted from GB minimodules after step 6 of exposure (i.e., 3024 hours of exposure). Fourier-transform infrared (FTIR) spectroscopy was performed on EPE and POE rear encapsulants from unexposed and exposed minimodules. An FTIR spectrometer (Spectrum One, Perkin Elmer) was used to record IR spectra using 16 scans at a resolution of 1 cm^{-1} with attenuated total reflectance (ATR). The encapsulant changes were monitored in the range of 650-4000 nm using Spectrum One software. Measurements were taken for each retrieved encapsulant to identify changes at the encapsulant-cell interface (cell-side).

Colorimetry was used for obtaining yellowness index (YI) values to monitor changes in the encapsulants. YI changes in POE and EPE rear encapsulants from unexposed and exposed minimodules were investigated. A HunterLab UltraScan PRO instrument was used along with the Easy Match QC software to organize the results.

In this section, we compare changes in the UV-cutoff POE and EPE rear encapsulants across exposed and unexposed minimodules. We selected two GB minimodules, with either EPE or POE, exposed in mDH conditions for 3024 hours. Similarly, we selected two unexposed GB counterparts to compare if there were any chemical changes in the rear encapsulants. To understand the peaks in EPE, unexposed minimodule with EVA encapsulation was used; the rear encapsulant was UV-cutoff EVA.

This analysis helps us assess the extent of degradation and chemical modifications in the encapsulant materials due to exposure. We were particularly interested in identifying any unique peaks present in the spectra of the exposed EPE samples compared to the unexposed POE and EVA. Figure 36 shows the baseline FTIR-ATR spectra for cell-side EPE, POE, and EVA rear encapsulants. It can be seen that the unexposed and exposed spectra for each encapsulant are quite similar. From 650 to 2000 cm^{-1}, EPE behaves similarly to EVA. From 2000 to 3000 cm^{-1}, EPE behaves similarly to both POE and EPE. However, past 3000 cm^{-1}, we observe the appearance of a small peak in the EPE encapsulant spectra, which looks similar to the water absorption band [17]. This indicates a potential onset of delamination due to water ingress and/or additive diffusion [18] as the lamination recipe used to manufacture modules in set #5 is not optimized.

In addition, yellowness index (YI) values were obtained for the rear encapsulants to monitor optical transmission changes. Table 9 shows the YI values for the EPE and POE rear encapsulants.

There is an increase in YI from unexposed to exposed encapsulant samples. The largest YI increase can be seen for the POE rear encapsulant: the increase is comparable for both cell- and rear-sides.

3.4.6 Neural Network Models for Predicting Overall Parameters' Change

This particular topic is not related to any specific task, subtask or milestone. This is part of the work done by Jiqi Liu for her PhD thesis.

This work utilizes convolutional neural network (CNN) and recurrent neural network (RNN)

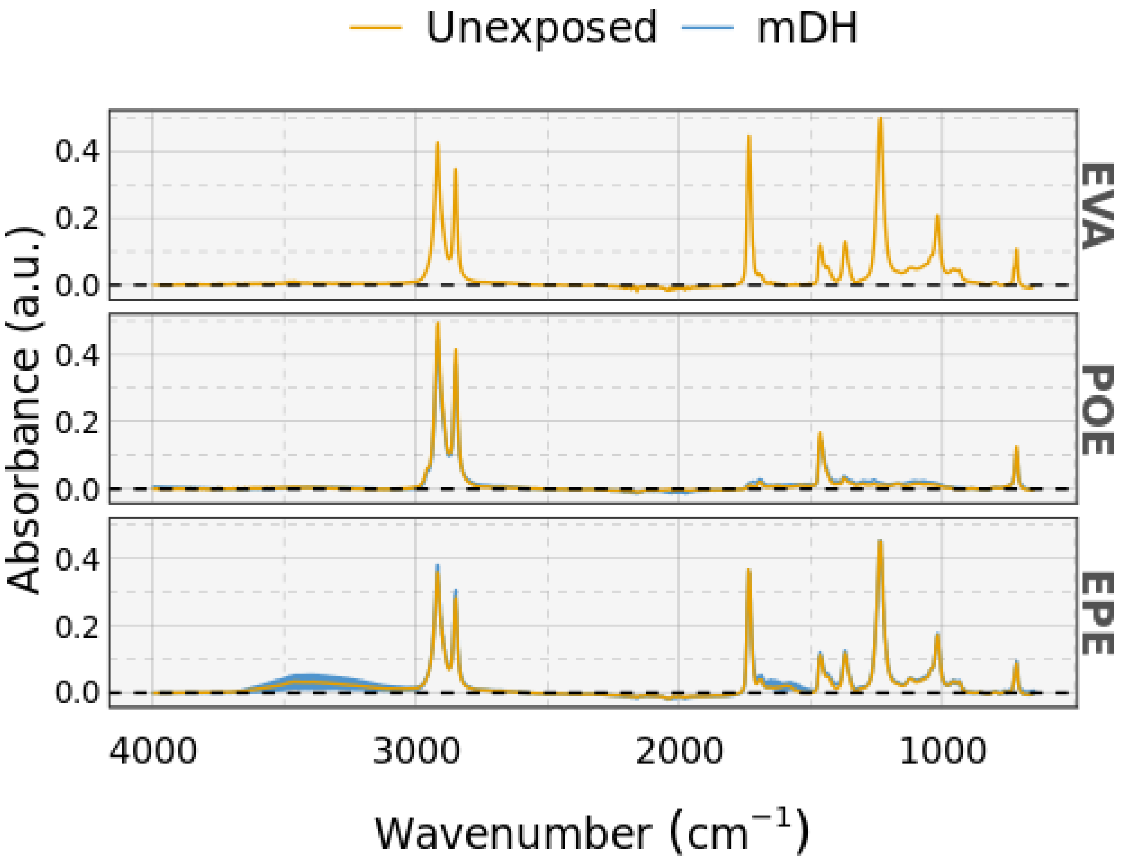

Figure 36: Fourier transform infrared spectra of rear encapsulants (EPE and POE) taken on the cell-side. The EVA spectrum is for an unexposed retrieved sample.

Table 9: Yellowness index values for retrieved encapsulants from unexposed and exposed minimodules.

Encapsulant	Side	Exposure	YI
POE	Cell-side	Unexposed	2.48
POE	Cell-side	mDH	5.34
POE	Rear-side	Unexposed	3.97
POE	Rear-side	mDH	6.77
EPE	Cell-side	Unexposed	5.35
EPE	Cell-side	mDH	5.45
EPE	Rear-side	Unexposed	3.84
EPE	Rear-side	mDH	4.93

to quantitatively learn spatial and temporal information from spatiotemporal image datasets. As a showcase, we use image data of PV modules to train neural network models and predict the change of electrical features, which is enabled by the extensive data collected in the project, including I-V measurements and EL images of many cells in the laminated module.

We demonstrate how to quickly obtain the best local neural network model by running Slurm jobs in our high performance computing cluster to parallelly train 52 model variants with different input image types and image preprocessing methods, and output feature scaling methods. We find a significant performance improvement of RNN over CNN, indicating that it is beneficial to take advantage of measurements for the same sample taken at different exposure times to make a more accurate prediction from the local dataset collected in this project.

The data were obtained from set #1 - #4 minimodules under the two indoor accelerated exposures as mDH and mDH+FSL, with step-wise measurements of six steps, including the baseline step.

PV images: Electroluminescence (EL) and Photoluminescence (PL) images The model inputs contains eight images were collected per module, consisting of three electroluminescence (EL) images with three different forwarding currents, three corresponding dark images with the same camera settings and no forwarding current, and two PL images. The three forwarding currents were 9.4 A (I_o), 4.7 A (0.5 I_o), and 2.4 A (0.25 I_o). The camera exposure time was adjusted for each EL image to reasonably utilize the range of allowed image intensity. One PL image denoted as $PL@OC$ was measured under illumination with the module's current set as zero, i.e., open-circuit status. Another PL image denoted as $PL@SC$ was measured under illumination with the module's voltage set as zero, i.e., short-circuit status. One more PL image denoted as $PL@OC-SC$ was obtained by subtracting $PL@SC$ from $PL@OC$. The illumination was about twice as intense as the green light peak in the solar spectrum, provided by ten green LED lamps arranged in two columns in the imaging chamber.

I-V Features: ${}^{n}P_{mp,IV}$ and ${}^{n}R_{s,IV}$ The output is the normalized maximum power (${}^{n}P_{mp,IV}$) and the normalized series resistance (${}^{n}R_{s,IV}$). These features were obtained from the I-V measurement. Each I-V measurement contains three I-V curves at different irradiance levels, including 1000 W/m^2, 500 W/m^2, and 250 W/m^2. The $P_{mp,IV}$ was extracted from the 1000 W/m^2 I-V curve using the ddiv package on CRAN[14], and the $R_{s,IV}$ was obtained using the three irradiance I-V curves followed the IEC 60891. The normalization was implemented by dividing the value obtained from the same cell at baseline.

Different model variants in categories of CNN, RNN, and CNN+RNN were developed to predict the normalized power and series resistance using PV images as the input. The influences of input image types and preprocessing, output feature scaling, and model categories on the modeling performance are investigated.

Model Input Image Types and Preprocessing We used a cell extraction python pipeline[19] to extract four cell images from each module image. Cell images were used directly as the input, meanwhile other types of images were constructed to investigate potential model performance improvements, such as the baseline subtraction images, the enhanced signal-to-noise (S/N) EL images, and some hyper images.

- **Raw image**: EL image after subtracting the corresponding dark image. Raw EL images with different forwarding current are denoted as $EL@I_o$, $EL@0.5I_o$, and $EL@0.25I_o$.
- **Baseline subtraction image**: EL image after subtracting from EL of the same sample at baseline (initial state without aging). Then the difference was normalized by dividing the average intensity of the baseline image. Therefore, the baseline subtraction image highlights a cell area that becomes darker after some time under an accelerated exposure.
- **Enhanced S/N image**: weighted average of the three EL images measured with different forwarding currents. The weights are the reciprocal of their corresponding camera exposure times. Figure 37 shows the extracted $EL@I_o$ cell image of one solar cell after five steps of mDH exposure, the corresponding baseline subtraction image, and the enhanced S/N EL image.
- **Hyper image**: Constructed image by putting different types of EL and PL images into multiple channels. Double-channel hyper images using the combination of $EL@I_o$ and $EL@0.25I_o$, and $EL@I_o$ and $PL@OC$ after the baseline subtraction were constructed in the study.

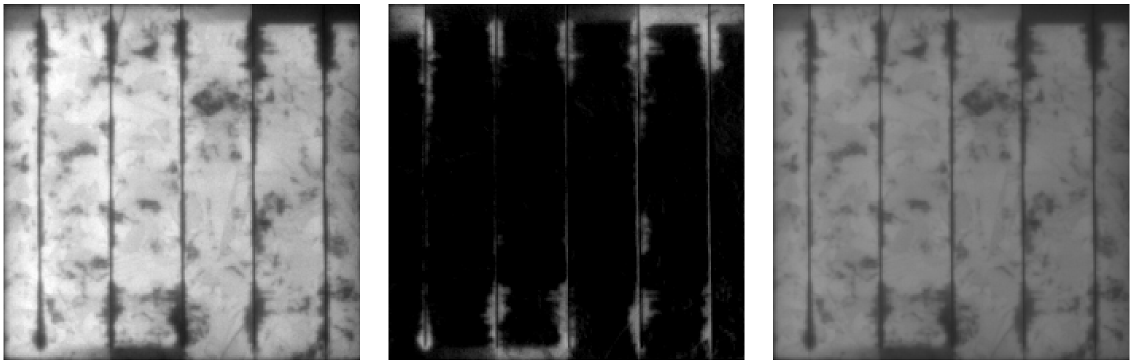

(a) Raw (b) Baseline subtraction (c) Enhanced S/N EL

Figure 37: The raw $EL@I_o$ image (a), the baseline subtraction image (b), and the enhanced S/N EL image (c), for a solar cell in a laminated module after five steps of mDH exposure.

Convolution Neural Network (CNN) CNN is designed to automatically and adaptively learn spatial hierarchies of features through backpropagation by using multiple building blocks, such as convolution layers, pooling layers, and dense layers. In this study, multiple modifications were applied to CNN models to explore potential model performance improvements, including adding dropout layers, changing the number of neurons in dense layers, alternating the grid size in max pooling layers, adding different regularization and batch normalization, and changing convolution structures. The simplest and the most complex CNN models in this study contain two and seven convolution layers shown in Figure 38. For CNN model expressions, the letter "c" stands for the convolution layer, and the letter "p" stands for the max pooling layer with the following number as the layer order.

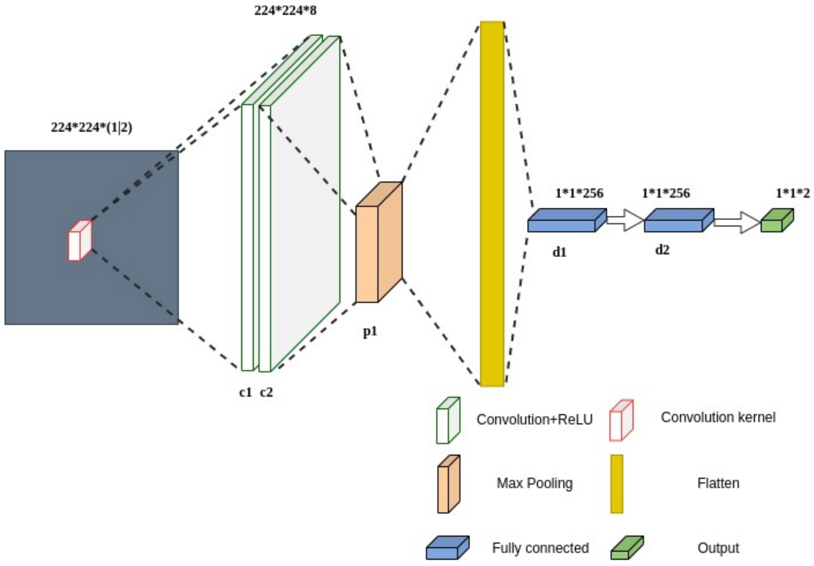

(a) c1c2p1

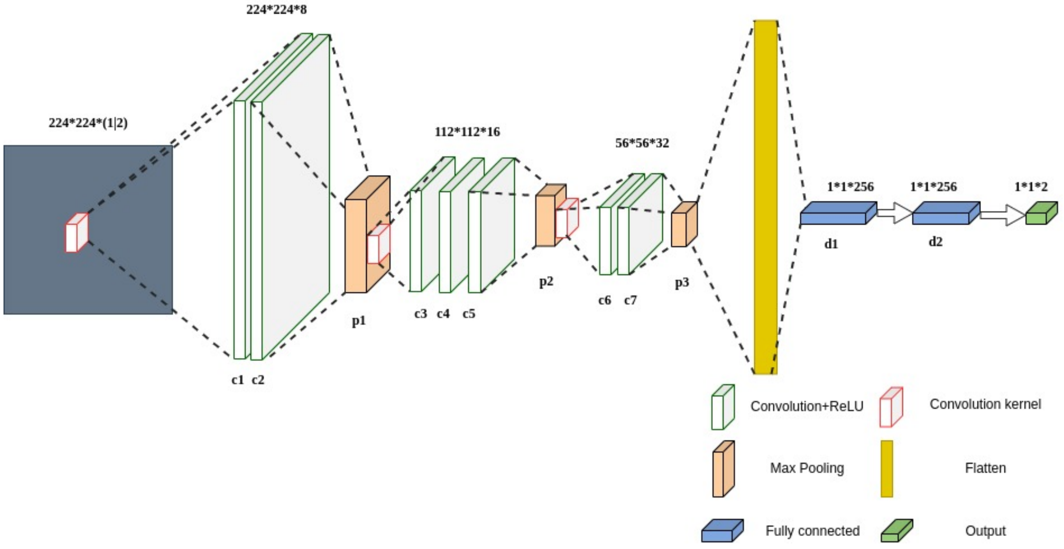

(b) c1c2p1c3c4p2c6c7p3

Figure 38: The model architecture for the simplest and most complex CNN models.

Recurrent Neural Networks (RNN) RNN is a class of artificial neural networks (ANNs) where connections between neurons form a directed or indirect graph along the sequence of input. A sequence is a particular order in which one thing follows another. The most common sequential input is timeseries data such as audio, video, and the daily stock price. A usual RNN neuron takes the current input like a typical feedforward neural network and information from the previous input to predict the current output. So it exhibits temporal dynamic behavior and owns a memory. It is well known that a very deep feedforward neuron network suffers from the vanishing gradient problem. A usual RNN neuron will easily encounter the same issue, which causes its internal state to keep a short-term memory since its depth is decided by the length of the input sequence, which can be long in nature.

Besides dividing a long input sequence into multiple short input sequences, two specially designed RNN neurons are applied more often to enable long-term memory. They are long short-term memory unit (LSTM)[20] and gated recurrent unit (GRU)[21] which can balance the contribution to predicting the current output from the long-term memory, the short-term memory, and the current input.

GRU is used here due to its concise structure and fewer parameters. The number of parameters in a GRU neuron is decided by the input dimension and the specified output dimension, defined in the "units" parameter in the "tf.keras.layers.GRU" function. Performance of RNN models was investigated with units changed as 2, 20, and 200 for a single GRU layer and numbers of GRU layers chosen from 1 to 3. The image dataset needs to be reorganized into a video format to train an RNN model. The video is for each solar cell with frames of images following the order of exposure steps.

CNN+RNN The combined model takes all layers in CNN#1 described in Table **??** except the output layer, followed by the RNN#1 model structure described in Table **??** without the input layer.

Model Output Feature Scaler The normalized Pmp (${}^{n}P_{mp,IV}$) and Rs (${}^{n}R_{s,IV}$) were chosen as the predicted output feature. The normalization was done by dividing the feature value by the value measured from the same cell at baseline. Two kinds of scaling methods were applied for the output for the potential improvement in model performance, including the minimum-maximum scaler (MMS) shown in Eq. 2 and the standard scaler STS) shown in Eq. 3. The scaler translates each feature individually, denoted as X in Eq. 2 and Eq. 3 using the statistics obtained from the training dataset, such as the range, the average (μ), and the standard deviation (σ).

$$X_{scaled} = \frac{X - min(X)}{max(X) - min(X)} \tag{2}$$

$$X_{scaled} = (x - \mu)/\sigma \tag{3}$$

Model Performance Matrix The data of 396 solar cell samples were partitioned into training, validation, and testing datasets according to the ratio of 75 %, 15 %, and 15 % based on randomly selected cells. Then rotations of 90°, 180°, and 270° were applied to each image to increase the number of observations and make the model generalized across different image orientations.

- Training: 1108 videos or 6648 images
- Validation: 236 videos or 1416 images

- Testing: 240 videos or 1440 image

Therefore, there were for training, for validation, and s for testing. Mean squared error (MSE) calculated by Eq. 4 was used as the loss function in the training process. The model performance was evaluated using the root-mean-square error (RMSE) shown in Eq. 5 obtained from the testing dataset. In both Equation 4 and Equation 5, n is the number of observations in the dataset, Y_i is the actual output feature value, and $\hat{Y}_i$ is the predicted output feature value.

$$MSE = \frac{1}{n}\sum_{i=1}^{n}(Y_i - \hat{Y}_i)^2 \tag{4}$$

$$RMSE = \sqrt{\frac{\sum_{i=1}^{n}(Y_i - \hat{Y}_i)^2}{n}} \tag{5}$$

The number of epochs in the training process is denoted by a number in parentheses following the model expression. Models returned from checkpoints, denoted by a letter "c" following the defined training epoch number, were sometimes used to obtain models before overfitting. The checkpoint was set to continuously save model objects with a smaller MSE for the validation dataset in the training process.

Model Training Environment: Tensorflow 2.6.1 library was used for building the neural network model[22]. The model was trained and tested on Intel(R) Xeon(R) CPU E5-2630 v4 @ 2.20GHz, 64 GB memory, 8 CPU cores, and 12 GB Nvidia GeForce RTX 2080 GPU card.

Slurm: stands for Simple Linux Utility for Resource Management, which was initially developed at the Lawrence Livermore National Laboratory. Slurm is a full-featured job scheduler with a multi-threaded core scheduler and substantially high scalability that was used for parallel neural network model training.

The Slurm workload manager is used to submit fleets of jobs in HPC to speed up the process and improve fault tolerance. Figure 39 [23] indicates how a Slurm scheduler takes jobs from a workstation that can be run through its cores and submits them to compute-nodes with robust specifications. The compute and login nodes have access to the storage environment of the home, scratch, and work directories.

Summary: The specification of all cases with differences in the model structure, input, and output is described in Table 10 with the testing RMSE. A baseline model was made by guessing values of output features as one, and its testing RMSE is 0.0958. "Raw" is for the original image in the input column, and "BS" is for the baseline subtraction image. "Hyper" is for the image with multiple channels for different image characterizations, and "EH" is for the enhanced S/N EL image constructed by the three EL images with different forwarding currents. The normalized electrical features were used directly as the output if the output column was left empty. Otherwise, a scaler was applied, where MMS represents the minimum-maximum scaler as Eq. 2 and STS represents the standard scaler as Eq. 3.

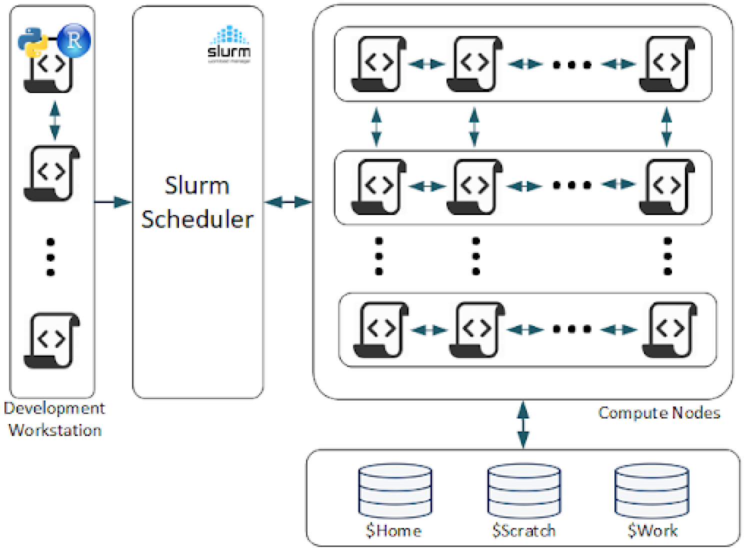

Figure 39: Slurm jobs workflow for parallel model training.

This section explores neural network models to predict the normalized power and series resistance based on EL and PL images for PV modules under accelerated exposures. Figure 40 shows that the baseline subtraction $EL@I_o$ image brings the lowest testing RMSE for the CNN model, and the raw $EL@I_o$ image brings the lowest testing RMSE for the RNN model.

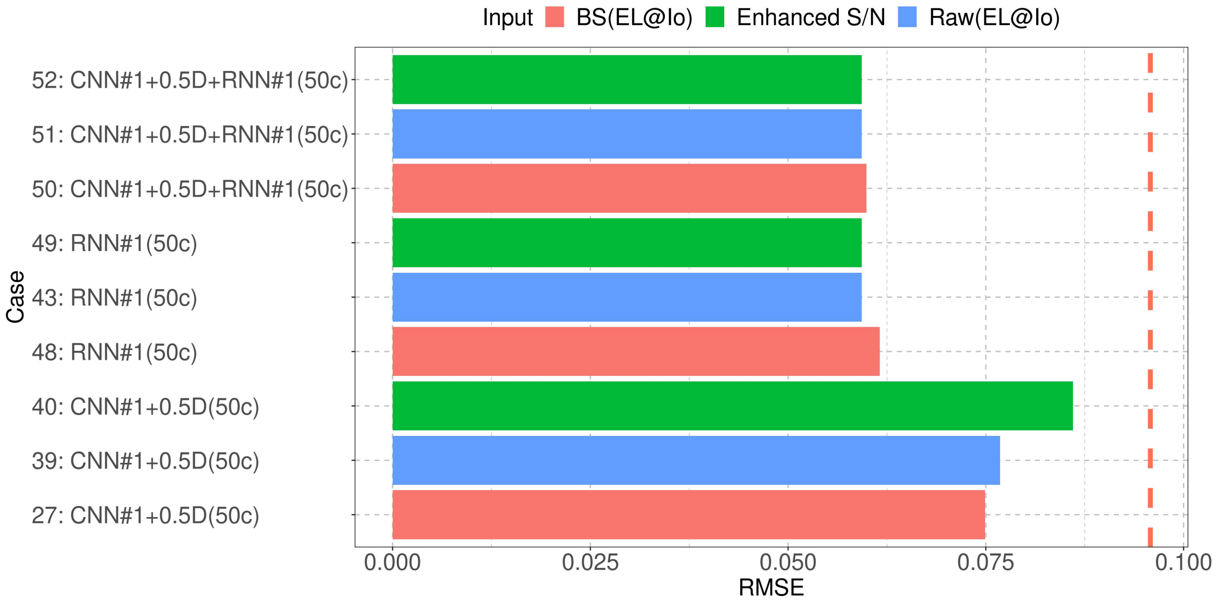

Figure 40: Comparison of the testing RMSE of CNN, RNN and CNN+RNN model examples with three kinds of input images, including the raw $EL@I_o$ images, the baseline subtraction $EL@I_o$ images, and the enhanced S/N EL images.

Incorporating other image characterizations into the input, such as using the enhanced S/N

Table 10: The specification of each modeling experiment and its resulting testing RMSE.

Case	Model Expression	Comments	Input	Output	# of Parameters	RMSE
1	CNN#1(50)		BS($EL@I_o$)		12,918,090	0.0844
2	CNN#1+0.5D(50)	add dropout layer (50%) following each dense layer	BS($EL@I_o$)		12,918,090	0.0735
3	CNN#1+0.5D+RF1(50)	reduce neurons in the first dense layer from 256 to 128	BS($EL@I_o$)		6,462,666	0.0758
4	CNN#1+0.5D+RF2(50)	reduce neurons in the second dense layer from 256 to 128	BS($EL@I_o$)		12,884,938	0.0741
5	CNN#1+0.5D+MP3(50)	change the grid in max pooling as 3 × 3	BS($EL@I_o$)		2,633,034	0.0777
6	CNN#1+0.5D+MP4(50)	change the grid in max pooling as 4 × 4	BS($EL@I_o$)		875,850	0.0780
7	CNN#1+0.5D+KR(50)	add kernel regularization to each convolution layer	BS($EL@I_o$)		12,918,090	0.0742
8	CNN#1+0.5D+AR(50)	add activation regularization to each convolution layer	BS($EL@I_o$)		12,918,090	0.0788
9	CNN#1+0.5D+BNB16(50)	add BNB with a batch size of 16	BS($EL@I_o$)		12,918,186	0.0783
10	CNN#1+0.5D+BNB64(50)	add BNB with a batch size of 64	BS($EL@I_o$)		12,918,186	0.1154
11	CNN#1+0.5D+BNB256(50)	add BNB with a batch size of 256	BS($EL@I_o$)		12,918,186	0.1154
12	CNN#1+0.5D+BNB512(50)	add BNB with a batch size of 512	BS($EL@I_o$)		12,918,186	0.2017
13	CNN#1+0.5D+BNB1024(50)	add BNB with a batch size of 1024	BS($EL@I_o$)		12,918,186	0.5036
14	CNN#1+0.5D+BN16(50)	add BN with a batch size of 16	BS($EL@I_o$)		12,918,346	0.0779
15	CNN#1+0.5D+BN64(50)	add BN with a batch size of 64	BS($EL@I_o$)		12,918,346	0.0783
16	CNN#1+0.5D+BN256(50)	add BN with a batch size of 256	BS($EL@I_o$)		12,918,346	0.0792
17	CNN#1+0.5D+BN512(50)	add BN with a batch size of 512	BS($EL@I_o$)		12,918,346	0.0851
18	CNN#1+0.5D+BN1024(50)	add BN with a batch size of 1024	BS($EL@I_o$)		12,918,346	0.3259
19	CNN#1+0.5D(50)	add dropout layer (50%) following each dense layer	BS($EL@I_o$)	STS	12,918,090	0.0778
20	CNN#1+0.5D+BNB512(50)	add BNB with a batch size of 512	BS($EL@I_o$)	STS	12,918,186	0.0738
21	CNN#1+0.5D+BN512(50)	add BN with a batch size of 512	BS($EL@I_o$)	STS	12,918,346	0.0778
22	CNN#1+0.5D(50)	add dropout layer (50%) following each dense layer	BS($EL@I_o$)	MMS	12,918,090	0.0757
23	CNN#1+0.5D+BNB512(50)	add BNB with a batch size of 512	BS($EL@I_o$)	MMS	12,918,186	0.0788
24	CNN#1+0.5D+BN512(50)	add BN with a batch size of 512	BS($EL@I_o$)	MMS	12,918,346	0.0951
25	CNN#1+0.5D+BNB512(250)	add BNB with a batch size of 512	BS($EL@I_o$)		12,918,186	0.0787
26	CNN#1+0.5D+BN512(250)	add BN with a batch size of 512	BS($EL@I_o$)		12,918,346	0.0798
27	CNN#1+0.5D(50c)	add dropout layer (50%) following each dense layer	BS($EL@I_o$)		12,918,090	0.0749
28	CNN#2+0.5D(50c)	add dropout layer (50%) following each dense layer	BS($EL@I_o$)		25,757,338	0.0730
29	CNN#3+0.5D(50c)	add dropout layer (50%) following each dense layer	BS($EL@I_o$)		25,757,922	0.0742
30	CNN#4+0.5D(50c)	add dropout layer (50%) following each dense layer	BS($EL@I_o$)		12,912,866	0.0738
31	CNN#5+0.5D(50c)	add dropout layer (50%) following each dense layer	BS($EL@I_o$)		12,918,674	0.0737
32	CNN#6+0.5D(50c)	add dropout layer (50%) following each dense layer	BS($EL@I_o$)		12,916,354	0.0752
33	CNN#7+0.5D(50c)	add dropout layer (50%) following each dense layer	BS($EL@I_o$)		12,915,770	0.0754
34	CNN#8+0.5D(50c)	add dropout layer (50%) following each dense layer	BS($EL@I_o$)		6,494,879	0.0737
35	CNN#9+0.5D(50c)	add dropout layer (50%) following each dense layer	BS($EL@I_o$)		6,507,130	0.0738
36	CNN#10+0.5D(50c)	add dropout layer (50%) following each dense layer	BS($EL@I_o$)		6,516,378	0.0734
37	VGG16(T)+0.5D(50c)	trainable VGG16 with the same top layers structure	BS($EL@I_o$)		21,203,778	0.0756
38	VGG16(NT)+0.5D(50c)	non-trainable VGG16 with the same top layers structure	BS($EL@I_o$)		21,203,778	0.0777
39	CNN#1+0.5D(50c)		Raw($EL@I_o$)		12,918,090	0.0768
40	CNN#1+0.5D(50c)		EH		12,918,090	0.0860
41	CNN#1+0.5D(50c)	channel 0: BS($EL@I_o$); channel 1: BS($EL@0.25I_o$)	Hyper		12,918,162	0.0923
42	CNN#1+0.5D(50c)	channel 0: BS($EL@I_o$); channel 1: BS($PL@OC$)	Hyper		12,918,162	0.0922
43	RNN#1(50c)	one GRU layer with units as two	Raw($EL@I_o$)		301,236	0.0593
44	RNN#2(50c)	one GRU layer with units as 20	Raw($EL@I_o$)		3,013,332	0.0597
45	RNN#3(50c)	one GRU layer with units as 200	Raw($EL@I_o$)		30,241,212	0.0631
46	RNN#4(50c)	two GRU layer with units for each layer as two	Raw($EL@I_o$)		301,272	0.0593
47	RNN#5(50c)	three GRU layer with units for each layer as two	Raw($EL@I_o$)		301,308	0.0605
48	RNN#1(50c)	one GRU layer with units as two	BS($EL@I_o$)		301,236	0.0616
49	RNN#1(50c)	one GRU layer with units as two	EH		301,236	0.0593
50	CNN#1+0.5D+RNN#1(50c)	combine CNN#1 before the output layer and RNN#1	BS($EL@I_o$)		12,919,292	0.0599
51	CNN#1+0.5D+RNN#1(50c)	combine CNN#1 before the output layer and RNN#1	Raw($EL@I_o$)		12,919,292	0.0593
52	CNN#1+0.5D+RNN#1(50c)	combine CNN#1 before the output layer and RNN#1	EH		12,919,292	0.0593

EL image or the hyper image, harms CNN models' performance but does not influence the performance of RNN and CNN+RNN models. The lowest testing RMSE for all CNN model variants is 0.0730, and for all RNN model variants is 0.0593. Compared to the performance of the baseline model, the testing RMSE is reduced by 23.8% for CNN models and 38.1% for RNN models at most. Combining the RNN model with one GRU layer, which has the output dimension specified as two, and the raw $EL@I_o$ images as the input is proposed as the best combination to predict the normalized electrical features.

3.5 Indoor/Outdoor Cross-correlation of Minimodule Sets 1-4

The minimodule characterization in this project was completed in BP1 and BP2 as part of:

- ST 3.3, 7.6
- EOP-B

The cross-correlation algorithm was developed in the project to quantify the similarity in the degradation behavior for a module variant under indoor accelerated and outdoor exposure. It took the $< S|R >$ and $< S|M$ models for a module variant under different exposures, their exposure times, and the guessing range of the returned cross-correlation scale factor as inputs. These models described how power and other features change over time. The algorithm returns the optimal cross-correlation scale factor ($CCSF^*$) to quantify the ratio of the changing rate for power for modules under indoor accelerated and outdoor exposures, and the cross-correlation coefficient (CCC) for each feature to evaluate the similarity in trends for the overlapping exposure time between the scaled indoor and outdoor exposures. The cross-correlation scale factor ($CCSF$) is defined as the indoor exposure time divided by the equivalent outdoor exposure time, so it is usually smaller than one, considering that indoor accelerated exposures leading to faster degradation.

The algorithm first compared the two $< S|R >$ models for indoor accelerated and outdoor exposures to solve $CCSF^*$. The y-intercept of the two models were shifted to one to represent a change starting exactly from 100%. Then a value in the guessing range is picked as the $CCSF$ to scale the indoor model. Figure 41 shows the indoor model scaled by two different CCSF values. Next, the overlapping time range between the indoor scaled model and the outdoor model is calculated, and a hundred time points are evenly generated within it. These time points are then input to the scaled indoor and outdoor models to obtain two predicted value sequences, and the root-mean-square error (RMSE) between these two value sequences is calculated. The above process is repeated for every value in the guessing range of $CCSF$ with an interval specification. Finally, the optimal cross-correlation scale factor is decided by the minimum RMSE. In summary, the indoor model is scaled along the time axis to get closest to the outdoor model in their common exposure time, and the corresponding scale factor is $CCSF^*$.

The $CCSF^*$ is then applied to all indoor models, including $< S|R >$ model and various $< S|M$ models. Similar value sequences were generated within the overlapping time range from a pair of outdoor models and the indoor model scaled by $CCSF^*$. Then Pearson correlation coefficient is then calculated instead of RMSE between the two value sequences and named the cross-correlation coefficient (CCC). It can quantify the similarity in trends of the outdoor model and the scaled indoor model in their overlapping time region. When their trends are more identical, the CCC is closer to one, and when they are more opposite, the CCC is closer to minus one. The CCC can be obtained for each pathway. In this study, we set the guessing range of $CCSF$ as from 0.04 to 2, which means that the indoor model can be compressed into half of its original exposure time and stretched into 25 times its original exposure time. The $< S|R >$ model was $< Time|^nP_{mp,IV} >$, and the mechanism features were $^nI_{sc,IV}$, $^nR_{s,IV}$, and $^nV_{mp,PIV}$. It is worth noting that when using CCC to evaluate the similarity of degradation behavior under different exposures, the CCC of the activated degradation mechanism feature should be the focus due to its significant contribution to the total power loss. In our study,

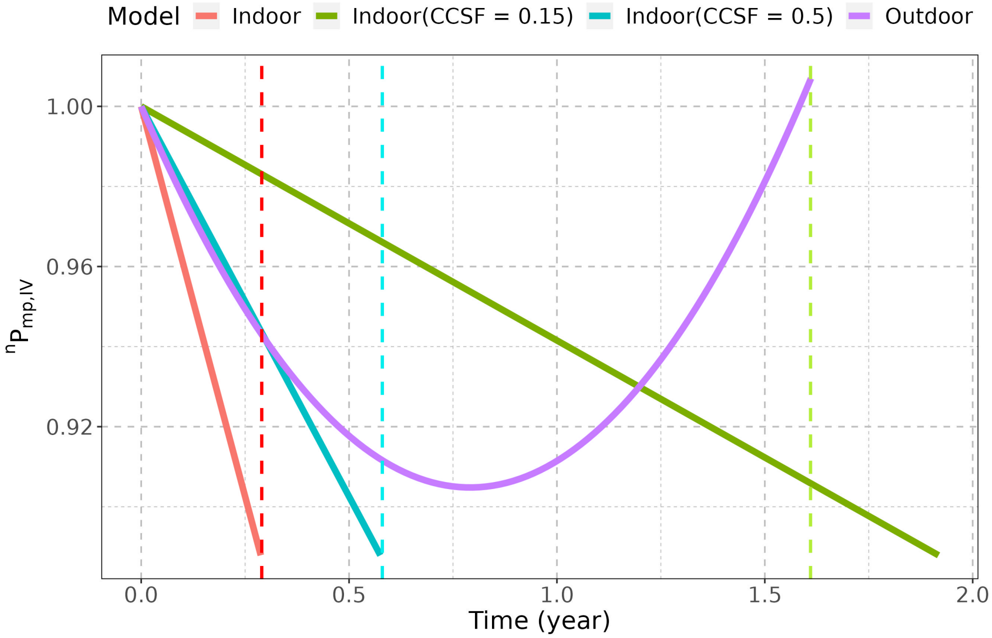

Figure 41: Illustration of the process to obtain the optimal cross-correlation scale factor ($CCSF^*$) by comparing the scaled indoor model and outdoor model in their overlapping exposure time.

outdoor modules experienced changes in both $^nI_{sc,IV}$ and $^nR_{s,IV}$, but indoor modules only had prominent changes only in $^nR_{s,IV}$. Therefore, only the $^nR_{s,IV}$ is for the activated degradation mechanism in common. Even if the CCC results for $^nI_{sc,IV}$ and $^nV_{mp,PIV}$ turn out to be close to one, the degradation behavior between exposures can not be concluded as similar due to the difference in activated degradation mechanisms.

The $CCSF^*$ and CCC of each pathway for comparing the degradation behavior of each module variant between mDH and the outdoor exposure is shown in Table 11. According to the success criteria listed in project SOPO, we had five module variants satisfying the requirements of $CCSF^*$ smaller than 0.5 and CCC of $^nP_{mp,IV}$ higher than 0.7. When the $< S|R >$ models have opposite trends or one $< S|R >$ model exhibits much slower change than the other, the indoor $< S|R >$ model tends to continuously compress or stretch itself to get close to the outdoor model. As can be seen from the results in table 11, all cases with a negative CCC for $^nP_{mp,IV}$ also have a $CCSF^*$ appearing at the guessing boundaries. Ten module variants have a $CCSF^*$ not appearing on the guessing boundaries. Their $CCSF^*$ varies from 0.122 to 1.08, with an average of 0.4739. Their average CCC for $^nP_{mp,IV}$ and $^nR_{s,IV}$ were 0.94 and 0.89, respectively, which were much higher than those for $^nI_{sc,IV}$ and $^nV_{mp,PIV}$ as 0.11 and -0.43, respectively.

The cross-correlation results comparing module degradation under mDH+FSL and the outdoor exposure are listed in Table 12. There were six module variants satisfying the criteria of a $CCSF^*$ lower than 0.5 and a CCC for $^nP_{mp,IV}$ higher than 0.7. There were ten module variants with the $CCSF^*$ not appearing on the guessing boundaries, which were identical to those found in comparing mDH and the outdoor exposure. Their average $CCSF^*$ is 0.4298, and the CCC for $^nP_{mp,IV}$ and $^nR_{s,IV}$ are still much closer to one than those of the other two features. The average CCC for $^nP_{mp,IV}$ and $^nR_{s,IV}$ are 0.82 and 0.78. Compared to the results of mDH, the

Table 11: The results of $CCSF^*$ and CCC comparing the models for each module variant under mDH and the outdoor exposure.

Module variant	$CCSF^*$	CCC			
		$< Time \vert {}^nP_{mp,IV} >$	$< Time \vert {}^nI_{sc,IV}$	$< Time \vert {}^nR_{s,IV}$	$< Time \vert {}^nV_{mp,PIV}$
1	2.000	0.804	0.999	0.968	1.000
2	2.000	0.374	0.307	0.783	0.968
3	2.000	-0.858	-0.925	0.968	1.000
4	**0.169**	0.726	0.561	0.259	0.068
5	**0.511**	0.959	0.716	0.968	-1.000
6	2.000	0.778	0.968	0.962	-0.860
7	**0.210**	1.000	-0.112	0.888	-0.515
8	**0.792**	0.935	-0.747	0.884	-0.586
9	**0.398**	0.972	0.893	0.999	0.231
10	**0.122**	0.885	-0.461	0.979	0.601
11	**0.584**	0.999	0.648	0.999	-0.649
12	2.000	-1.000	-0.775	-1.000	0.586
13	0.040	-0.696	-0.658	0.913	0.998
14	**0.210**	0.994	-0.918	1.000	-0.448
15	**1.089**	0.953	0.673	0.968	-1.000
16	**0.654**	1.000	-0.127	0.979	-0.994

difference is mainly due to the results of module variant 9. The average CCC for ${}^nI_{sc,IV}$ and ${}^nV_{mp,PIV}$ are 0.29 and 0.01. The CCC for ${}^nI_{sc,IV}$ is higher when comparing mDH+FSL and the outdoor exposure than that when comparing mDH, which is caused by a slightly more decrease in ${}^nI_{sc,IV}$ for modules under mDH+FSL.

Table 12: The results of $CCSF^*$ and CCC comparing the models for each module variant under mDH+FSL and the outdoor exposure.

Module variant	$CCSF^*$	CCC			
		$< Time\vert^n P_{mp,IV} >$	$< Time\vert^n I_{sc,IV}$	$< Time\vert^n R_{s,IV}$	$< Time\vert^n V_{mp,PIV}$
1	2.000	0.999	0.978	0.944	0.846
2	2.000	0.378	0.414	0.783	0.868
3	2.000	-0.968	-1.000	0.999	0.645
4	**0.168**	0.862	-0.602	0.439	0.524
5	**0.599**	0.968	0.612	0.968	-0.129
6	2.000	0.800	0.968	0.937	-1.000
7	**0.207**	1.000	-0.183	0.978	-0.670
8	**0.475**	0.964	0.981	0.968	-0.948
9	**0.063**	-0.308	-0.006	-0.406	0.260
10	**0.188**	0.864	0.349	0.988	0.275
11	**0.576**	0.968	0.995	0.968	0.821
12	2.000	-0.939	-0.975	-1.000	-1.000
13	0.040	-0.560	0.678	0.918	-0.979
14	**0.357**	1.000	-0.865	1.000	0.038
15	**0.448**	0.985	0.899	0.968	-0.616
16	**1.217**	0.932	0.731	0.940	0.563

4 Publications/Presentations

This is part of Task 4 and EOP-D. The complete set of publications and presentations are listed below.

- Statistical Analysis and Degradation Pathway Modeling of PERC PV Minimodules with Different Packaging Strategies in Indoor Accelerated Exposures

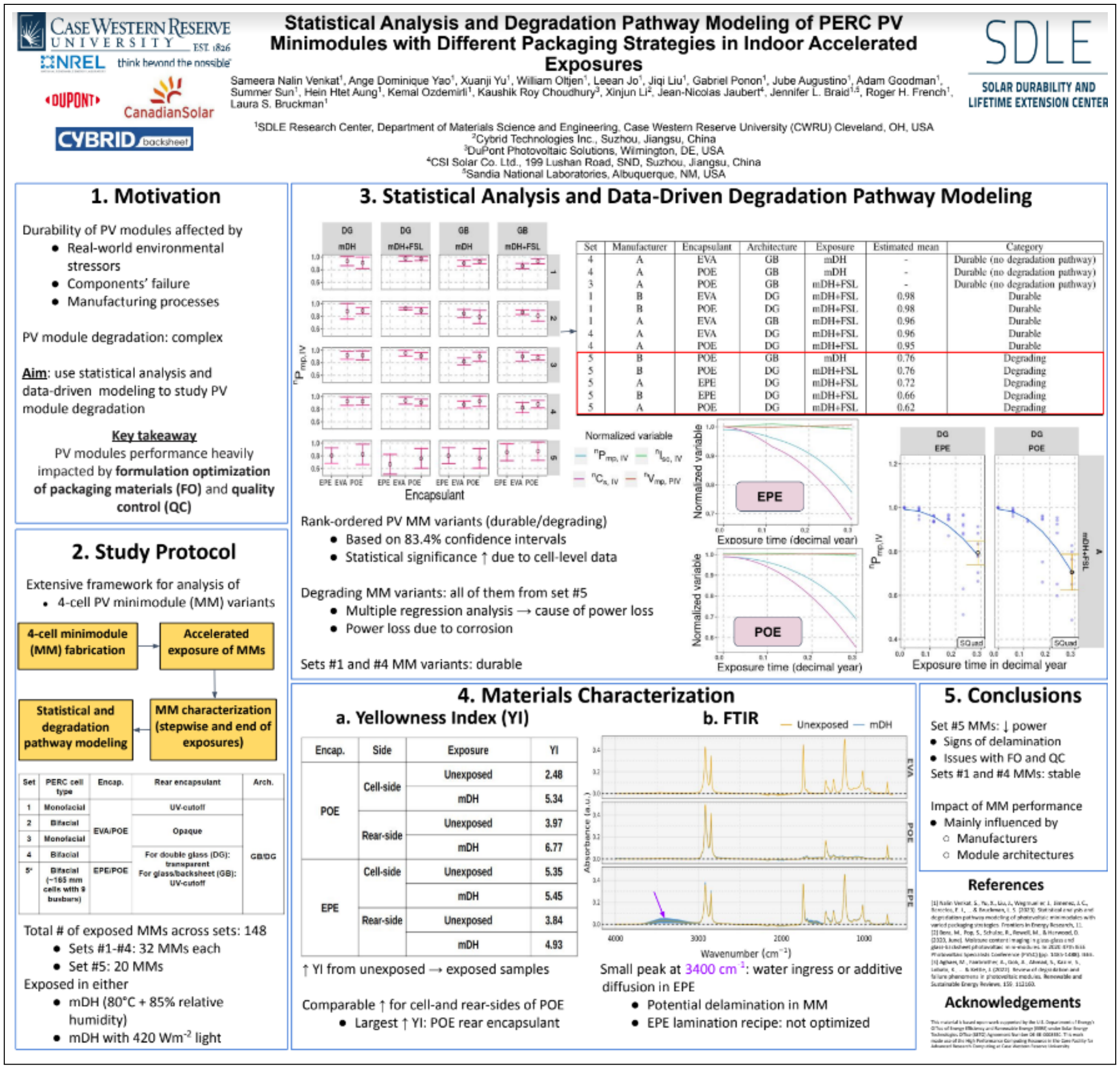

Statistical Analysis and Degradation Pathway Modeling of PERC PV Minimodules with Different Packaging Strategies in Indoor Accelerated Exposures

Sameera Nalin Venkat[1], Ange Dominique Yao[1], Xuanji Yu[1], William Oltjen[1], Leean Jo[1], Jiqi Liu[1], Gabriel Ponon[1], Jube Augustino[1], Adam Goodman[1], Summer Sun[1], Hein Htet Aung[1], Kemal Ozdemirli[1], Kaushik Roy Choudhury[3], Xinjun Li[2], Jean-Nicolas Jaubert[4], Jennifer L. Braid[1,5], Roger H. French[1], Laura S. Bruckman[1]

[1]SDLE Research Center, Department of Materials Science and Engineering, Case Western Reserve University (CWRU) Cleveland, OH, USA
[2]Cybrid Technologies Inc., Suzhou, Jiangsu, China
[3]DuPont Photovoltaic Solutions, Wilmington, DE, USA
[4]CSI Solar Co. Ltd., 199 Lushan Road, SND, Suzhou, Jiangsu, China
[5]Sandia National Laboratories, Albuquerque, NM, USA

1. Motivation

Durability of PV modules affected by
- Real-world environmental stressors
- Components' failure
- Manufacturing processes

PV module degradation: complex

Aim: use statistical analysis and data-driven modeling to study PV module degradation

Key takeaway

PV modules performance heavily impacted by **formulation optimization of packaging materials (FO)** and **quality control (QC)**

2. Study Protocol

Extensive framework for analysis of
- 4-cell PV minimodule (MM) variants

4-cell minimodule (MM) fabrication → **Accelerated exposure of MMs** → **MM characterization (stepwise and end of exposures)** → **Statistical and degradation pathway modeling**

Set	PERC cell type	Encap.	Rear encapsulant	Arch.
1	Monofacial	EVA/POE	UV-cutoff	GB/DG
2	Bifacial		Opaque	
3	Monofacial			
4	Bifacial		For double glass (DG): transparent For glass/backsheet (GB): UV-cutoff	
5*	Bifacial (~165 mm cells with 9 busbars)	EPE/POE		

Total # of exposed MMs across sets: 148
- Sets #1-#4: 32 MMs each
- Set #5: 20 MMs

Exposed in either
- mDH (80°C + 85% relative humidity)
- mDH with 420 Wm^{-2} light

3. Statistical Analysis and Data-Driven Degradation Pathway Modeling

Set	Manufacturer	Encapsulant	Architecture	Exposure	Estimated mean	Category
4	A	EVA	GB	mDH	-	Durable (no degradation pathway)
4	A	POE	GB	mDH	-	Durable (no degradation pathway)
3	A	POE	GB	mDH+FSL	-	Durable (no degradation pathway)
1	B	EVA	DG	mDH+FSL	0.98	Durable
1	B	POE	DG	mDH+FSL	0.98	Durable
1	A	EVA	GB	mDH+FSL	0.96	Durable
4	A	EVA	DG	mDH+FSL	0.96	Durable
4	A	POE	DG	mDH+FSL	0.95	Durable
5	B	POE	GB	mDH	0.76	Degrading
5	B	POE	DG	mDH+FSL	0.76	Degrading
5	A	EPE	DG	mDH+FSL	0.72	Degrading
5	B	EPE	DG	mDH+FSL	0.66	Degrading
5	A	POE	DG	mDH+FSL	0.62	Degrading

Rank-ordered PV MM variants (durable/degrading)
- Based on 83.4% confidence intervals
- Statistical significance ↑ due to cell-level data

Degrading MM variants: all of them from set #5
- Multiple regression analysis → cause of power loss
- Power loss due to corrosion

Sets #1 and #4 MM variants: durable

4. Materials Characterization

a. Yellowness Index (YI)

Encap.	Side	Exposure	YI
POE	Cell-side	Unexposed	2.48
		mDH	5.34
	Rear-side	Unexposed	3.97
		mDH	6.77
EPE	Cell-side	Unexposed	5.35
		mDH	5.45
	Rear-side	Unexposed	3.84
		mDH	4.93

↑ YI from unexposed → exposed samples

Comparable ↑ for cell-and rear-sides of POE
- Largest ↑ YI: POE rear encapsulant

b. FTIR

Small peak at 3400 cm^{-1}: water ingress or additive diffusion in EPE
- Potential delamination in MM
- EPE lamination recipe: not optimized

5. Conclusions

Set #5 MMs: ↓ power
- Signs of delamination
- Issues with FO and QC

Sets #1 and #4 MMs: stable

Impact of MM performance
- Mainly influenced by
  - Manufacturers
  - Module architectures

References

Acknowledgements

Figure 42: Poster presentation at PVSC 50th in Puerto Rico.

- Statistical analysis and degradation pathway modeling of photovoltaic minimodules with varied packaging strategies
- Quantitative Learning from Spatiotemporal Image Datasets: Application to Degradation of Silicon Photovoltaic Modules
  - poster, 8th Annual Data science in Eng & Life Sci Symposium 2022 44.

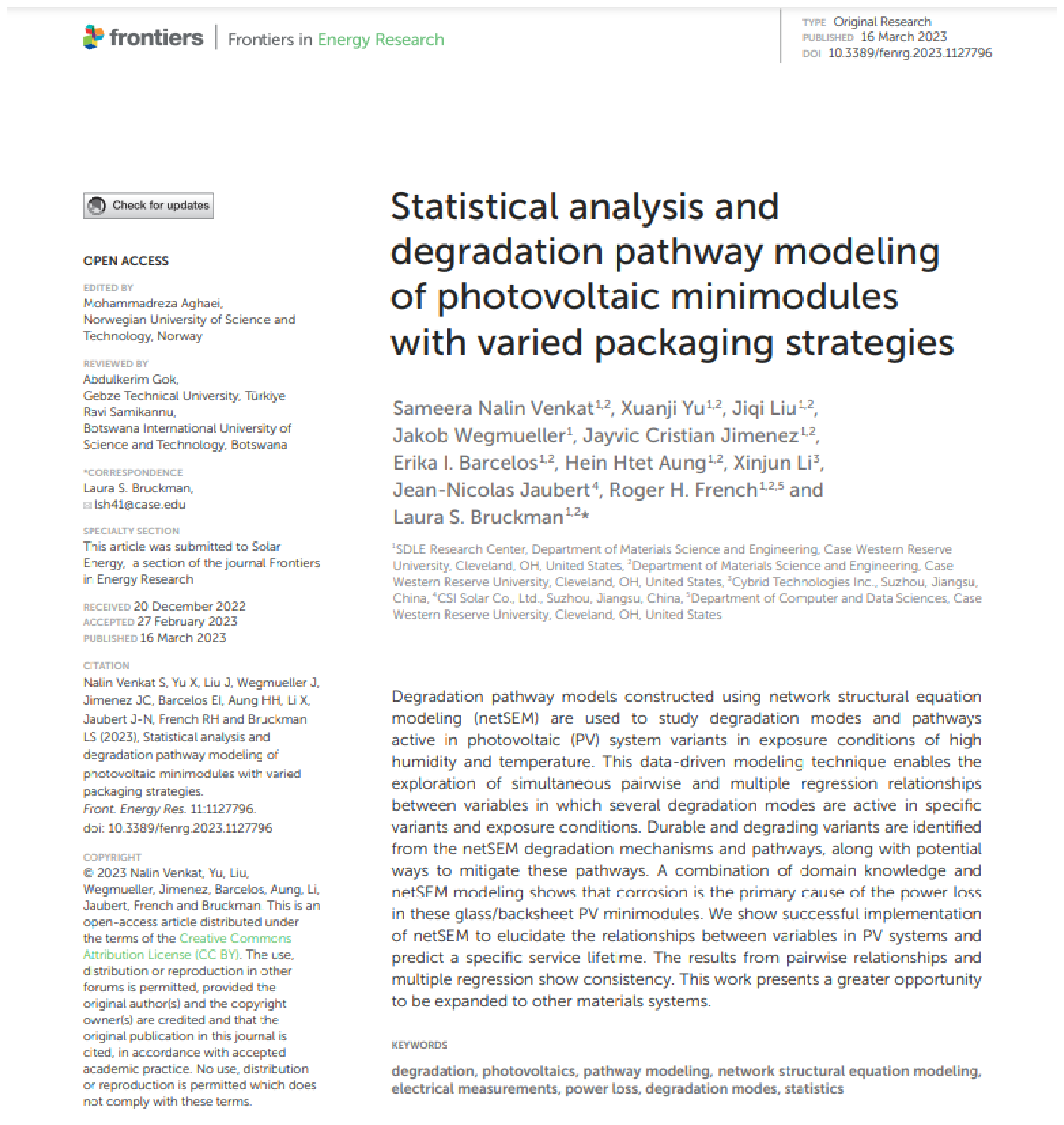

frontiers | Frontiers in Energy Research

TYPE Original Research
PUBLISHED 16 March 2023
DOI 10.3389/fenrg.2023.1127796

Check for updates

OPEN ACCESS

EDITED BY
Mohammadreza Aghaei,
Norwegian University of Science and Technology, Norway

REVIEWED BY
Abdulkerim Gok,
Gebze Technical University, Türkiye
Ravi Samikannu,
Botswana International University of Science and Technology, Botswana

*CORRESPONDENCE
Laura S. Bruckman,
✉ lsh41@case.edu

SPECIALTY SECTION
This article was submitted to Solar Energy, a section of the journal Frontiers in Energy Research

RECEIVED 20 December 2022
ACCEPTED 27 February 2023
PUBLISHED 16 March 2023

CITATION
Nalin Venkat S, Yu X, Liu J, Wegmueller J, Jimenez JC, Barcelos EI, Aung HH, Li X, Jaubert J-N, French RH and Bruckman LS (2023), Statistical analysis and degradation pathway modeling of photovoltaic minimodules with varied packaging strategies.
Front. Energy Res. 11:1127796.
doi: 10.3389/fenrg.2023.1127796

Statistical analysis and degradation pathway modeling of photovoltaic minimodules with varied packaging strategies

Sameera Nalin Venkat[1,2], Xuanji Yu[1,2], Jiqi Liu[1,2], Jakob Wegmueller[1], Jayvic Cristian Jimenez[1,2], Erika I. Barcelos[1,2], Hein Htet Aung[1,2], Xinjun Li[3], Jean-Nicolas Jaubert[4], Roger H. French[1,2,5] and Laura S. Bruckman[1,2]*

[1]SDLE Research Center, Department of Materials Science and Engineering, Case Western Reserve University, Cleveland, OH, United States, [2]Department of Materials Science and Engineering, Case Western Reserve University, Cleveland, OH, United States, [3]Cybrid Technologies Inc., Suzhou, Jiangsu, China, [4]CSI Solar Co., Ltd., Suzhou, Jiangsu, China, [5]Department of Computer and Data Sciences, Case Western Reserve University, Cleveland, OH, United States

Degradation pathway models constructed using network structural equation modeling (netSEM) are used to study degradation modes and pathways active in photovoltaic (PV) system variants in exposure conditions of high humidity and temperature. This data-driven modeling technique enables the exploration of simultaneous pairwise and multiple regression relationships between variables in which several degradation modes are active in specific variants and exposure conditions. Durable and degrading variants are identified from the netSEM degradation mechanisms and pathways, along with potential ways to mitigate these pathways. A combination of domain knowledge and netSEM modeling shows that corrosion is the primary cause of the power loss in these glass/backsheet PV minimodules. We show successful implementation of netSEM to elucidate the relationships between variables in PV systems and predict a specific service lifetime. The results from pairwise relationships and multiple regression show consistency. This work presents a greater opportunity to be expanded to other materials systems.

KEYWORDS

degradation, photovoltaics, pathway modeling, network structural equation modeling, electrical measurements, power loss, degradation modes, statistics

Figure 43: Journal article published.

- poster, MDS-Rely Rely Center 2022 Spring Meeting 44

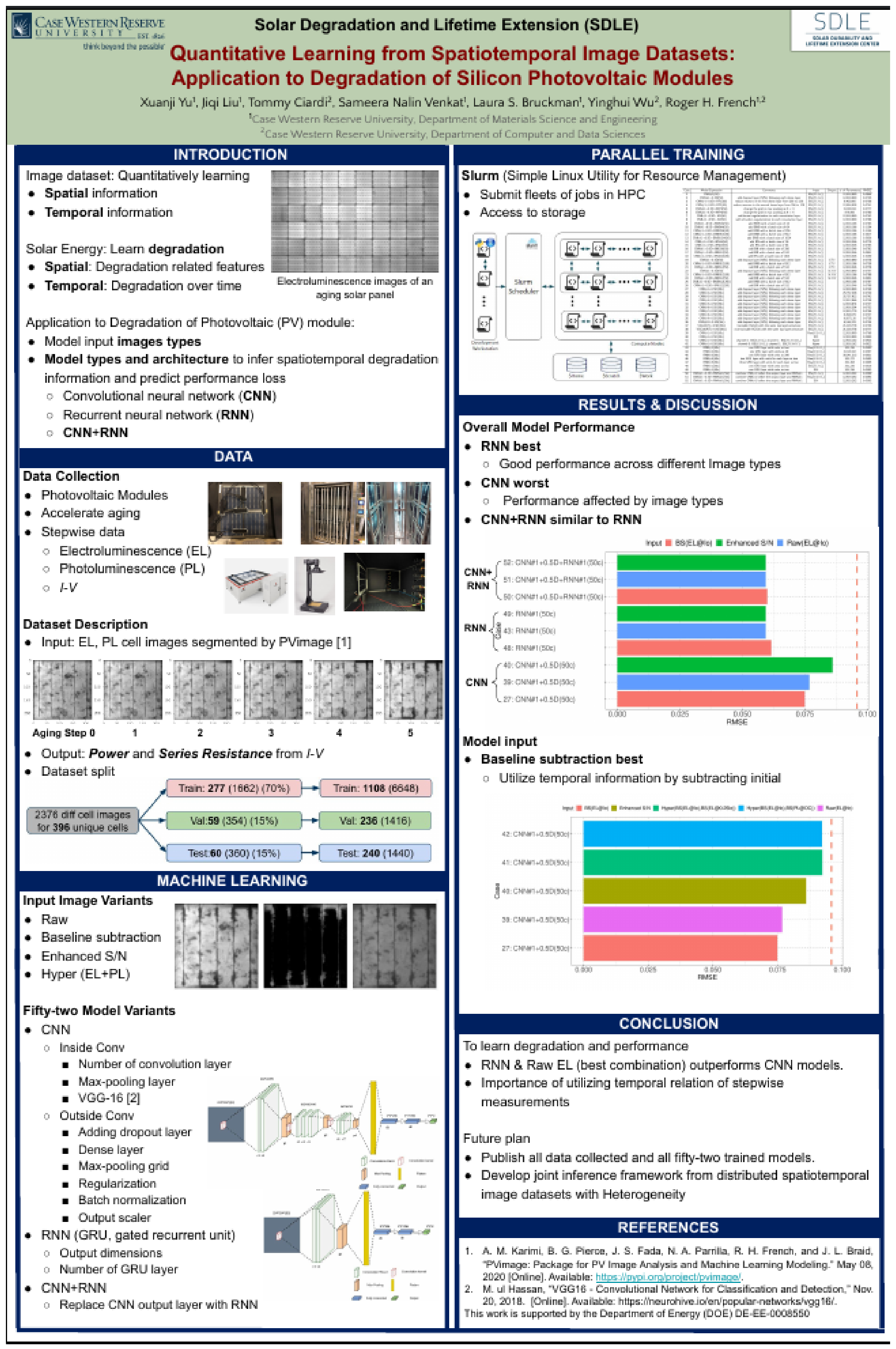

Solar Degradation and Lifetime Extension (SDLE)

Quantitative Learning from Spatiotemporal Image Datasets: Application to Degradation of Silicon Photovoltaic Modules

Xuanji Yu[1], Jiqi Liu[1], Tommy Ciardi[2], Sameera Nalin Venkat[1], Laura S. Bruckman[1], Yinghui Wu[2], Roger H. French[1,2]
[1]Case Western Reserve University, Department of Materials Science and Engineering
[2]Case Western Reserve University, Department of Computer and Data Sciences

INTRODUCTION

Image dataset: Quantitatively learning
- **Spatial** information
- **Temporal** information

Solar Energy: Learn **degradation**
- **Spatial**: Degradation related features
- **Temporal**: Degradation over time

Electroluminescence images of an aging solar panel

Application to Degradation of Photovoltaic (PV) module:
- Model input **images types**
- **Model types and architecture** to infer spatiotemporal degradation information and predict performance loss
  - Convolutional neural network (**CNN**)
  - Recurrent neural network (**RNN**)
  - **CNN+RNN**

DATA

Data Collection
- Photovoltaic Modules
- Accelerate aging
- Stepwise data
  - Electroluminescence (EL)
  - Photoluminescence (PL)
  - *I-V*

Dataset Description
- Input: EL, PL cell images segmented by PVimage [1]

- Output: ***Power*** and ***Series Resistance*** from *I-V*
- Dataset split

2378 diff cell images for **396** unique cells
Train: **277** (1662) (70%) → Train: **1108** (6648)
Val:**59** (354) (15%) → Val: **236** (1416)
Test:**60** (360) (15%) → Test: **240** (1440)

MACHINE LEARNING

Input Image Variants
- Raw
- Baseline subtraction
- Enhanced S/N
- Hyper (EL+PL)

Fifty-two Model Variants
- CNN
  - Inside Conv
    - Number of convolution layer
    - Max-pooling layer
    - VGG-16 [2]
  - Outside Conv
    - Adding dropout layer
    - Dense layer
    - Max-pooling grid
    - Regularization
    - Batch normalization
    - Output scaler
- RNN (GRU, gated recurrent unit)
  - Output dimensions
  - Number of GRU layer
- CNN+RNN
  - Replace CNN output layer with RNN

PARALLEL TRAINING

Slurm (Simple Linux Utility for Resource Management)
- Submit fleets of jobs in HPC
- Access to storage

RESULTS & DISCUSSION

Overall Model Performance
- **RNN best**
  - Good performance across different Image types
- **CNN worst**
  - Performance affected by image types
- **CNN+RNN similar to RNN**

Model input
- **Baseline subtraction best**
  - Utilize temporal information by subtracting initial

CONCLUSION

To learn degradation and performance
- RNN & Raw EL (best combination) outperforms CNN models.
- Importance of utilizing temporal relation of stepwise measurements

Future plan
- Publish all data collected and all fifty-two trained models.
- Develop joint inference framework from distributed spatiotemporal image datasets with Heterogeneity

REFERENCES

1. A. M. Karimi, B. G. Pierce, J. S. Fada, N. A. Parrilla, R. H. French, and J. L. Braid, "PVimage: Package for PV Image Analysis and Machine Learning Modeling." May 08, 2020 [Online]. Available: https://pypi.org/project/pvimage/.
2. M. ul Hassan, "VGG16 - Convolutional Network for Classification and Detection," Nov. 20, 2018. [Online]. Available: https://neurohive.io/en/popular-networks/vgg16/.

This work is supported by the Department of Energy (DOE) DE-EE-0008550

Figure 44: A poster in Data science in Eng & Life Sci Symposium 2022 and MDS-Rely 2022.

- Materials Data Science Research with SDLE Lab, Poster, Biomedical Engineering Society 2022 45

Materials Data Science Research with SDLE Lab

Kemal Ozdemirli

Towards 50 Project

- Identify the advances needed to increase the lifetime of solar PV modules to 50 years
- Analyzing impact of:
  - Packing Materials
    - Encapsulants: Ethylene-vinyl acetate and Polyolefin elastomers (EVA and POE)
    - Backsheet: Fluorinated Composite (KPf)
  - Different Types of Solar Modules
    - Glass Backsheet (GB)
    - Double Glass Backsheet (GB)
  - Used most common Multicrystalline Silicon

How we tested our Solar Panel Modules?

- We tested two different companies' PV modules (Manufacture A and B)
  - Half of Manufacturer A's panels were exposed outdoor
  - The rest of A and B manufacturer solar panels were exposed to indoor accelerated testing
    - Modified Damp Heat 85 degree C exposure chamber (mDH) for 21 days
    - Modified Damp Heat 85 degree C exposure chamber (mDH) for 14 days and full spectrum light (FS) for 7 days
- We performed different types of measuring for the PV modules
  - Mechanical (4-pt bending proof test)
  - Electrical (I-V, Suns-Voc, PL, EL)
  - Chemical degradation (FL) signal

What to do with the acquired data from the tested Modules?

- Using network structural equation modeling (netSEM) to predict the service lifetime of solar panels
  - It is used to analyze systems that experience degradation of materials that are exposed to a specific stressor (independent variable)
- We are looking for a <Stressor|Mechanism|Response> framework
  - Stressor Variable (S)
    - Service Lifetime of PV Module (dy)
  - Mechanism Variables (M)
    - Short Circuit Current (n_Isc_IV)
    - Series Resistance (n_Rs_IV)
    - Voltage Maximum Power (n_Vmp_IV)
  - Response Variable (R)
    - PV Module Voltage Output (n_Pmp_IV)
- Two types of netSEM Principles used
  - Principle 1
  - Principle 2

Principle 1

- Principle 1 explores direct relationships between pairs of variables in which gives us an inferential model
  - It is fitted using a Mavorikan process (pairwise correlation)
- Principle 1 uses <S|M|R>, <S|R>, <M|R> when generating datasets
  - It explores direct relationship between pairs of variables that gives us an inferential model

Principle 2

- Principle 2 uses <S|M|R> when generating datasets
- Uses multiple regression models that incorporate stepAIC to avoid complex models and overfitting the data
- Principle 2 is a predictive model since it considers impact from other mechanistic variables as well instead of just one variable in which will affect the solar panel durability

Sample of Principle 2 Dataset Single Glass Backsheet Samples

POE Polymer Results

Graph Key:
- Red: Raw Data Points
- Blue: Plotted P2 Equations
- n_Isc_IV: Orange
- n_RS_IV: Green
- n_Vmp_PIV: Purple

Figure 45: A poster in Biomedical Engineering Society 2022.

- Performance Losses and Activated Mechanisms in Monofacial and Bifacial, Double Glass and Glass-backsheet Photovoltaic Modules with PERC Cells, under Accelerated Exposures, poster, PVRW 2022 46

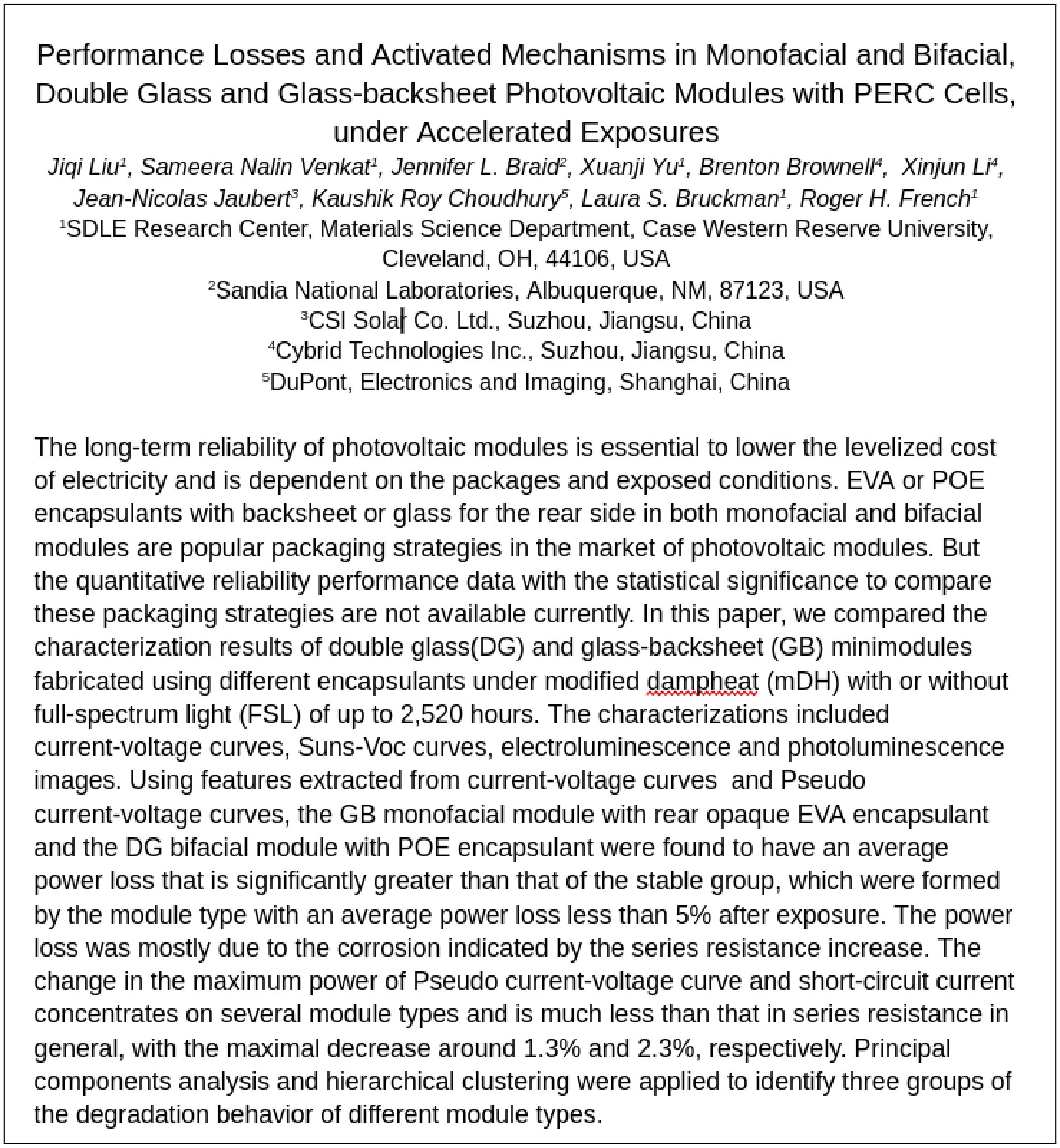

Performance Losses and Activated Mechanisms in Monofacial and Bifacial, Double Glass and Glass-backsheet Photovoltaic Modules with PERC Cells, under Accelerated Exposures

Jiqi Liu[1], Sameera Nalin Venkat[1], Jennifer L. Braid[2], Xuanji Yu[1], Brenton Brownell[4], Xinjun Li[4], Jean-Nicolas Jaubert[3], Kaushik Roy Choudhury[5], Laura S. Bruckman[1], Roger H. French[1]
[1]SDLE Research Center, Materials Science Department, Case Western Reserve University, Cleveland, OH, 44106, USA
[2]Sandia National Laboratories, Albuquerque, NM, 87123, USA
[3]CSI Solar Co. Ltd., Suzhou, Jiangsu, China
[4]Cybrid Technologies Inc., Suzhou, Jiangsu, China
[5]DuPont, Electronics and Imaging, Shanghai, China

The long-term reliability of photovoltaic modules is essential to lower the levelized cost of electricity and is dependent on the packages and exposed conditions. EVA or POE encapsulants with backsheet or glass for the rear side in both monofacial and bifacial modules are popular packaging strategies in the market of photovoltaic modules. But the quantitative reliability performance data with the statistical significance to compare these packaging strategies are not available currently. In this paper, we compared the characterization results of double glass(DG) and glass-backsheet (GB) minimodules fabricated using different encapsulants under modified dampheat (mDH) with or without full-spectrum light (FSL) of up to 2,520 hours. The characterizations included current-voltage curves, Suns-Voc curves, electroluminescence and photoluminescence images. Using features extracted from current-voltage curves and Pseudo current-voltage curves, the GB monofacial module with rear opaque EVA encapsulant and the DG bifacial module with POE encapsulant were found to have an average power loss that is significantly greater than that of the stable group, which were formed by the module type with an average power loss less than 5% after exposure. The power loss was mostly due to the corrosion indicated by the series resistance increase. The change in the maximum power of Pseudo current-voltage curve and short-circuit current concentrates on several module types and is much less than that in series resistance in general, with the maximal decrease around 1.3% and 2.3%, respectively. Principal components analysis and hierarchical clustering were applied to identify three groups of the degradation behavior of different module types.

Figure 46: A poster in PVRW 2022.

- Overall Performance Losses and Activated Mechanisms in Double Glass and Glass-backsheet Photovoltaic Modules with Monofacial and Bifacial PERC Cells, under Accelerated Exposures, conference proceeding, PVSC 49th 47

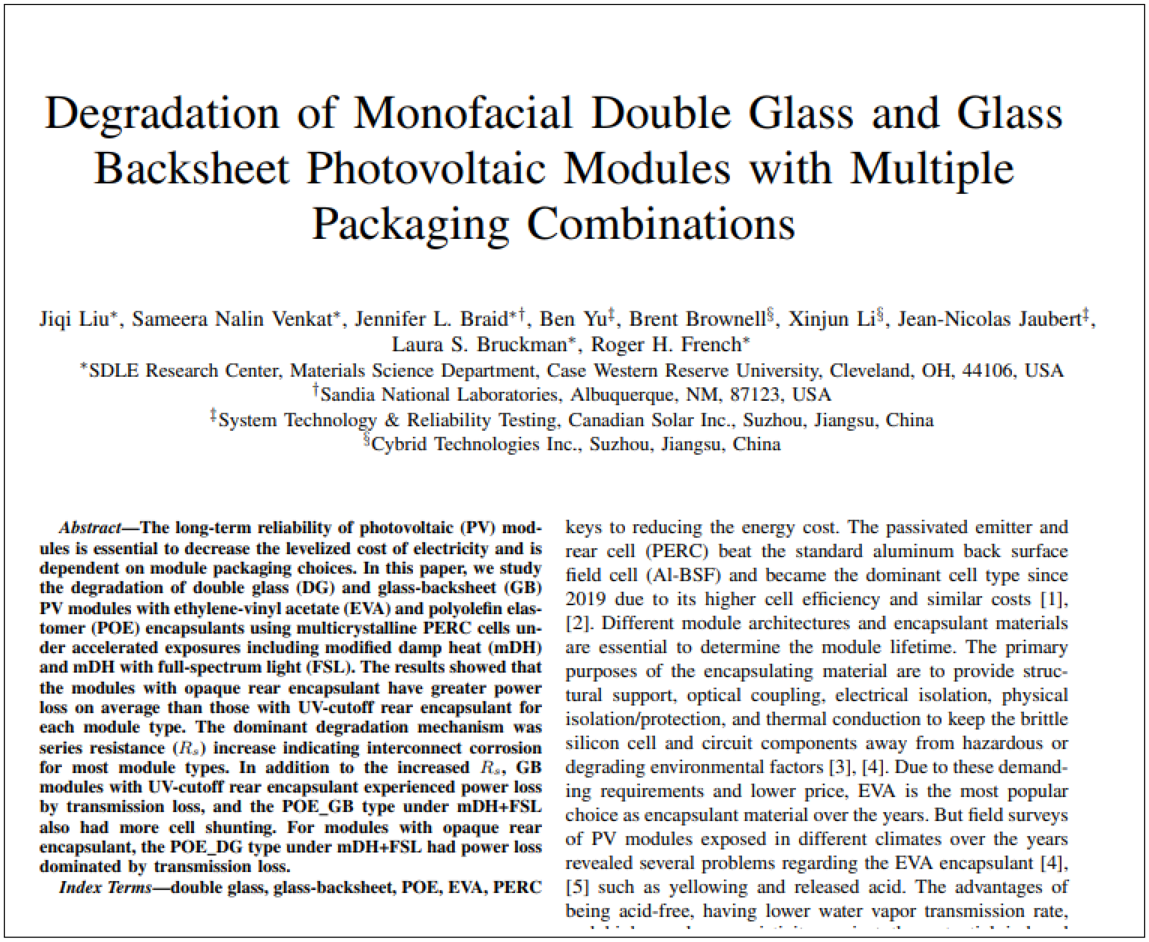

Degradation of Monofacial Double Glass and Glass Backsheet Photovoltaic Modules with Multiple Packaging Combinations

Jiqi Liu*, Sameera Nalin Venkat*, Jennifer L. Braid*†, Ben Yu‡, Brent Brownell§, Xinjun Li§, Jean-Nicolas Jaubert‡,
Laura S. Bruckman*, Roger H. French*
*SDLE Research Center, Materials Science Department, Case Western Reserve University, Cleveland, OH, 44106, USA
†Sandia National Laboratories, Albuquerque, NM, 87123, USA
‡System Technology & Reliability Testing, Canadian Solar Inc., Suzhou, Jiangsu, China
§Cybrid Technologies Inc., Suzhou, Jiangsu, China

***Abstract*—The long-term reliability of photovoltaic (PV) modules is essential to decrease the levelized cost of electricity and is dependent on module packaging choices. In this paper, we study the degradation of double glass (DG) and glass-backsheet (GB) PV modules with ethylene-vinyl acetate (EVA) and polyolefin elastomer (POE) encapsulants using multicrystalline PERC cells under accelerated exposures including modified damp heat (mDH) and mDH with full-spectrum light (FSL). The results showed that the modules with opaque rear encapsulant have greater power loss on average than those with UV-cutoff rear encapsulant for each module type. The dominant degradation mechanism was series resistance (R_s) increase indicating interconnect corrosion for most module types. In addition to the increased R_s, GB modules with UV-cutoff rear encapsulant experienced power loss by transmission loss, and the POE_GB type under mDH+FSL also had more cell shunting. For modules with opaque rear encapsulant, the POE_DG type under mDH+FSL had power loss dominated by transmission loss.**

***Index Terms*—double glass, glass-backsheet, POE, EVA, PERC**

keys to reducing the energy cost. The passivated emitter and rear cell (PERC) beat the standard aluminum back surface field cell (Al-BSF) and became the dominant cell type since 2019 due to its higher cell efficiency and similar costs [1], [2]. Different module architectures and encapsulant materials are essential to determine the module lifetime. The primary purposes of the encapsulating material are to provide structural support, optical coupling, electrical isolation, physical isolation/protection, and thermal conduction to keep the brittle silicon cell and circuit components away from hazardous or degrading environmental factors [3], [4]. Due to these demanding requirements and lower price, EVA is the most popular choice as encapsulant material over the years. But field surveys of PV modules exposed in different climates over the years revealed several problems regarding the EVA encapsulant [4], [5] such as yellowing and released acid. The advantages of being acid-free, having lower water vapor transmission rate,

Figure 47: A conference proceeding article in PVSC 49th.

- Degradation Pathway Modeling of PV Minimodule Variants with Different Packaging Materials Under Indoor Accelerated Exposures, conference proceeding, PVSC 49th 48

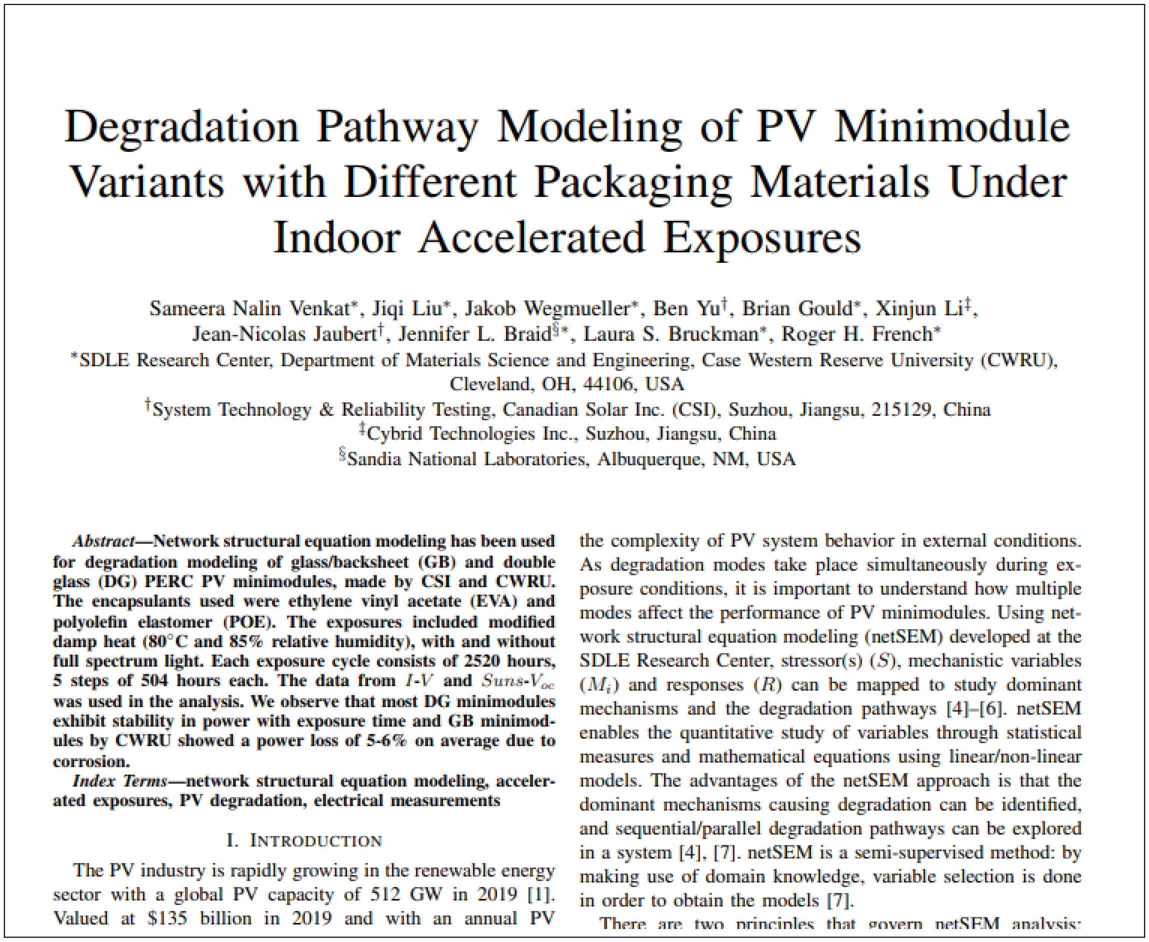

Degradation Pathway Modeling of PV Minimodule Variants with Different Packaging Materials Under Indoor Accelerated Exposures

Sameera Nalin Venkat*, Jiqi Liu*, Jakob Wegmueller*, Ben Yu†, Brian Gould*, Xinjun Li‡,
Jean-Nicolas Jaubert†, Jennifer L. Braid§*, Laura S. Bruckman*, Roger H. French*
*SDLE Research Center, Department of Materials Science and Engineering, Case Western Reserve University (CWRU),
Cleveland, OH, 44106, USA
†System Technology & Reliability Testing, Canadian Solar Inc. (CSI), Suzhou, Jiangsu, 215129, China
‡Cybrid Technologies Inc., Suzhou, Jiangsu, China
§Sandia National Laboratories, Albuquerque, NM, USA

***Abstract*—Network structural equation modeling has been used for degradation modeling of glass/backsheet (GB) and double glass (DG) PERC PV minimodules, made by CSI and CWRU. The encapsulants used were ethylene vinyl acetate (EVA) and polyolefin elastomer (POE). The exposures included modified damp heat (80°C and 85% relative humidity), with and without full spectrum light. Each exposure cycle consists of 2520 hours, 5 steps of 504 hours each. The data from I-V and $Suns$-V_{oc} was used in the analysis. We observe that most DG minimodules exhibit stability in power with exposure time and GB minimodules by CWRU showed a power loss of 5-6% on average due to corrosion.**

***Index Terms*—network structural equation modeling, accelerated exposures, PV degradation, electrical measurements**

I. Introduction

The PV industry is rapidly growing in the renewable energy sector with a global PV capacity of 512 GW in 2019 [1]. Valued at $135 billion in 2019 and with an annual PV the complexity of PV system behavior in external conditions. As degradation modes take place simultaneously during exposure conditions, it is important to understand how multiple modes affect the performance of PV minimodules. Using network structural equation modeling (netSEM) developed at the SDLE Research Center, stressor(s) (S), mechanistic variables (M_i) and responses (R) can be mapped to study dominant mechanisms and the degradation pathways [4]–[6]. netSEM enables the quantitative study of variables through statistical measures and mathematical equations using linear/non-linear models. The advantages of the netSEM approach is that the dominant mechanisms causing degradation can be identified, and sequential/parallel degradation pathways can be explored in a system [4], [7]. netSEM is a semi-supervised method: by making use of domain knowledge, variable selection is done in order to obtain the models [7].

There are two principles that govern netSEM analysis:

Figure 48: A conference proceeding article in PVSC 49th.

- Representative Modules for Accelerated Thermal Cycling and Static Load Testing, conference proceeding, PVSC 48th 49

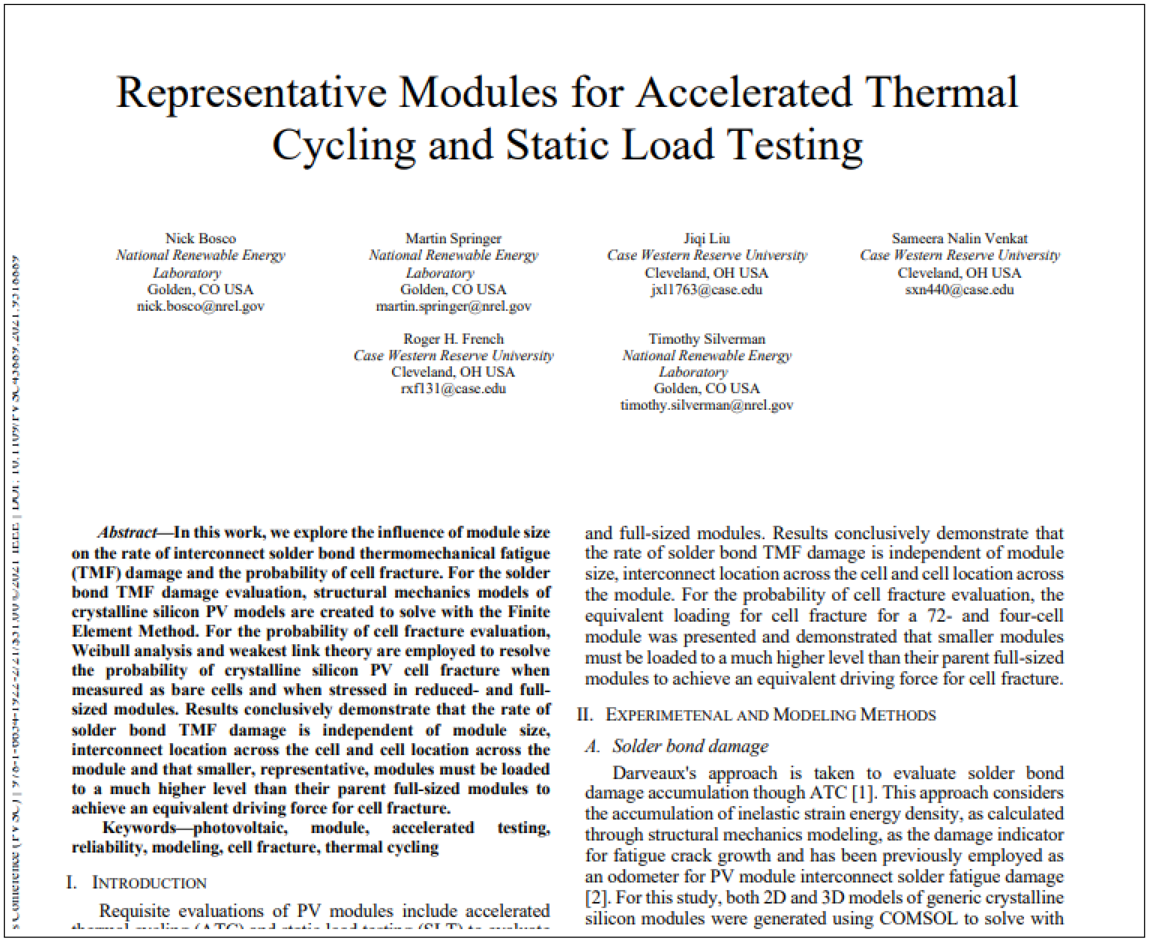

Representative Modules for Accelerated Thermal Cycling and Static Load Testing

Nick Bosco
National Renewable Energy Laboratory
Golden, CO USA
nick.bosco@nrel.gov

Martin Springer
National Renewable Energy Laboratory
Golden, CO USA
martin.springer@nrel.gov

Jiqi Liu
Case Western Reserve University
Cleveland, OH USA
jxl1763@case.edu

Sameera Nalin Venkat
Case Western Reserve University
Cleveland, OH USA
sxn440@case.edu

Roger H. French
Case Western Reserve University
Cleveland, OH USA
rxf131@case.edu

Timothy Silverman
National Renewable Energy Laboratory
Golden, CO USA
timothy.silverman@nrel.gov

***Abstract*—In this work, we explore the influence of module size on the rate of interconnect solder bond thermomechanical fatigue (TMF) damage and the probability of cell fracture. For the solder bond TMF damage evaluation, structural mechanics models of crystalline silicon PV models are created to solve with the Finite Element Method. For the probability of cell fracture evaluation, Weibull analysis and weakest link theory are employed to resolve the probability of crystalline silicon PV cell fracture when measured as bare cells and when stressed in reduced- and full-sized modules. Results conclusively demonstrate that the rate of solder bond TMF damage is independent of module size, interconnect location across the cell and cell location across the module and that smaller, representative, modules must be loaded to a much higher level than their parent full-sized modules to achieve an equivalent driving force for cell fracture.**

Keywords—photovoltaic, module, accelerated testing, reliability, modeling, cell fracture, thermal cycling

I. INTRODUCTION

Requisite evaluations of PV modules include accelerated

and full-sized modules. Results conclusively demonstrate that the rate of solder bond TMF damage is independent of module size, interconnect location across the cell and cell location across the module. For the probability of cell fracture evaluation, the equivalent loading for cell fracture for a 72- and four-cell module was presented and demonstrated that smaller modules must be loaded to a much higher level than their parent full-sized modules to achieve an equivalent driving force for cell fracture.

II. EXPERIMETENAL AND MODELING METHODS

A. Solder bond damage

Darveaux's approach is taken to evaluate solder bond damage accumulation though ATC [1]. This approach considers the accumulation of inelastic strain energy density, as calculated through structural mechanics modeling, as the damage indicator for fatigue crack growth and has been previously employed as an odometer for PV module interconnect solder fatigue damage [2]. For this study, both 2D and 3D models of generic crystalline silicon modules were generated using COMSOL to solve with

Figure 49: A conference proceeding article in PVSC 47th.

- Employing Fracture Statistics to Track Cell Reliability Through Module Fabrication, peer-reviewed journal, IEEE JPV. 50.

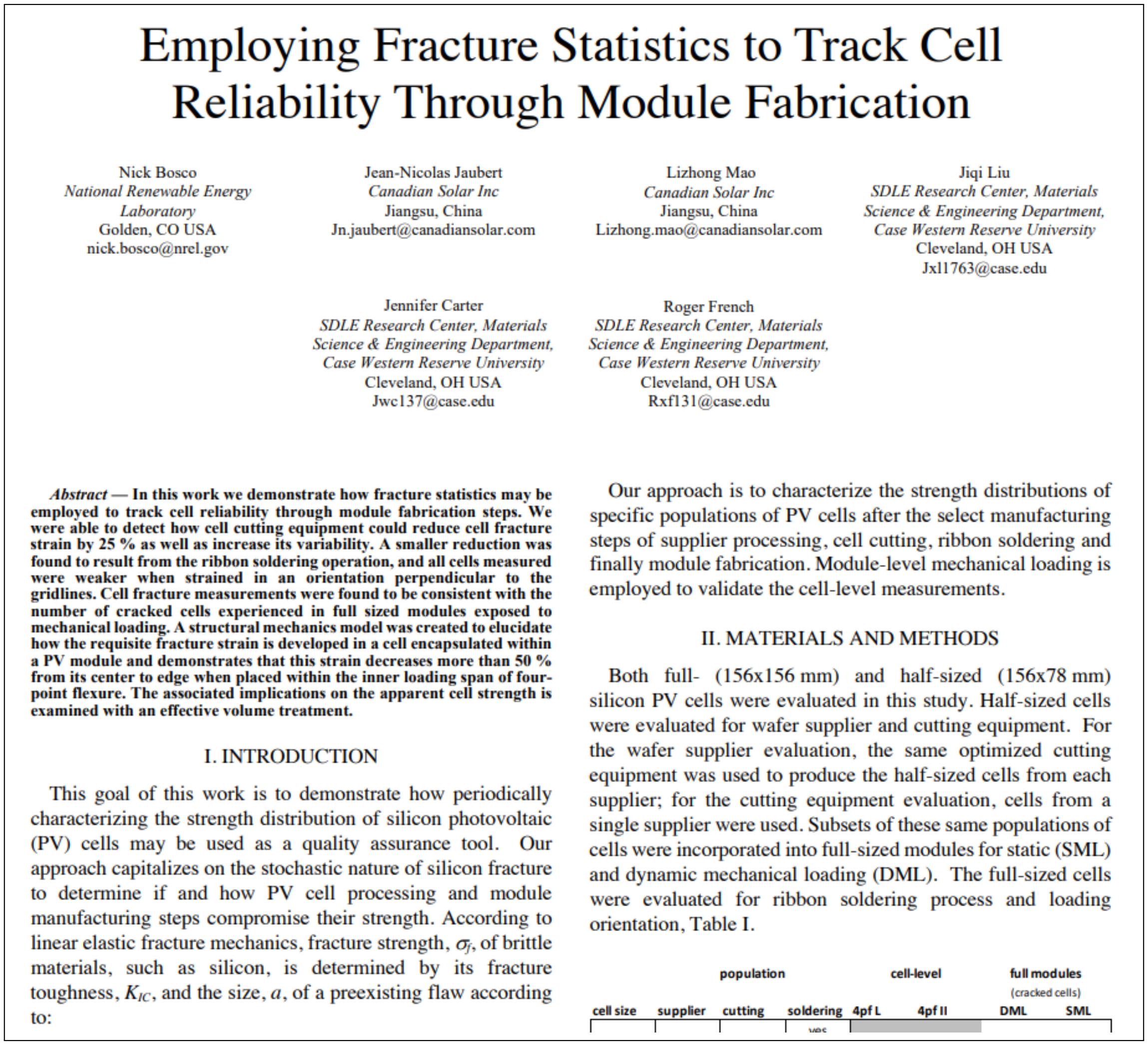

Employing Fracture Statistics to Track Cell Reliability Through Module Fabrication

Nick Bosco
National Renewable Energy Laboratory
Golden, CO USA
nick.bosco@nrel.gov

Jean-Nicolas Jaubert
Canadian Solar Inc
Jiangsu, China
Jn.jaubert@canadiansolar.com

Lizhong Mao
Canadian Solar Inc
Jiangsu, China
Lizhong.mao@canadiansolar.com

Jiqi Liu
SDLE Research Center, Materials Science & Engineering Department, Case Western Reserve University
Cleveland, OH USA
Jxl1763@case.edu

Jennifer Carter
SDLE Research Center, Materials Science & Engineering Department, Case Western Reserve University
Cleveland, OH USA
Jwc137@case.edu

Roger French
SDLE Research Center, Materials Science & Engineering Department, Case Western Reserve University
Cleveland, OH USA
Rxf131@case.edu

***Abstract* — In this work we demonstrate how fracture statistics may be employed to track cell reliability through module fabrication steps. We were able to detect how cell cutting equipment could reduce cell fracture strain by 25 % as well as increase its variability. A smaller reduction was found to result from the ribbon soldering operation, and all cells measured were weaker when strained in an orientation perpendicular to the gridlines. Cell fracture measurements were found to be consistent with the number of cracked cells experienced in full sized modules exposed to mechanical loading. A structural mechanics model was created to elucidate how the requisite fracture strain is developed in a cell encapsulated within a PV module and demonstrates that this strain decreases more than 50 % from its center to edge when placed within the inner loading span of four-point flexure. The associated implications on the apparent cell strength is examined with an effective volume treatment.**

I. INTRODUCTION

This goal of this work is to demonstrate how periodically characterizing the strength distribution of silicon photovoltaic (PV) cells may be used as a quality assurance tool. Our approach capitalizes on the stochastic nature of silicon fracture to determine if and how PV cell processing and module manufacturing steps compromise their strength. According to linear elastic fracture mechanics, fracture strength, σ_f, of brittle materials, such as silicon, is determined by its fracture toughness, K_{IC}, and the size, a, of a preexisting flaw according to:

Our approach is to characterize the strength distributions of specific populations of PV cells after the select manufacturing steps of supplier processing, cell cutting, ribbon soldering and finally module fabrication. Module-level mechanical loading is employed to validate the cell-level measurements.

II. MATERIALS AND METHODS

Both full- (156x156 mm) and half-sized (156x78 mm) silicon PV cells were evaluated in this study. Half-sized cells were evaluated for wafer supplier and cutting equipment. For the wafer supplier evaluation, the same optimized cutting equipment was used to produce the half-sized cells from each supplier; for the cutting equipment evaluation, cells from a single supplier were used. Subsets of these same populations of cells were incorporated into full-sized modules for static (SML) and dynamic mechanical loading (DML). The full-sized cells were evaluated for ribbon soldering process and loading orientation, Table I.

population				cell-level		full modules (cracked cells)	
cell size	supplier	cutting	soldering	4pf L	4pf II	DML	SML

Figure 50: Peer Review Journal Accepted.

- Degradation Mechanisms and Partial Shading of Glass-backsheet and Double Glass Photovoltaic Modules in Three Climate Zones Determined by Remote Monitoring of Time-series Current-voltage and Power Datastreams, peer-reviewed journal, Solar Energy. 51.

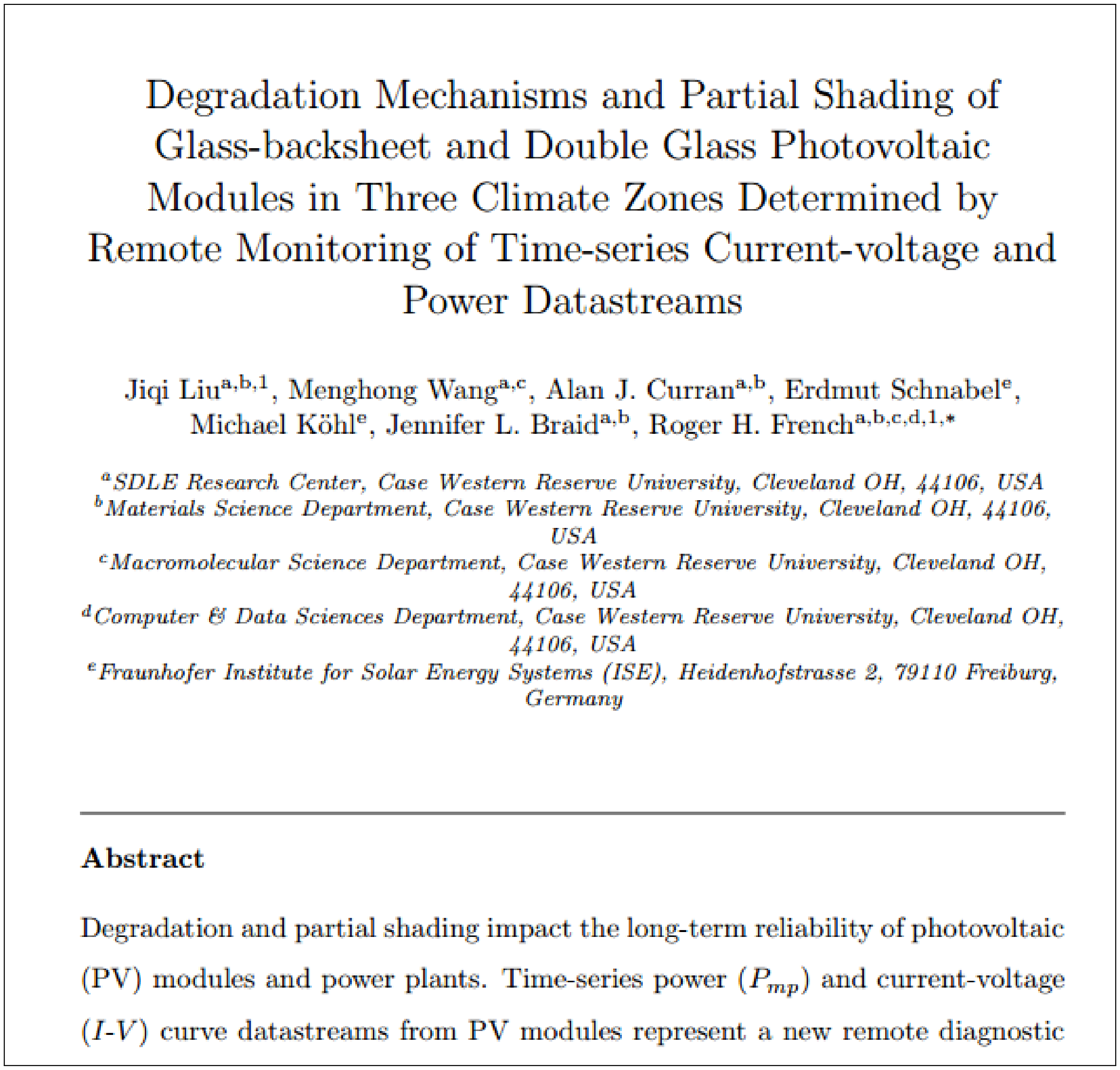

Degradation Mechanisms and Partial Shading of Glass-backsheet and Double Glass Photovoltaic Modules in Three Climate Zones Determined by Remote Monitoring of Time-series Current-voltage and Power Datastreams

Jiqi Liu[a,b,1], Menghong Wang[a,c], Alan J. Curran[a,b], Erdmut Schnabel[e], Michael Köhl[e], Jennifer L. Braid[a,b], Roger H. French[a,b,c,d,1,*]

[a]SDLE Research Center, Case Western Reserve University, Cleveland OH, 44106, USA
[b]Materials Science Department, Case Western Reserve University, Cleveland OH, 44106, USA
[c]Macromolecular Science Department, Case Western Reserve University, Cleveland OH, 44106, USA
[d]Computer & Data Sciences Department, Case Western Reserve University, Cleveland OH, 44106, USA
[e]Fraunhofer Institute for Solar Energy Systems (ISE), Heidenhofstrasse 2, 79110 Freiburg, Germany

---

Abstract

Degradation and partial shading impact the long-term reliability of photovoltaic (PV) modules and power plants. Time-series power (P_{mp}) and current-voltage (I-V) curve datastreams from PV modules represent a new remote diagnostic

Figure 51: Peer Review Journal Submitted.

- Mechanistic Insights to Degradation of PERC Minimodules with Differentiated Packaging Materials & Module Architectures, conference proceeding, PVSC 46th, Chicago, IN. 52.

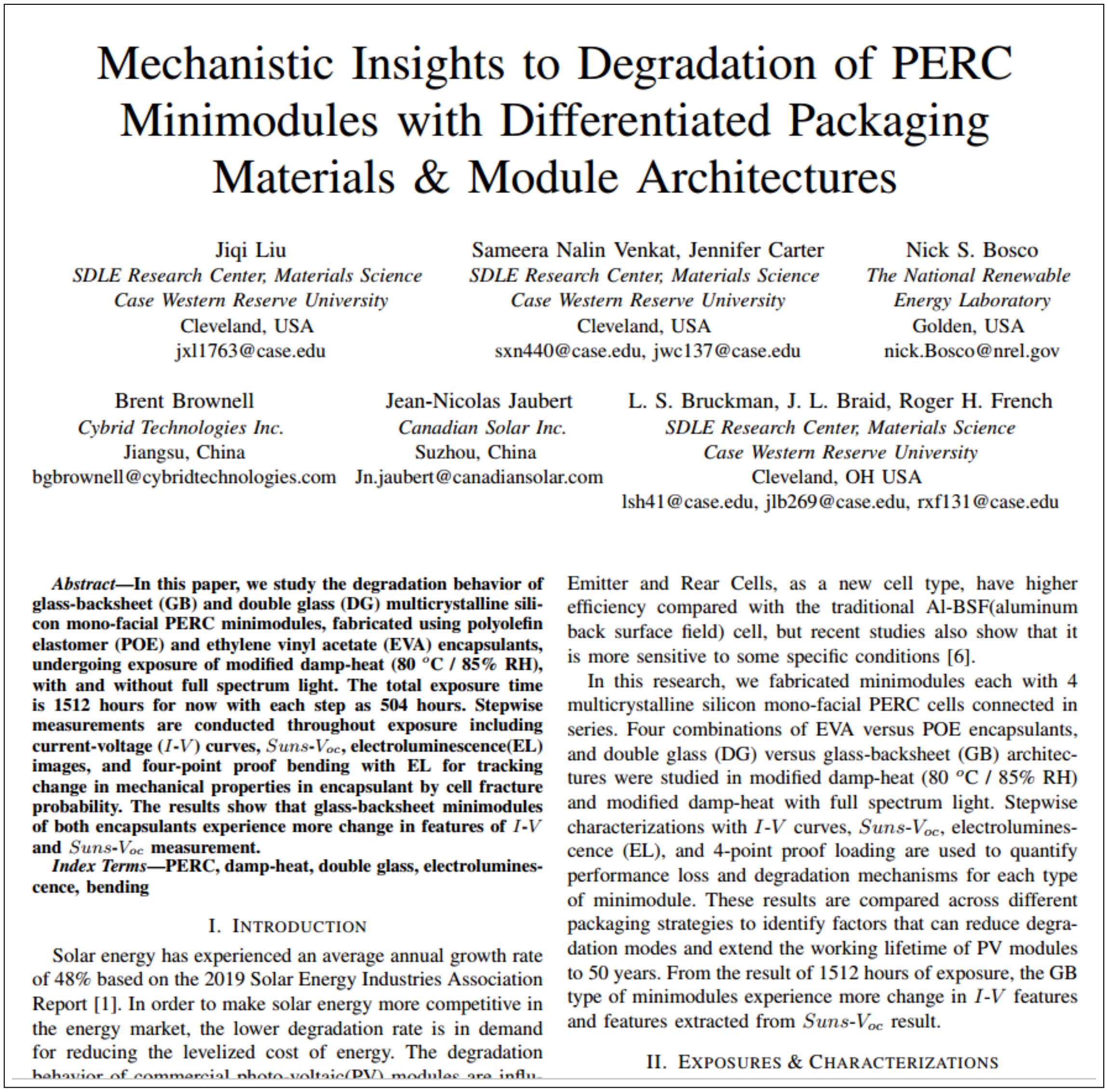

Mechanistic Insights to Degradation of PERC Minimodules with Differentiated Packaging Materials & Module Architectures

Jiqi Liu
SDLE Research Center, Materials Science
Case Western Reserve University
Cleveland, USA
jxl1763@case.edu

Sameera Nalin Venkat, Jennifer Carter
SDLE Research Center, Materials Science
Case Western Reserve University
Cleveland, USA
sxn440@case.edu, jwc137@case.edu

Nick S. Bosco
The National Renewable Energy Laboratory
Golden, USA
nick.Bosco@nrel.gov

Brent Brownell
Cybrid Technologies Inc.
Jiangsu, China
bgbrownell@cybridtechnologies.com

Jean-Nicolas Jaubert
Canadian Solar Inc.
Suzhou, China
Jn.jaubert@canadiansolar.com

L. S. Bruckman, J. L. Braid, Roger H. French
SDLE Research Center, Materials Science
Case Western Reserve University
Cleveland, OH USA
lsh41@case.edu, jlb269@case.edu, rxf131@case.edu

***Abstract*—In this paper, we study the degradation behavior of glass-backsheet (GB) and double glass (DG) multicrystalline silicon mono-facial PERC minimodules, fabricated using polyolefin elastomer (POE) and ethylene vinyl acetate (EVA) encapsulants, undergoing exposure of modified damp-heat (80 ^oC / 85% RH), with and without full spectrum light. The total exposure time is 1512 hours for now with each step as 504 hours. Stepwise measurements are conducted throughout exposure including current-voltage (I-V) curves, $Suns$-V_{oc}, electroluminescence(EL) images, and four-point proof bending with EL for tracking change in mechanical properties in encapsulant by cell fracture probability. The results show that glass-backsheet minimodules of both encapsulants experience more change in features of I-V and $Suns$-V_{oc} measurement.**

***Index Terms*—PERC, damp-heat, double glass, electroluminescence, bending**

I. INTRODUCTION

Solar energy has experienced an average annual growth rate of 48% based on the 2019 Solar Energy Industries Association Report [1]. In order to make solar energy more competitive in the energy market, the lower degradation rate is in demand for reducing the levelized cost of energy. The degradation behavior of commercial photo-voltaic(PV) modules are influ-

Emitter and Rear Cells, as a new cell type, have higher efficiency compared with the traditional Al-BSF(aluminum back surface field) cell, but recent studies also show that it is more sensitive to some specific conditions [6].

In this research, we fabricated minimodules each with 4 multicrystalline silicon mono-facial PERC cells connected in series. Four combinations of EVA versus POE encapsulants, and double glass (DG) versus glass-backsheet (GB) architectures were studied in modified damp-heat (80 ^oC / 85% RH) and modified damp-heat with full spectrum light. Stepwise characterizations with I-V curves, $Suns$-V_{oc}, electroluminescence (EL), and 4-point proof loading are used to quantify performance loss and degradation mechanisms for each type of minimodule. These results are compared across different packaging strategies to identify factors that can reduce degradation modes and extend the working lifetime of PV modules to 50 years. From the result of 1512 hours of exposure, the GB type of minimodules experience more change in I-V features and features extracted from $Suns$-V_{oc} result.

II. EXPOSURES & CHARACTERIZATIONS

Figure 52: Conference proceeding in PVSC 46th.

- Employing Fracture Statistics to Track Cell Reliability Through Module Fabrication, conference proceeding, PVSC 46th, Chicago, IN. 53.

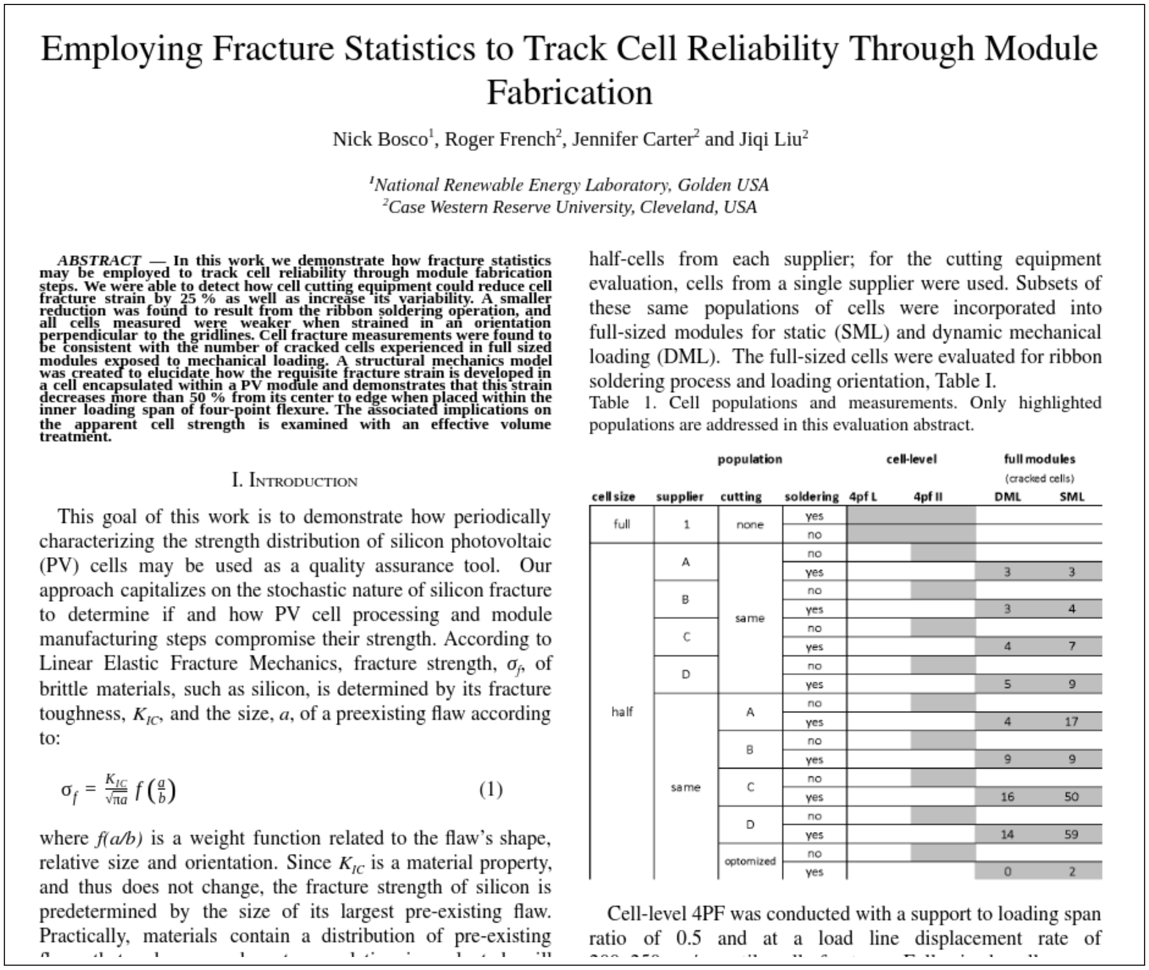

Employing Fracture Statistics to Track Cell Reliability Through Module Fabrication

Nick Bosco[1], Roger French[2], Jennifer Carter[2] and Jiqi Liu[2]

[1]*National Renewable Energy Laboratory, Golden USA*
[2]*Case Western Reserve University, Cleveland, USA*

***ABSTRACT* — In this work we demonstrate how fracture statistics may be employed to track cell reliability through module fabrication steps. We were able to detect how cell cutting equipment could reduce cell fracture strain by 25 % as well as increase its variability. A smaller reduction was found to result from the ribbon soldering operation, and all cells measured were weaker when strained in an orientation perpendicular to the gridlines. Cell fracture measurements were found to be consistent with the number of cracked cells experienced in full sized modules exposed to mechanical loading. A structural mechanics model was created to elucidate how the requisite fracture strain is developed in a cell encapsulated within a PV module and demonstrates that this strain decreases more than 50 % from its center to edge when placed within the inner loading span of four-point flexure. The associated implications on the apparent cell strength is examined with an effective volume treatment.**

I. Introduction

This goal of this work is to demonstrate how periodically characterizing the strength distribution of silicon photovoltaic (PV) cells may be used as a quality assurance tool. Our approach capitalizes on the stochastic nature of silicon fracture to determine if and how PV cell processing and module manufacturing steps compromise their strength. According to Linear Elastic Fracture Mechanics, fracture strength, σ_f, of brittle materials, such as silicon, is determined by its fracture toughness, K_{IC}, and the size, a, of a preexisting flaw according to:

$$\sigma_f = \frac{K_{IC}}{\sqrt{\pi a}} f\left(\frac{a}{b}\right) \quad (1)$$

where *f(a/b)* is a weight function related to the flaw's shape, relative size and orientation. Since K_{IC} is a material property, and thus does not change, the fracture strength of silicon is predetermined by the size of its largest pre-existing flaw. Practically, materials contain a distribution of pre-existing

half-cells from each supplier; for the cutting equipment evaluation, cells from a single supplier were used. Subsets of these same populations of cells were incorporated into full-sized modules for static (SML) and dynamic mechanical loading (DML). The full-sized cells were evaluated for ribbon soldering process and loading orientation, Table I.

Table 1. Cell populations and measurements. Only highlighted populations are addressed in this evaluation abstract.

population				cell-level		full modules (cracked cells)	
cell size	supplier	cutting	soldering	4pf L	4pf II	DML	SML
full	1	none	yes	▨	▨		
			no	▨	▨		
half	A	same	no		▨		
			yes			3	3
	B		no		▨		
			yes			3	4
	C		no		▨		
			yes			4	7
	D		no		▨		
			yes			5	9
	same	A	no		▨		
			yes			4	17
		B	no		▨		
			yes			9	9
		C	no		▨		
			yes			16	50
		D	no		▨		
			yes			14	59
		optomized	no		▨		
			yes			0	2

Cell-level 4PF was conducted with a support to loading span ratio of 0.5 and at a load line displacement rate of

Figure 53: Conference proceeding in PVSC 46th.

- Towards 50 Year Module Lifetimes: Impact of Module Architecture and Packaging Materials, NREL workshop in Lakewood CO, 2020 54.

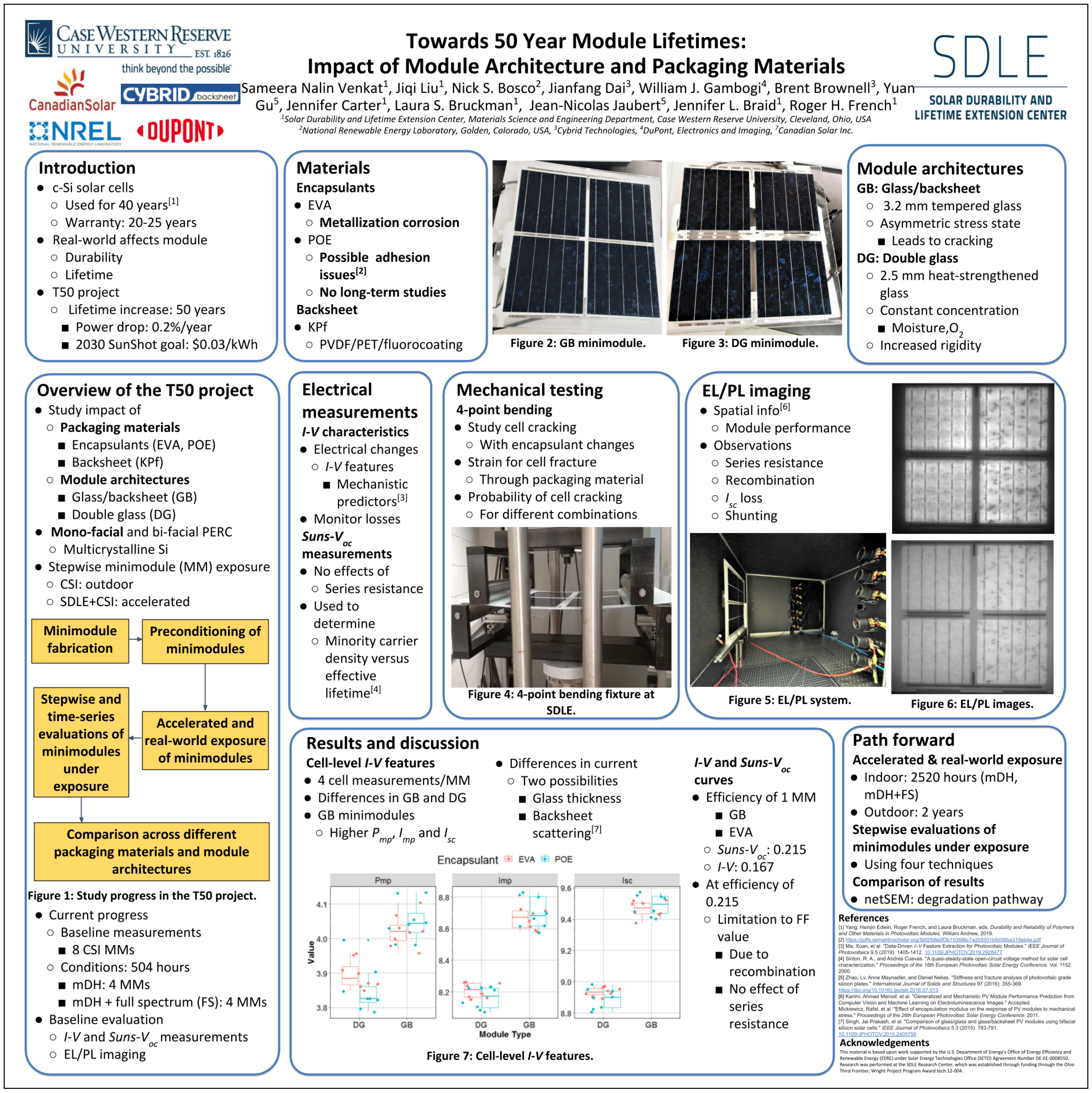

Towards 50 Year Module Lifetimes: Impact of Module Architecture and Packaging Materials

Sameera Nalin Venkat[1], Jiqi Liu[1], Nick S. Bosco[2], Jianfang Dai[3], William J. Gambogi[4], Brent Brownell[3], Yuan Gu[5], Jennifer Carter[1], Laura S. Bruckman[1], Jean-Nicolas Jaubert[5], Jennifer L. Braid[1], Roger H. French[1]
[1]Solar Durability and Lifetime Extension Center, Materials Science and Engineering Department, Case Western Reserve University, Cleveland, Ohio, USA
[2]National Renewable Energy Laboratory, Golden, Colorado, USA, [3]Cybrid Technologies, [4]DuPont, Electronics and Imaging, [7]Canadian Solar Inc.

Introduction

- c-Si solar cells
  - Used for 40 years[1]
  - Warranty: 20-25 years
- Real-world affects module
  - Durability
  - Lifetime
- T50 project
  - Lifetime increase: 50 years
    - Power drop: 0.2%/year
    - 2030 SunShot goal: $0.03/kWh

Materials

Encapsulants
- EVA
  - **Metallization corrosion**
- POE
  - **Possible adhesion issues[2]**
  - **No long-term studies**

Backsheet
- KPf
  - PVDF/PET/fluorocoating

Figure 2: GB minimodule.

Figure 3: DG minimodule.

Module architectures

GB: Glass/backsheet
- 3.2 mm tempered glass
- Asymmetric stress state
  - Leads to cracking

DG: Double glass
- 2.5 mm heat-strengthened glass
- Constant concentration
  - Moisture,O_2
- Increased rigidity

Overview of the T50 project

- Study impact of
  - **Packaging materials**
    - Encapsulants (EVA, POE)
    - Backsheet (KPf)
  - **Module architectures**
    - Glass/backsheet (GB)
    - Double glass (DG)
- **Mono-facial** and bi-facial PERC
  - Multicrystalline Si
- Stepwise minimodule (MM) exposure
  - CSI: outdoor
  - SDLE+CSI: accelerated

Figure 1: Study progress in the T50 project.

- Current progress
  - Baseline measurements
    - 8 CSI MMs
  - Conditions: 504 hours
    - mDH: 4 MMs
    - mDH + full spectrum (FS): 4 MMs
- Baseline evaluation
  - *I-V* and *Suns-*V_{oc} measurements
  - EL/PL imaging

Electrical measurements

***I-V* characteristics**
- Electrical changes
  - *I-V* features
    - Mechanistic predictors[3]
- Monitor losses

***Suns-*V_{oc} measurements**
- No effects of
  - Series resistance
- Used to determine
  - Minority carrier density versus effective lifetime[4]

Mechanical testing

4-point bending
- Study cell cracking
  - With encapsulant changes
- Strain for cell fracture
  - Through packaging material
- Probability of cell cracking
  - For different combinations

Figure 4: 4-point bending fixture at SDLE.

EL/PL imaging

- Spatial info[6]
  - Module performance
- Observations
  - Series resistance
  - Recombination
  - I_{sc} loss
  - Shunting

Figure 5: EL/PL system.

Figure 6: EL/PL images.

Results and discussion

Cell-level *I-V* features
- 4 cell measurements/MM
- Differences in GB and DG
- GB minimodules
  - Higher P_{mp}, I_{mp} and I_{sc}
- Differences in current
  - Two possibilities
    - Glass thickness
    - Backsheet scattering[7]

Figure 7: Cell-level *I-V* features.

***I-V* and *Suns-*V_{oc} curves**
- Efficiency of 1 MM
  - GB
  - EVA
  - *Suns-*V_{oc}: 0.215
  - *I-V*: 0.167
- At efficiency of 0.215
  - Limitation to FF value
    - Due to recombination
    - No effect of series resistance

Path forward

Accelerated & real-world exposure
- Indoor: 2520 hours (mDH, mDH+FS)
- Outdoor: 2 years

Stepwise evaluations of minimodules under exposure
- Using four techniques

Comparison of results
- netSEM: degradation pathway

References

[1] Yang, Hsinjin Edwin, Roger French, and Laura Bruckman, eds. *Durability and Reliability of Polymers and Other Materials in Photovoltaic Modules*. William Andrew, 2019.
[2] https://pdfs.semanticscholar.org/5bf2/b8e0f3b110596c7a2b5501b9d36ba315eb4e.pdf
[3] Ma, Xuan, et al. "Data-Driven *I–V* Feature Extraction for Photovoltaic Modules." *IEEE Journal of Photovoltaics* 9.5 (2019): 1405-1412. 10.1109/JPHOTOV.2019.2928477
[4] Sinton, R. A., and Andres Cuevas. "A quasi-steady-state open-circuit voltage method for solar cell characterization." *Proceedings of the 16th European Photovoltaic Solar Energy Conference*. Vol. 1152. 2000.
[5] Zhao, Lv, Anne Maynadier, and Daniel Nelias. "Stiffness and fracture analysis of photovoltaic grade silicon plates." *International Journal of Solids and Structures* 97 (2016): 355-369. https://doi.org/10.1016/j.ijsolstr.2016.07.013
[6] Karimi, Ahmad Maroof, et al. "Generalized and Mechanistic PV Module Performance Prediction from Computer Vision and Machine Learning on Electroluminescence Images." Accepted.
Mickiewicz, Rafal, et al. "Effect of encapsulation modulus on the response of PV modules to mechanical stress." *Proceedings of the 26th European Photovoltaic Solar Energy Conference*. 2011.
[7] Singh, Jai Prakash, et al. "Comparison of glass/glass and glass/backsheet PV modules using bifacial silicon solar cells." *IEEE Journal of Photovoltaics* 5.3 (2015): 783-791. 10.1109/JPHOTOV.2015.2405756

Acknowledgements

This material is based upon work supported by the U.S. Department of Energy's Office of Energy Efficiency and Renewable Energy (EERE) under Solar Energy Technologies Office (SETO) Agreement Number DE-EE-0008550. Research was performed at the SDLE Research Center, which was established through funding through the Ohio Third Frontier, Wright Project Program Award tech 12-004.

Figure 54: Towards 50 Year Module Lifetimes: Impact of Module Architecture and Packaging Materials, NREL workshop in Golden, CO, 2020.

- Impact of packing materials and module architectures for PERC bi- and mono- facial modules: Towards 50 year module lifetimes, in Lakewood CO, 2020 55.

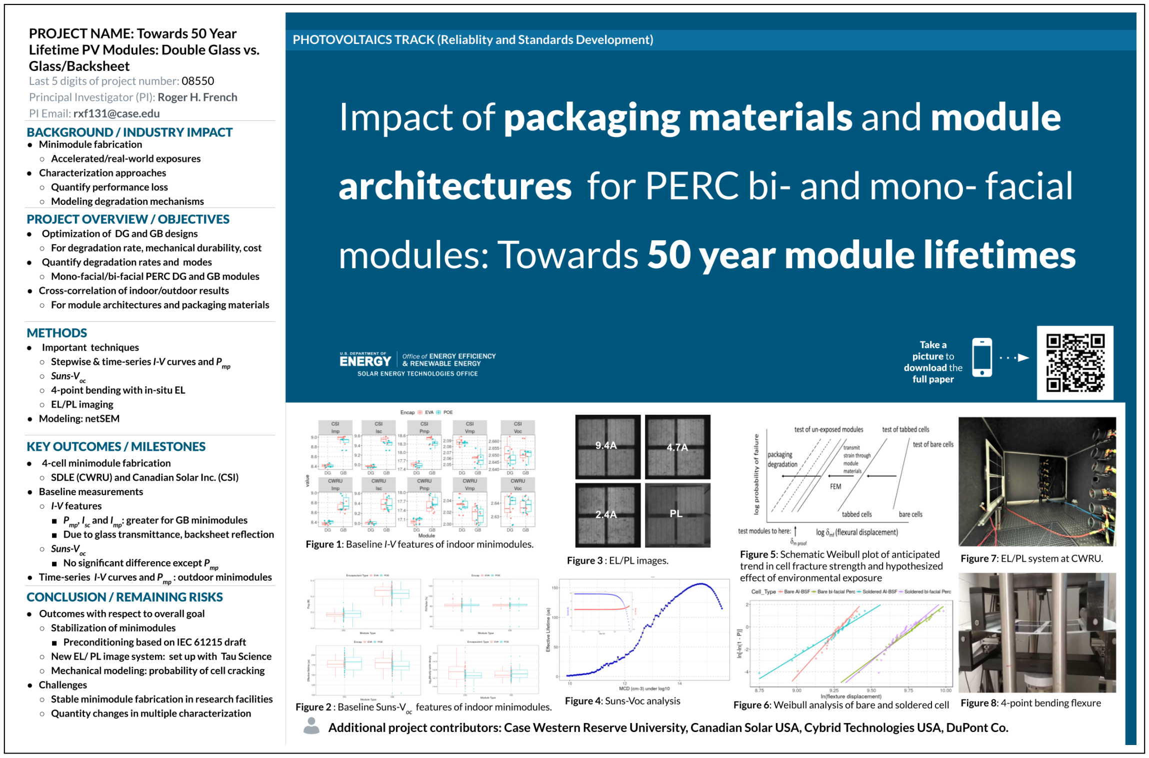

PROJECT NAME: Towards 50 Year Lifetime PV Modules: Double Glass vs. Glass/Backsheet

Last 5 digits of project number: 08550
Principal Investigator (PI): **Roger H. French**
PI Email: **rxf131@case.edu**

BACKGROUND / INDUSTRY IMPACT

- Minimodule fabrication
    - Accelerated/real-world exposures
- Characterization approaches
    - Quantify performance loss
    - Modeling degradation mechanisms

PROJECT OVERVIEW / OBJECTIVES

- Optimization of DG and GB designs
    - For degradation rate, mechanical durability, cost
- Quantify degradation rates and modes
    - Mono-facial/bi-facial PERC DG and GB modules
- Cross-correlation of indoor/outdoor results
    - For module architectures and packaging materials

METHODS

- Important techniques
    - Stepwise & time-series *I-V* curves and P_{mp}
    - *Suns*-V_{oc}
    - 4-point bending with in-situ EL
    - EL/PL imaging
- Modeling: netSEM

KEY OUTCOMES / MILESTONES

- 4-cell minimodule fabrication
    - SDLE (CWRU) and Canadian Solar Inc. (CSI)
- Baseline measurements
    - *I-V* features
        - P_{mp}, I_{sc} and I_{mp}: greater for GB minimodules
        - Due to glass transmittance, backsheet reflection
    - *Suns*-V_{oc}
        - No significant difference except P_{mp}
- Time-series *I-V* curves and P_{mp} : outdoor minimodules

CONCLUSION / REMAINING RISKS

- Outcomes with respect to overall goal
    - Stabilization of minimodules
        - Preconditioning based on IEC 61215 draft
    - New EL/ PL image system: set up with Tau Science
    - Mechanical modeling: probability of cell cracking
- Challenges
    - Stable minimodule fabrication in research facilities
    - Quantity changes in multiple characterization

PHOTOVOLTAICS TRACK (Reliablity and Standards Development)

Impact of **packaging materials** and **module architectures** for PERC bi- and mono- facial modules: Towards **50 year module lifetimes**

U.S. DEPARTMENT OF ENERGY | Office of ENERGY EFFICIENCY & RENEWABLE ENERGY
SOLAR ENERGY TECHNOLOGIES OFFICE

Take a picture to **download** the **full paper**

Figure 1: Baseline *I-V* features of indoor minimodules.

Figure 3 : EL/PL images.

Figure 5: Schematic Weibull plot of anticipated trend in cell fracture strength and hypothesized effect of environmental exposure

Figure 7: EL/PL system at CWRU.

Figure 2 : Baseline Suns-V_{oc} features of indoor minimodules.

Figure 4: Suns-Voc analysis

Figure 6: Weibull analysis of bare and soldered cell

Figure 8: 4-point bending flexure

Additional project contributors: Case Western Reserve University, Canadian Solar USA, Cybrid Technologies USA, DuPont Co.

Figure 55: Impact of packaging materials and module architectures for PERC bi- and mono- facial modules: Towards 50 year module lifetimes, SETO Poster Presentation Denver CO, February 2020.

- Towards 50 Year Modules, SETO Poster Presentation at the 46th PVSC meeting in Chicago, 201956.

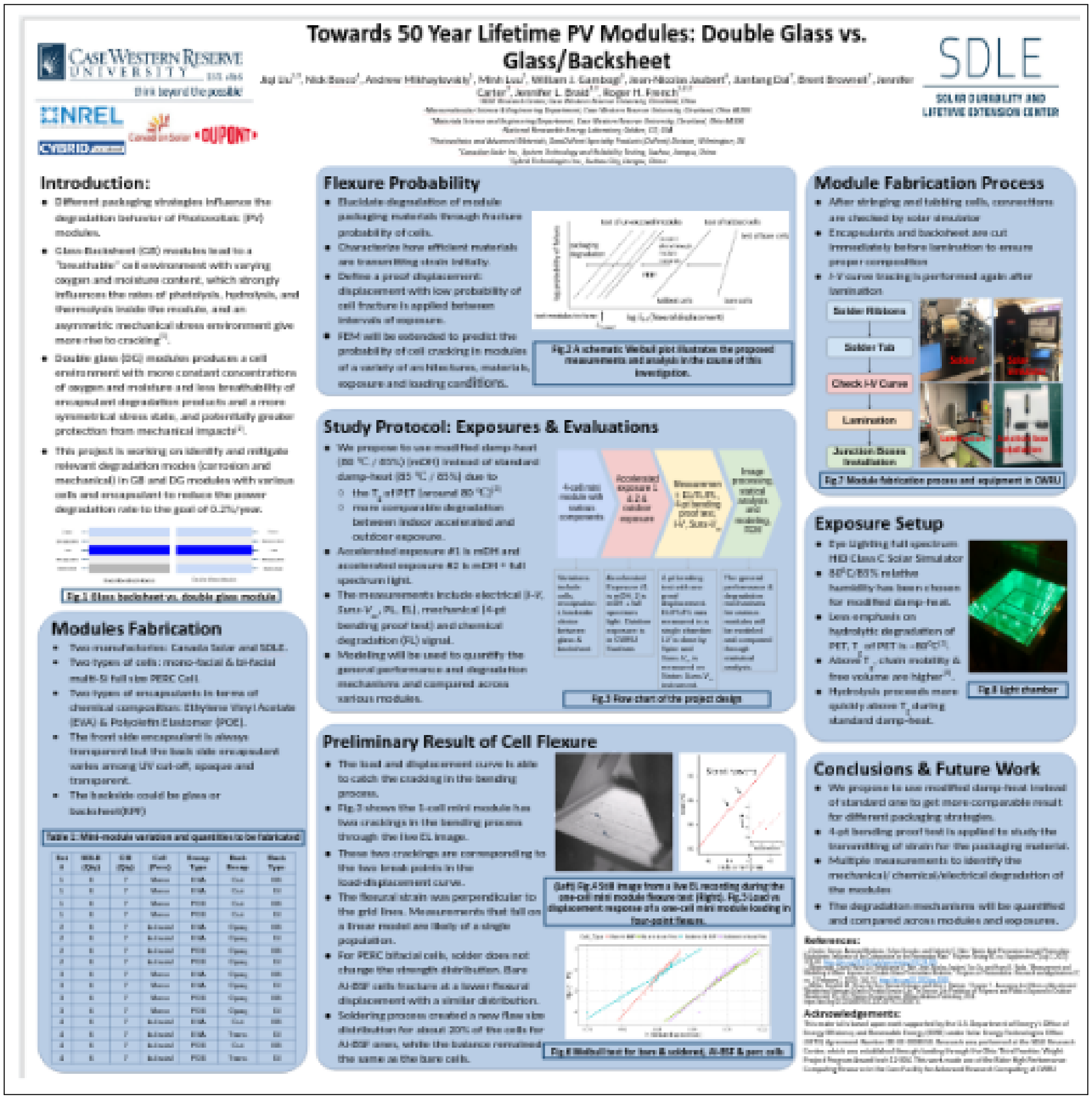

Towards 50 Year Lifetime PV Modules: Double Glass vs. Glass/Backsheet

Introduction:

Flexure Probability

Module Fabrication Process

Study Protocol: Exposures & Evaluations

Exposure Setup

Modules Fabrication

Preliminary Result of Cell Flexure

Conclusions & Future Work

Figure 56: Towards 50 Year Modules, SETO Poster Presentation at the 46th PVSC meeting in Chicago, 2019.

- Towards 50 Year Lifetime PV Modules: Double Glass vs. Glass/Backsheet, 6th Annual Data Science Symposium in CWRU, 2019 57.

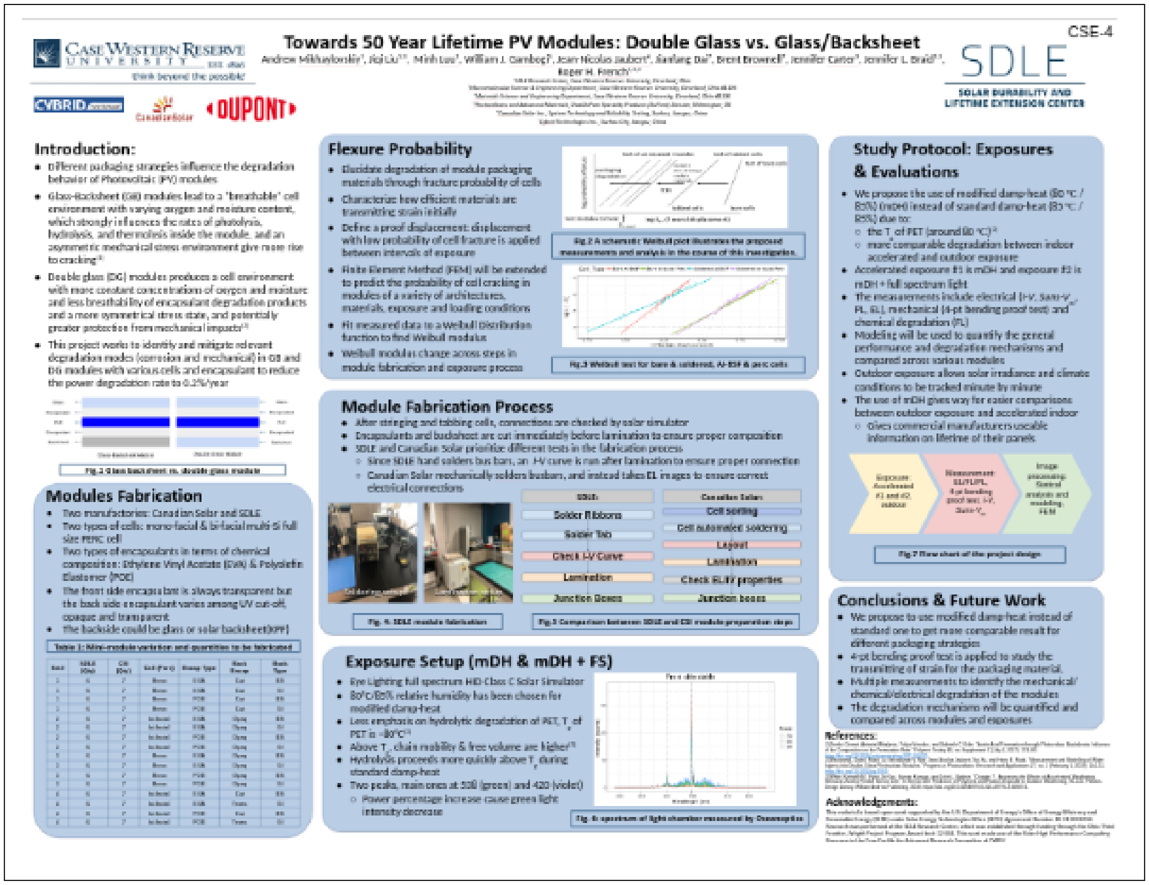

CSE-4

Towards 50 Year Lifetime PV Modules: Double Glass vs. Glass/Backsheet

Andrew Mikhaylovskiy[1], Jiqi Liu[1,2], Minh Luu[1], William J. Gambogi[3], Jean Nicolas Jaubert[4], Jianfang Dai[4], Brent Brownell[5], Jennifer Carter[2], Jennifer L. Braid[1,2], Roger H. French[1,2]

Introduction:

- Different packaging strategies influence the degradation behavior of Photovoltaic (PV) modules
- Glass-Backsheet (GB) modules lead to a "breathable" cell environment with varying oxygen and moisture content, which strongly influences the rates of photolysis, hydrolysis, and thermolysis inside the module, and an asymmetric mechanical stress environment give more rise to cracking[1]
- Double glass (DG) modules produces a cell environment with more constant concentrations of oxygen and moisture and less breathability of encapsulant degradation products and a more symmetrical stress state, and potentially greater protection from mechanical impacts[2]
- This project works to identify and mitigate relevant degradation modes (corrosion and mechanical) in GB and DG modules with various cells and encapsulant to reduce the power degradation rate to 0.2%/year

Fig.1 Glass backsheet vs. double glass module

Modules Fabrication

- Two manufactories: Canadian Solar and SDLE
- Two types of cells: mono-facial & bi-facial multi-Si full size PERC cell
- Two types of encapsulants in terms of chemical composition: Ethylene Vinyl Acetate (EVA) & Polyolefin Elastomer (POE)
- The front side encapsulant is always transparent but the back side encapsulant varies among UV cut-off, opaque and transparent
- The backside could be glass or solar backsheet(KPF)

Table 1: Mini-module variation and quantities to be fabricated

Flexure Probability

- Elucidate degradation of module packaging materials through fracture probability of cells
- Characterize how efficient materials are transmitting strain initially
- Define a proof displacement: displacement with low probability of cell fracture is applied between intervals of exposure
- Finite Element Method (FEM) will be extended to predict the probability of cell cracking in modules of a variety of architectures, materials, exposure and loading conditions
- Fit measured data to a Weibull Distribution function to find Weibull modulus
- Weibull modulus change across steps in module fabrication and exposure process

Fig.2 A schematic Weibull plot illustrates the proposed measurements and analysis in the course of this investigation.

Fig.3 Weibull test for bare & soldered, Al-BSF & perc cells

Module Fabrication Process

- After stringing and tabbing cells, connections are checked by solar simulator
- Encapsulants and backsheet are cut immediately before lamination to ensure proper composition
- SDLE and Canadian Solar prioritize different tests in the fabrication process
  - Since SDLE hand solders bus bars, an I-V curve is run after lamination to ensure proper connection
  - Canadian Solar mechanically solders busbars, and instead takes EL images to ensure correct electrical connections

SDLE:
Solder Ribbons
Solder Tab
Check I-V Curve
Lamination
Junction Boxes

Canadian Solar:
Cell sorting
Cell automated soldering
Layout
Lamination
Check EL/IV properties
Junction boxes

Fig. 4: SDLE module fabrication

Fig.5 Comparison between SDLE and CSI module preparation steps

Exposure Setup (mDH & mDH + FS)

- Eye Lighting full spectrum HID-Class C Solar Simulator
- 80°C/85% relative humidity has been chosen for modified damp-heat
- Less emphasis on hydrolytic degradation of PET, T_g of PET is ~80°C[3]
- Above T_g, chain mobility & free volume are higher[3]
- Hydrolysis proceeds more quickly above T_g during standard damp-heat
- Two peaks, main ones at 508 (green) and 420 (violet)
  - Power percentage increase cause green light intensity decrease

Fig. 6 spectrum of light chamber measured by Oceanoptics

Study Protocol: Exposures & Evaluations

- We propose the use of modified damp-heat (80 °C / 85%) (mDH) instead of standard damp-heat (85 °C / 85%) due to:
  - the T_g of PET (around 80 °C)[3]
  - more comparable degradation between indoor accelerated and outdoor exposure
- Accelerated exposure #1 is mDH and exposure #2 is mDH + full spectrum light
- The measurements include electrical (I-V, Suns-V_{oc}, PL, EL), mechanical (4-pt bending proof test) and chemical degradation (FL)
- Modeling will be used to quantify the general performance and degradation mechanisms and compared across various modules
- Outdoor exposure allows solar irradiance and climatic conditions to be tracked minute by minute
- The use of mDH gives way for easier comparisons between outdoor exposure and accelerated indoor
  - Gives commercial manufacturers useable information on lifetime of their panels

Exposure: Accelerated #1 and #2, outdoor
Measurement: EL/FL/PL, 4-pt bending proof test, I-V, Suns-V_{oc}
Image processing, Statistical analysis and modeling, FEM

Fig.7 Flow chart of the project design

Conclusions & Future Work

- We propose to use modified damp-heat instead of standard one to get more comparable result for different packaging strategies
- 4-pt bending proof test is applied to study the transmitting of strain for the packaging material.
- Multiple measurements to identify the mechanical/chemical/electrical degradation of the modules
- The degradation mechanisms will be quantified and compared across modules and exposures

References:

Acknowledgements:

Figure 57: Towards 50 Year Lifetime PV Modules: Double Glass vs. Glass/Backsheet, 6th Annual Data Science Symposium in CWRU, 2019.

In addition, three manuscripts are currently being prepared.

- Statistical Analysis and Degradation Pathway Modeling of PERC PV Minimodules with Different Packaging Strategies in Indoor Accelerated Exposures
- Four-Point Proof Testing of Glass/Backsheet PV Minimodules for Monitoring Exposure-Induced Changes in Packaging Materials
- Quantitative Learning from Spatiotemporal Image Datasets: Application to Degradation of Silicon Photovoltaic Modules

The first manuscript is based off on the indoor accelerated exposure results from sets #1-#5. The second manuscript will focus on mechanical 4-point proof loading results for all the minimodule sets. The third manuscript focuses on predicting changes in electrical features from spatiotemporal image datasets.

Students working on this project Over the years and during the extension period, faculty members, students, staff and collaborators have contributed greatly to the smooth functioning of Towards50 project. Some students who have been an active part of this project have successfully graduated from their degree programs. A brief update on the recent graduates and current members (students and postdoc) will be provided in this section.

- Xuanji Yu

  Xuanji is a postdoc working in the T50 project. He has a PhD in Materials Science and Engineering from Boston University and has worked as the Chief Reliability Engineer at Canadian Solar Inc. for two years before joining CWRU. His focus areas include $< S|M|R >$ Multiple Regression Prediction Model in netSEM (Principle 2) and joint inference of trained neural network model among heterogeneous Spatiotemporal (Stepwise) Image Datasets.

- Sameera Nalin Venkat

  Sameera is a PhD student working in the T50 project. She is pursuing her PhD in materials science and engineering at CWRU. Her focus areas in T50 include feature extraction, statistical analysis and data-driven modeling using netSEM. For her PhD work, she is involved in analyzing crystallization kinetics of fluoroelastomer films and is currently exploring spatiotemporal graph neural networks.

- Ange Dominique Yao

  Dominique is a BS/MS student majoring in Chemical Engineering. She has been working in the T50 project during the extension period. She has greatly contributed to the characterization of minimodules and extracted encapsulants and the ongoing manuscript preparation.

- Jiqi Liu

  Jiqi graduated with a PhD in Materials Science and Engineering from CWRU in May 2022. She has been an active member in the T50 project since its inception in 2019 and she has greatly contributed to both the experimental and data analysis aspects of the project. Her focus areas in the project were fabrication of minimodules, feature extraction and analysis along with development of federated inference. She has begun her new career role as a Packaging Reliability Engineer at Apple.

- William Oltjen

  William is a Macromolecular Science and Engineering MS student at the SDLE Research Center. He is involved in FAIRification of data, multiscale characterization of PV modules. In the T50 project, he has helped immensely in coordinating the measurements after each exposure step. He has also been the point of contact for exposing minimodules in exposure chambers.

- Raymond Wieser

  Raymond is a Materials Science and Engineering PhD student at the SDLE Research Center. His focus areas are studying backsheet degradation using spatiotemporal studies and constructing spatiotemporal graph neural networks for PV performance loss rate prediction.

In the T50 project, he has helped a lot in coordinating measurements and ensuring that the scheduled personnel are able to complete measurements as per the schedule in the initial stages of the project.

- Hein Htet Aung

  Hein is a Materials Science and Engineering PhD student. He has been actively developing the netSEM R package and helped extensively in discussing ideas with respect to the multiple regression analysis work in the project. For his PhD work, he is focusing on degradation of polymer systems (acrylics) and working on polymer additive manufacturing.

- Leean Jo

  Leean is an BS/MS majoring in Chemical Engineering. She has been helped extensively in doing the electrical measurements for PV minimodules after each exposure step. Her focus areas are development of the netSEM package and chemical characterization of polymer coupons.

- Jakob Wegmueller

  Jakob graduated with a BS in Mechanical Engineering from CWRU in May 2022. As an undergraduate, he started off with helping in the experimental side of the project, eventually transitioning to remote work during the pandemic and started exploring netSEM. His focus areas have been to help in the analysis of statistical results and data-driven modeling along with generalizing code for generating netSEM results. He will be beginning his graduate studies at the Department of Mechanical Engineering, Massachusetts Institute of Technology.

- Kemal Ozdemirli

  Kemal is an undergraduate pursuing BS in Mechanical Engineering at CWRU. His focus area is the development of an automated analysis pipeline for $< S|M|R >$ Multiple Regression Prediction Model in netSEM (Principle 2).

  We acknowledge the efforts and co-operation of the following SDLE Center graduate students and undergraduates in coordinating as well as doing measurements on 4-cell PV minimodules.

  Other undergraduates who have recently helped with measurements and exposures include:

- Jube Augustino
- Adam Goodman
- Gabriel Ponon
- Christelle Yameogo
- Summer Sun

Issues, Risks, and Mitigation:

We anticipate no critical problems or delays at this time.

Changes in Approach:

We have not instituted any changes to our approach at this stage of the project.

Key Personnel:

There have been no changes in Key Personnel or teaming.

Recipient and Principal Investigator Disclosures:

There are no Recipient or Principal Investigator Disclosures at this time. None of the sponsored persons or entities have been debarred, suspended, or found insolvent. Similarly, there have been no fraud convictions, violations of export control laws and regulations, or violations of the Drug-Free Workplace Act of 1988 to report.

Conflicts of Interests Within Project Team:

There are no Conflicts of Interest within the Project Team to report at this time.

Performance of Work in the United States:

There is no work funded under this award being performed outside the United States.

5 References

*

[1] Guide To Interpreting I-V Curve Measurements of PV Arrays, Application Note PVA-600-1, Solmetric (Mar. 2011).
URL `http://resources.solmetric.com/get/Guide%20to%20Interpreting%20I-V%20Curves.pdf`

[2] S. Nalin Venkat, Network Structural Equation Modeling of PV Minimodule Variants Under Indoor Accelerated Exposures, Master's thesis, Case Western Reserve University, tex.ids= nalinvenkatNetworkStructuralEquation (May 2021).

[3] IEC 60891:2021.
URL `https://webstore.iec.ch/publication/61766`

[4] W.-H. Huang, X. Ma, J. Liu, M. Wang, A. J. Curran, J. S. Fada, J.-N. Jaubert, J. Sun, J. L. Braid, J. Brynjarsdottir, R. H. French, ddiv: Data Driven I-V Feature Extraction (Sep. 2018).
URL `https://CRAN.R-project.org/package=ddiv`

[5] R. A. Sinton, A. Cuevas, A quasi-steady-state open-circuit voltage method for solar cell characterization, in: Proceedings of the 16th European Photovoltaic Solar Energy Conference, Vol. 1152, Glasgow, UK, 2000, p. 4.

[6] A. M. Karimi, J. S. Fada, M. A. Hossain, S. Yang, T. J. Peshek, J. L. Braid, R. H. French, Automated Pipeline for Photovoltaic Module Electroluminescence Image Processing and Degradation Feature Classification, IEEE Journal of Photovoltaics 9 (5) (2019) 1324–1335, conference Name: IEEE Journal of Photovoltaics. `doi:10.1109/JPHOTOV.2019.2920732`.

[7] A. M. Karimi, J. S. Fada, N. A. Parrilla, B. G. Pierce, M. Koyutürk, R. H. French, J. L. Braid, Generalized and Mechanistic PV Module Performance Prediction From Computer Vision and Machine Learning on Electroluminescence Images, IEEE Journal of Photovoltaics 10 (3) (2020) 878–887, conference Name: IEEE Journal of Photovoltaics. `doi:10.1109/JPHOTOV.2020.2973448`.

[8] G. Cumming, S. Finch, Inference by Eye: Confidence Intervals and How to Read Pictures of Data, American Psychologist 60 (2) (2005) 170–180. `doi:10.1037/0003-066X.60.2.170`.

[9] Sameera Venkat, Xuanji Yu, Jiqi Liu, Jakob Wegmueller, Jayvic Cristian Jimenez, Erika I. Barcelos, Hein Htet Aung, Xinjun Li, Jean-Nicolas Jaubert, Roger H. French, Laura S. Bruckman, Statistical Analysis and Degradation Pathway Modeling of Photovoltaic Minimodules with Varied Packaging Strategies, Frontiers in Energy Research 11 (2023). `doi:10.3389/fenrg.2023.1127796`.
URL `https://www.frontiersin.org/articles/10.3389/fenrg.2023.1127796`

[10] S. N. Venkat, J. Liu, J. Yu, Xuanji Wegmueller, K. Rath, X. Li, J.-N. Jaubert, J. L. Braid, L. S. Bruckman, R. H. French, Evaluation of PV Module Packaging Strategies of Monofacial and Bifacial PERC Using Degradation Pathway Network Modeling, in: 2022 IEEE 49th Photovoltaic Specialists Conference (PVSC), 2022, pp. 1020–1027. `doi:10.1109/PVSC48317.2022.9938854`.

[11] E. E. van Dyk, A. R. Gxasheka, E. L. Meyer, Monitoring current–voltage characteristics and energy output of silicon photovoltaic modules, Renewable Energy 30 (3) (2005) 399–411. `doi:10.1016/j.renene.2004.04.016`.
URL `https://www.sciencedirect.com/science/article/pii/S0960148104002447`

[12] E.E.van Dyk, E.L.Meyer, Analysis of the effect of parasitic resistances on the performance of photovoltaic modules, Renewable Energy 29 (3) (2004) 333–344. `doi:10.1016/S0960-1481(03)00250-7`.

[13] E.L. Meyer, E.E. van Dyk, Assessing the reliability and degradation of photovoltaic module performance parameters, IEEE Transactions on Reliability 53 (1) (2004) 83–92. `doi:10.1109/TR.2004.824831`.

[14] W.-H. Huang, Xuan Ma, Jiqi Liu, Menghong Wang, Alan J. Curran, J. S. Fada, Jean-Nicolas Jaubert, Jing Sun, Jennifer L. Braid, Jenny Brynjarsdottir, Roger H. French, Ddiv: Data Driven I-v Feature Extraction, Comprehensive R Archive Network (CRAN) (Apr. 2021).

[15] M. Wang, Tyler J. Burleyson, Jiqi Liu, Alan J. Curran, Abdulkerim Gok, Eric J. Schneller, Kristopher O. Davis, Jennifer L. Braid, Roger H. French, SunsVoc: Constructing Suns-Voc from Outdoor Time-Series I-V Curves, Comprehensive R Archive Network (CRAN) (Apr. 2021).

[16] N. Bosco, M. Springer, J. Liu, S. N. Venkat, R. H. French, Employing Weibull Analysis and Weakest Link Theory to Resolve Crystalline Silicon PV Cell Strength Between Bare Cells and Reduced- and Full-Sized Modules, IEEE Journal of Photovoltaics (2021) 1–11Tex.ids= boscoEmployingWeibullAnalysis2021a, boscoEmployingWeibullAnalysis2021b, nickboscoEmployingWeibullAnalysis2021 conferenceName: IEEE Journal of Photovoltaics. `doi:10.1109/JPHOTOV.2021.3056673`.

[17] M. Bora, S. Pop, R. Schulze, M. Rowell, D. Harwood, Moisture content imaging in glass-glass and glass-backsheet photovoltaic mini-modules, in: 2020 47th IEEE Photovoltaic Specialists Conference (PVSC), 2020, pp. 1485–1488, iSSN: 0160-8371. `doi:10.1109/PVSC45281.2020.9300346`.

[18] D. C. Miller, J. G. Bokria, D. M. Burns, S. Fowler, X. Gu, P. L. Hacke, C. C. Honeker, M. D. Kempe, M. Köhl, N. H. Phillips, K. P. Scott, A. Singh, S. Suga, S. Watanabe, A. F. Zielnik, Degradation in photovoltaic encapsulant transmittance: Results of the first PVQAT TG5 artificial weathering study, Progress in Photovoltaics 27 (5), institution: National Renewable Energy Lab. (NREL), Golden, CO (United States) Number: NREL/JA-5K00-72180 Publisher: Wiley (Jan. 2019). `doi:10.1002/pip.3103`.
URL `https://www.osti.gov/pages/biblio/1492516`

[19] Jennifer L. Braid, Ahmad Maroof Karimi, Benjamin G. Pierce, Justin S. Fada, Nicholas A. Parrilla, Roger H. French, Pvimage: Package for pv image analysis and machine learning modeling (May 2020).

[20] A. Sherstinsky, Fundamentals of Recurrent Neural Network (RNN) and Long Short-Term Memory (LSTM) Network, Physica D: Nonlinear Phenomena 404 (2020) 132306, comment: 43 pages, 10 figures, 78 references. `arXiv:1808.03314`, `doi:10.1016/j.physd.2019.132306`.

[21] K. Cho, B. van Merrienboer, D. Bahdanau, Y. Bengio, On the Properties of Neural Machine Translation: Encoder-Decoder Approaches, arXiv:1409.1259 [cs, stat]Comment: Eighth Workshop on Syntax, Semantics and Structure in Statistical Translation (SSST-8) (Oct. 2014). `arXiv:1409.1259`.

[22] M. Abadi, A. Agarwal, P. Barham, E. Brevdo, Z. Chen, C. Citro, G. S. Corrado, A. Davis, J. Dean, M. Devin, S. Ghemawat, I. Goodfellow, A. Harp, G. Irving, M. Isard, Y. Jia, R. Jozefowicz, L. Kaiser, M. Kudlur, J. Levenberg, D. Mané, R. Monga, S. Moore, D. Murray, C. Olah, M. Schuster, J. Shlens, B. Steiner, I. Sutskever, K. Talwar, P. Tucker, V. Vanhoucke, V. Vasudevan, F. Viégas, O. Vinyals, P. Warden, M. Wattenberg, M. Wicke, Y. Yu, X. Zheng, TensorFlow: Large-scale machine learning on heterogeneous systems, software available from tensorflow.org (2015).

[23] A. Khalilnejad, A. M. Karimi, S. Kamath, R. Haddadian, R. H. French, A. R. Abramson, Automated pipeline framework for processing of large-scale building energy time series data, PLOS ONE 15 (12) (2020) e0240461. `doi:10.1371/journal.pone.0240461`.
URL `https://dx.plos.org/10.1371/journal.pone.0240461`